Field observations and numerical simulations of storm-induced nearshore morphology change in Rincón, Puerto Rico

by

Patricia Chardón Maldonado

A thesis submitted in partial fulfillment of the requirements for the degree of

MASTER IN SCIENCE
in
CIVIL ENGINEERING
(Environmental and Water Resources Engineering)

UNIVERSITY OF PUERTO RICO
MAYAGÜEZ CAMPUS
2013

Approved by:

Miguel F. Canals Silander, Ph.D. President, Graduate Committee	Date
Ingrid Padilla Cestero, Ph.D. Member, Graduate Committee	Date
Luis Aponte Bermúdez, Ph.D. Member, Graduate Committee	Date
Ismael Pagán Trinidad, M. Sc. Chairperson of the Department	Date
Betsy Morales Caro, Ph.D. Graduate Studies Representative	Date

ABSTRACT

The municipality of Rincón, Puerto Rico has suffered from severe erosion during the last several decades. This stretch of coast is highly sensitive to storm-induced wave events. The effects of erosion on coastal communities and structures have been drastic and costly. It is therefore vital to understand the physical processes that induce nearshore morphology change in order to determine the causes of erosion as well as to suggest possible solutions to the problem. To assess short-term morphology changes, pre- and post-storm hydrographic surveys were carried out between July and November 2012 using a personal watercraft as a bathymetric surveying system. During this period, two storm events, Tropical Storm Isaac and Hurricane Sandy, impacted the coast of Rincón, allowing us to monitor and quantify erosion and accretion patterns in the nearshore region. The southwesterly wave events caused by Isaac and Sandy generated significant sediment transport and morphology change, causing the formation of shore-parallel sandbars. In contrast, the northwesterly swell generated by Sandy did not greatly affect nearshore morphology change.

To identify and understand the hydrodynamic processes responsible for the morphological changes observed in the field, a coupled wave-current-sediment transport numerical model, the Coastal Modeling System (CMS), developed by the U.S. Army Corps of Engineers, was implemented. Storm-induced circulation and sediment transport were reproduced for each storm and a detailed understanding of Rincón's coastal morphodynamic behavior was obtained. When compared with the jetski-based surveys, the model appears to predict, at least qualitatively, the large scale features of the observed morphology change for both storm events. Based upon the findings of this study, a much better understanding of the coastal dynamics of Rincón coast has been achieved.

RESUMEN

El municipio de Rincón, Puerto Rico ha sufrido de erosión severa durante las últimas décadas. Este tramo de costa es altamente sensible a las fuerzas oceanográficas inducidas por el oleaje de tormenta. Los efectos de la erosión sobre las comunidades y estructuras costeras han sido drásticos y costosos. Por lo tanto, para poder determinar la causa de estos procesos naturales como también poder sugerir posibles soluciones al problema, es de vital importancia entender los procesos físicos que inducen los cambios morfológicos cercanos a la costa. Para evaluar dichos cambios, mediciones hidrográficas antes y después de eventos ciclónicos se llevaron a cabo entre julio y noviembre del 2012 utilizando una motora acuática como sistema de mediciones batimétricas. Durante este período, dos tormentas, la tormenta tropical Isaac y el huracán Sandy, impactaron la costa de Rincón permitiéndonos monitorear y cuantificar los patrones de erosión y acreción en la región cercana a la costa. El oleaje proveniente del suroeste causado por Isaac y Sandy, generó un transporte de sedimento y un cambio morfológico significativo en la región cercana a la orilla causando la formación de bancos de arenas paralelos a la costa. Por el contrario, el oleaje proveniente del noroeste generado por Sandy no afectó en gran medida el cambio de morfología.

Para identificar y comprender los procesos hidrodinámicos responsables de los cambios morfológicos observados en las mediciones hidrográficas, se implementó el modelo acoplado de oleaje y circulación conocido como “Coastal Modeling System (CMS)”. Con este modelo se pudo reproducir la circulación de corrientes inducidas por tormentas y el transporte de sedimentos para cada tormenta permitiéndonos entender detalladamente el comportamiento morfodinámico de la costa. Cuando los resultados se comparan con las mediciones hidrográficas, el modelo parece predecir, al menos cualitativamente, la respuesta morfológica a gran escala observada tanto para el evento de Isaac como el huracán Sandy. Basado en las conclusiones de este estudio, se obtuvo un mejor conocimiento y entendimiento sobre las complejidades presentes en la costa de Rincón.

...to God, my family, friends, and mentors. For the support and help given along this fructiferous journey.

ACKNOWLEDGEMENTS

First of all, I would like to thank my parents, Wanda Maldonado and Roberto Chardón, for their unconditional support through all of my academic and personal endeavors. They have molded me into who I am today and taught me that with dedication, hard work, and perseverance any goal can be achieved. My most sincere thanks are given to them, to my grandmother, my sister Wandita and my boyfriend Francisco who supported me throughout this journey, regardless of the fact that my stress levels spilled over to them.

Special thanks to my advisor, Dr. Miguel F. Canals, who guided me through these years and introduced me to the world of coastal and ocean engineering. As a graduate student, I could not have asked for a better advisor than Dr. Canals. His level of care, dedication and interest is unsurpassed by anyone I have ever met in the academia. For that, I owe him many thanks.

I must also thank my committee, Dr. Ingrid Padilla and Dr. Luis Aponte for all the help provided. Additional gratitude to Dr. Jorge Capella whose attention and knowledge, helped make this thesis the best it could be.

This research could not have been successful without the help of the Ocean Engineering Laboratory technicians. David "Araña" Carrero who with his talent and knowledge helped develop the jetski-based surveying system and Carlos Ortiz who helped in the process of conducting field measurements. I am extremely grateful to have had the opportunity to work with such excellent persons. I must also thank my laboratory partner, André, for all his help. Thanks to my friends: Alejandro, Vincent, Arocho, Wesley, Fefa, Pacheco, Glenda, Angel, and many others for all their encouragement.

I gratefully acknowledge The Caribbean Coastal Ocean Observing System (CariCOOS) and the National Oceanic and Atmospheric Administration (NOAA) for their financial support for this research.

Contents

List of Figures

List of Tables

List of Symbols and Notations

A = empirical coefficient

ADCP = Acoustic Doppler Current Profiler

α_t = total-load adaptation coefficient

ASCII = American Standard Code for Information Interchange

β_{tk} = total-load correction factor transport

$\dot{C}$ = wave celerity

$\dot{C}_{g\theta}$ = wave velocities with respect to θ

$\dot{C}_g$ = group celerity

$\dot{C}_{gx}$ = wave velocities with respect to x

$\dot{C}_{gy}$ = wave velocities with respect to y

C_t = actual depth-averaged total-load sediment concentration

C_t^* = equilibrium depth-averaged total-load sediment concentration

C_{tk} = depth-averaged total-load sediment concentration for size class $\mathbf{k}$

C_{tk}^* = depth-averaged total-load equilibrium concentration

c_R = reference sediment concentration

D_{50} = median grain size

δ_{ij} = Kronecker delta

E = wave energy as a function of frequency and direction

E_r = surface roller energy

ε = coefficient of directional diffusion of wave energy

ε_{ij} = permutation parameter

ε_s = sediment mixing coefficient

f = wave frequency

f_b = bed-load scaling factor

f_c = Coriolis parameter

f_s = suspended-load scaling factor

g = gravitational constant

GPS = Global Positioning System

H_b = breaking wave height

h = total water depth

i = first point in the signal

j = computes an indexed sum

$\mathbf{k}$ = sediment size class

k_p = wave number

κ = von Karman constant

L_b = bed transport adaptation lengths

L_s = suspended transport adaptation lengths

LiDAR = Light Detection and Ranging remote sensing technology

λ = degree of longitude

M = number of observation-prediction pairs

MAV = moving average filter

MLW = Mean Low Water datum

MHW = Mean High Water datum

N = wave-action density

NMEA = National Marine Electronics Association

p_a = atmospheric pressure

q_b = actual bed load sediment transport

q_b^* = equilibrium bed load sediment transport rate

q_b^{*LC} = equilibrium bed load transport for Lund-CIRP formulation

q_b^{*vR} = equilibrium bed load transport for Van Rijn formulation

q_s = actual suspended load sediment transport

q_s^* = equilibrium suspended load sediment transport rate

q_s^{*LC} = equilibrium suspended load transport for Lund-CIRP formulation

q_s^{*vR} = equilibrium suspended load transport for Van Rijn formulation

q_{tot}^{*Wat} = total and bed load transport for Watanabe formulation

ρ_0 = reference water density

ρ_s = sediment density

ρ_w = density of water

R = number of points used in the moving average filter

R_{ij} = roller stress term

R^2 = correlation factor

RMSE = root mean square error

RTK = Real Time Kinematic satellite navigation

r_s = suspended sediment fraction

r_{sk} = fraction of suspended load in the total load for size class **k**

s = sediment specific gravity

σ = standard deviation

S = sources and sinks in wave action balance equation

S_{ij} = wave radiation stress

SBES = single beam echo-sounder

$\tau_{b,max}$ = maximum shear stress at the bed

τ_{bi} = combined wave-current mean bed shear stress

τ_{cr} = shear stress at incipient sediment motion

τ_{si} = surface wind stress

θ_H = surveying system heading

θ = wave direction

$\theta_{cw,m}$ = mean Shields parameter for waves and currents

θ_{cw} = maximum Shields parameter for waves and currents

T_p = spectral peak period

υ = mean wind speed profile

U = depth-averaged current velocity

U_{cr} = critical depth-averaged velocity necessary for initiation of motion

U_e = effective depth averaged velocity calculated

U_i = phase- and depth-averaged current velocity

u_w = wave bottom shear velocity

u* = friction velocity

U_{wi} = depth-averaged wave velocity

V_i = wave-averaged depth-integrated mass flux velocity

ν_s = horizontal sediment mixing coefficient

ν_t = turbulent eddy viscosity

w_s = sediment fall speed

w_{sk} = sediment fall velocity for size class k

WAAS = Wide Area Augmentation System

ω' = wave relative frequency

X' = adjusted coordinate (longitude)

X_{GPS} = original coordinate output from the GPS (longitude)

x = single beam echo-sounder raw signal

φ = degree of latitude

Y' = adjusted coordinate (latitude)

Y_{GPS} = original coordinate output from the GPS (latitude)

y = output signal

z = anemometer height above sea mean level

z_0 = surface roughness

Chapter 1

INTRODUCTION

1.1 Coastal processes

The shape of the world's coastlines is constantly changing in response to physical forcing caused by waves, tides, winds and the resulting current patterns. A detailed understanding of sediment transport and morphology change is vital for protecting both the coastal environment and the infrastructure that has been developed in this highly sensitive area. The most important sediment transport processes occur in the so-called littoral zone, which roughly extends from the shoreline to the edge of the continental shelf, as shown in Figure 1.1. The surf zone, defined as the region between the shoreline and the breaker line, is the most dynamic coastal region. The hydrodynamic processes which that occur in the surf zone are crucial for bathymetric evolution. As surface waves travel toward shore and interact with the seabed, their wave crests steepen as their amplitude increases, reaching a critical point where they break. This wave breaking process unleashes large amounts of kinetic energy which drives nearshore currents and produce sediment transport. Breaking waves are responsible for the transformation of wave motion into turbulence, entraining and suspending sediments off the seabed and into the water column, where wave-induced currents carry them away. For this reason, the surf zone has received a lot of attention from coastal engineers during the last several decades (Thieler et al., 2007).

There are several types of wave-induced currents. Alongshore currents flow parallel to the shoreline and decay rapidly seaward of the surf zone. Hydrodynamic instabilities can generate rip currents that flow seaward from the surf zone, which can transport momentum and sediment to the region outside of the surf zone. Rip currents can cause seabed scour and severe danger to

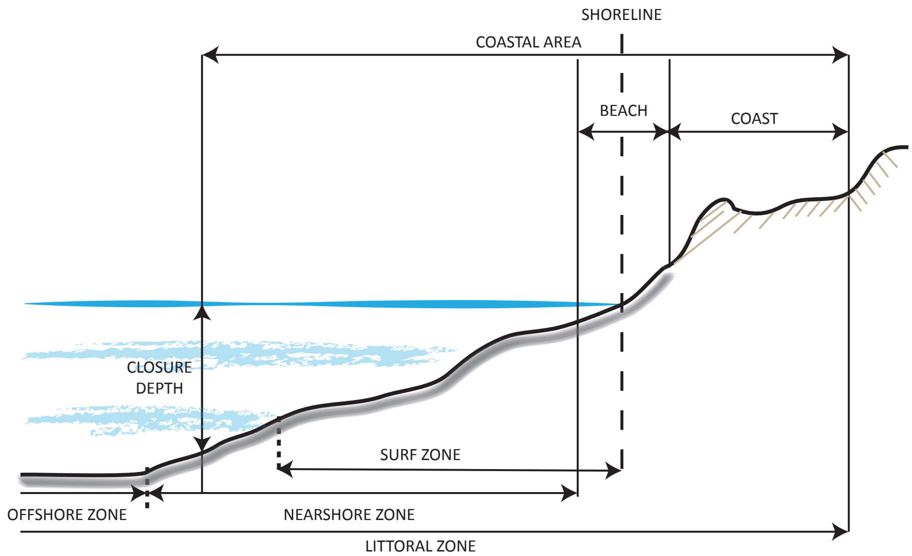

Figure 1.1: Schematic of the littoral region.

swimmers. These types of wave-induced nearshore currents interact with the currents driven by tides and wind to produce complex coastal circulation patterns. To understand coastal sediment transport, it is important to be able to understand and correctly model these complex circulation patterns and take into account the interaction between waves, tides and wind forcing.

Figure 1.2 shows a schematic diagram of the typical coastal erosion processes caused by storm-induced waves. These processes lead to the subsequent evolution of the beach profile. When storm waves affect the coast, they suspend sediments and affect the nearshore sediment balance. In general, a large portion of the eroded sand is transported seaward of the shoreline, frequently leading to the formation of shore-parallel sandbars (Fredsoe and Deigaard, 1992). After storm waves subside and normal wave conditions return, sand is slowly transported shoreward and, in the best of cases, the beach system slowly returns to equilibrium. In some cases, however, some sand may be lost permanently from the system, leading to possible permanent beach erosion. In the present study, jetski-based bathymetric surveys and numerical simulations of seabed erosion and sediment deposition were conducted to quantify morphology change in the municipality of Rincón, Puerto Rico, an area which has suffered from severe erosion in the past several decades (Thieler et al., 2007), as is explained below.

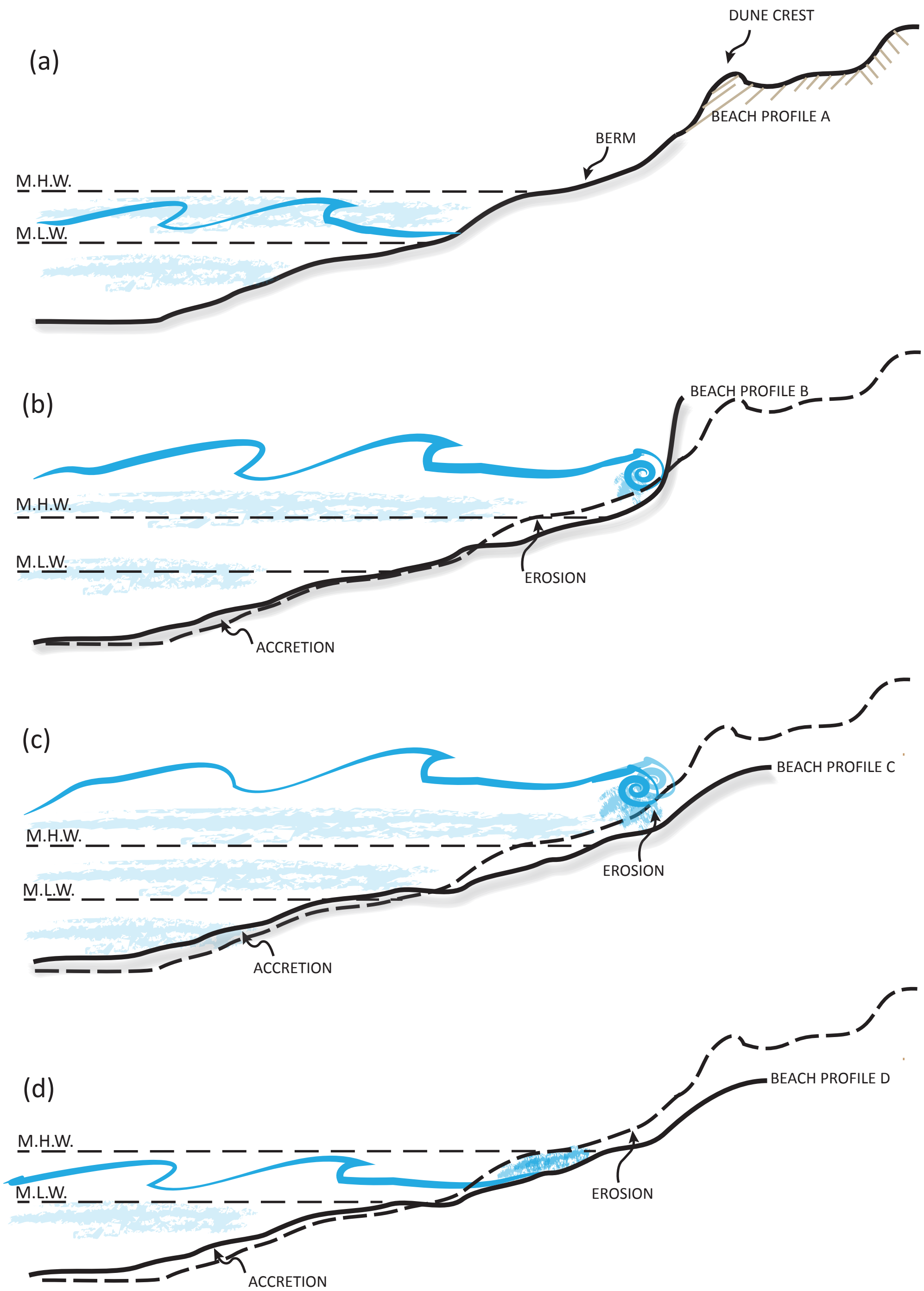

Figure 1.2: Schematic showing coastal response to storm waves in different stages: (a) normal wave action; (b) initial storm waves pounding the coast; (c) storm waves cause overtopping; (d) post-storm normal wave action. (M.H.W. represents the Mean High Water tidal datum and M.L.W. the Mean Low Water tidal datum).

1.2 Literature review

Puerto Rico is an island with approximately 700 miles of coastline (U.S. Department of Commerce, 1978). It has a highly energetic wave climate, which at some locations can lead to severe erosion. Its coasts are exposed to an active sequence of storms which are primarily responsible for shoreline erosion. Very few studies have been conducted to examine storm-induced nearshore changes in Puerto Rico. Knowledge about coastal processes and coastal erosion in Rincón is currently limited to studies carried out by Thieler et al. (2007) and Scott et al. (2012).

In 2007, the United States Geological Survey (Thieler et al., 2007) documented the long-term erosion rates in the municipality of Rincón, Puerto Rico. The study measured shoreline changes from 1936 to 2006 using aerial pictures, and revealed that the coast south of the Rincón marina is eroding at a rate of 0.5 to 1.0 m yr^{-1}, as a result of natural and human-induced causes. In 2012, Scott et al. (2012) analyzed beach profiles conducted during one year to characterize beach morphology changes caused by hurricanes and storms. Their measurements revealed that there is a seasonal cycle in sediment transport in Rincón, allowing the beach to recover most of the eroded sand within several weeks of storm-induced erosion events. However, storm-induced morphology changes in Rincón remain poorly understood, mainly because no study has measured sediment transport and morphology change in the surf zone, which is the region in which most of the morphology change occurs.

Short-term wave-induced morphology change has been widely investigated outside Puerto Rico, by analyzing seabed evolution during storm events using field surveys (van Rijn et al., 2003; Judge et al., 2003; Masselink et al., 2007; van Son et al., 2009; Trifonova et al., 2011) and numerical modeling (Zarillo and Brehinh, 2007; Nam et al., 2011; Ruggiero et al., 2009). These studies have presented evidence for a direct link between short-term morphology changes and storm wave events. Field surveys before and after storms have revealed that for micro-tidal regions such as Puerto Rico, sediment transport is mostly dominated by the seasonal cycle of storm wave events (Eversole and Fletcher, 2003). The migration of sediments as a morphological response to seasonal variability in wave energy can be readily observed by conducting pre- and post- storm transects. This method plays a pivotal role in numerical simulations, allowing the evaluation of the model's ability to reproduce the morphological changes observed in the field.

Despite the complexity of modeling sediment transport, several models have been developed which take into account the highly variable factors (wave, currents, seabed) that influence coastal processes (Cañizares and Irish, 2008). Among many models, 2D and 3D morphological models have been effective for simulating morphological evolution in coastal areas. The 2D models employ depth-averaged flow and wave equations (Sánchez et al., 2012), neglecting vertical variations, whereas 3D models include both vertical and horizontal variations (Deltares, 2011, 2012). Both type of models allow the coupling of wave, current, and sediment transport processes, however, 3D models are still somewhat limited since they are much more computationally expensive. Some numerical sediment transport modeling studies have shown good agreement between model predictions and field observations of nearshore storm-induced morphology change (Zarillo and Brehinh, 2007).

It is clear that waves and currents mobilize, suspend, and transport sediment whereas gradients in the sediment transport rate cause sediment deposition or removal (Nam and Larson, 2010), leading to seabed accretion and erosion, respectively. Intuitively, it is expected that the coast of Rincón will similarly respond to storm wave events, however, it is important to understand in detail the wave-induced circulation that causes morphology changes in the area. In this study, field observations and numerical modeling are implemented to, for the first time in Puerto Rico, understand and simulate short-term wave-induced nearshore morphology changes.

1.3 Study site

Rincón is located in the west region of Puerto Rico, and has approximately 12 kilometers of coastline, which consists mainly of sandy beaches and coral reef formations. The study site is located between Tres Palmas Marine Reserve and the Villa Cofresí Hotel, as shown in Figure 1.3. This site was selected for the present study due to the fact that it has been affected by severe long term and short term erosion (Thieler et al., 2007; Scott et al., 2012). In addition, a directional wave buoy (see Figure 1.3) is located in the vicinity of the study area, which provides accurate wave boundary conditions for the numerical simulations. This coastal area is influenced by wind-generated surface gravity waves which can be divided into wind-seas and long period swells. Wind-seas refers to waves with periods between 1 to 8 seconds whereas swells consist of waves with periods ranging from 8 to 25 seconds. A simple analysis of directional hindcast wave data from the Wave Information Studies (WIS) conducted by the U.S. Army Corps of Engineers (USACE, 2010), as well as CariCOOS (2008) regional buoys, shows that roughly 68% of the peak wave direction of the waves in Rincón come from the North-East, 28% from the North-West, 4% from the South-East and less than 0.5% from the South-West. Most of the time, however, there is a significant mix of wave directions and periods, which generate a complex sea state with both swell and wind-seas components. The sea state for this region varies seasonally, and is dominated by highly-energetic tropical storms in the fall and large winter swells from November to April. In between significant wave events, the easterly trade winds generate consistent wind-waves from the East and North-East.

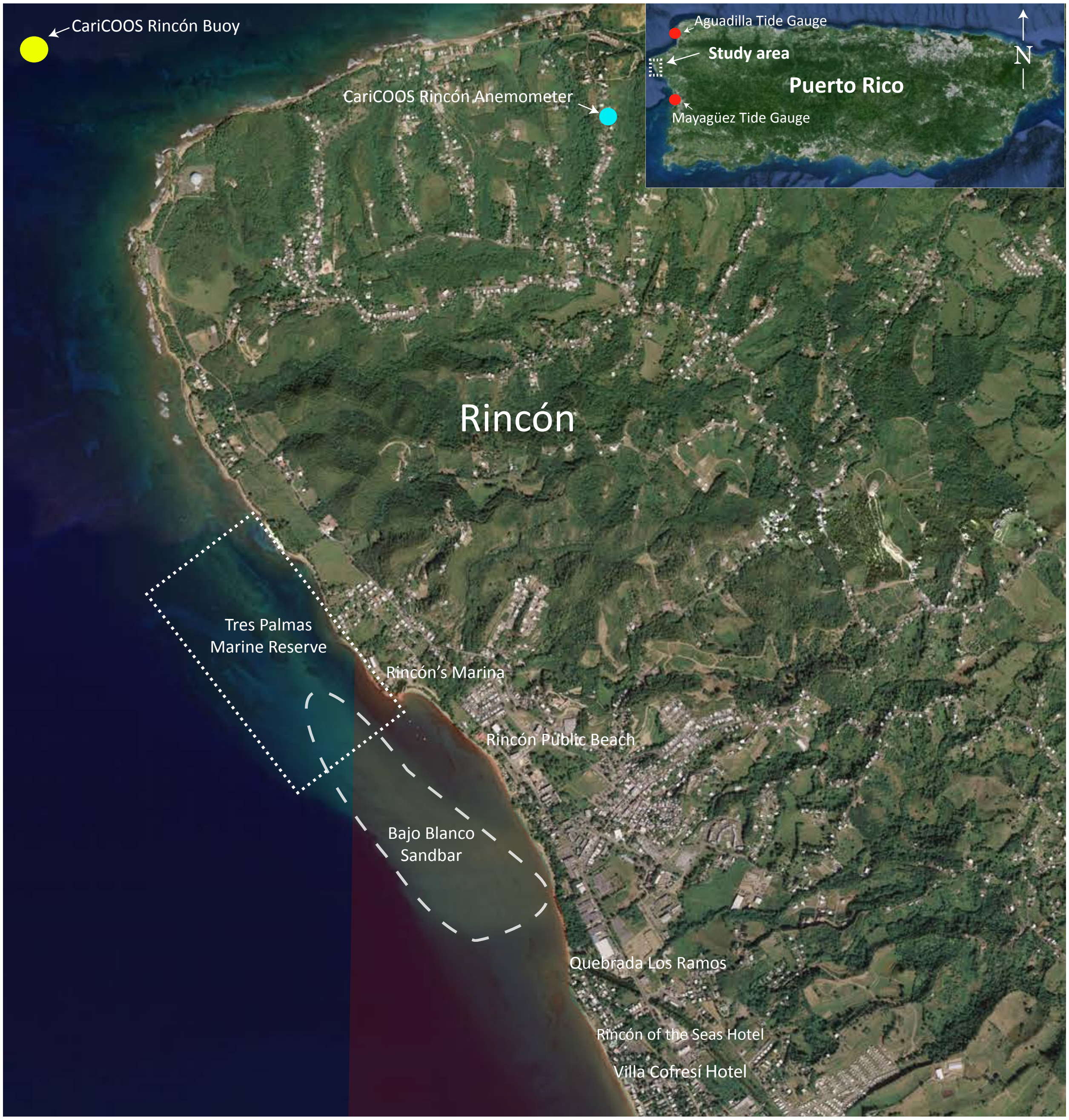

Figure 1.3: Aerial picture showing the location and important coastal features of the study site.

The local geomorphology of the study site is composed of sedimentary deposits, reefs and rock formations (Morelock, 1978). Figure 1.4 shows the different types of geological formations encountered in the study site. Around these isolated formations, large areas of sand and the Bajo

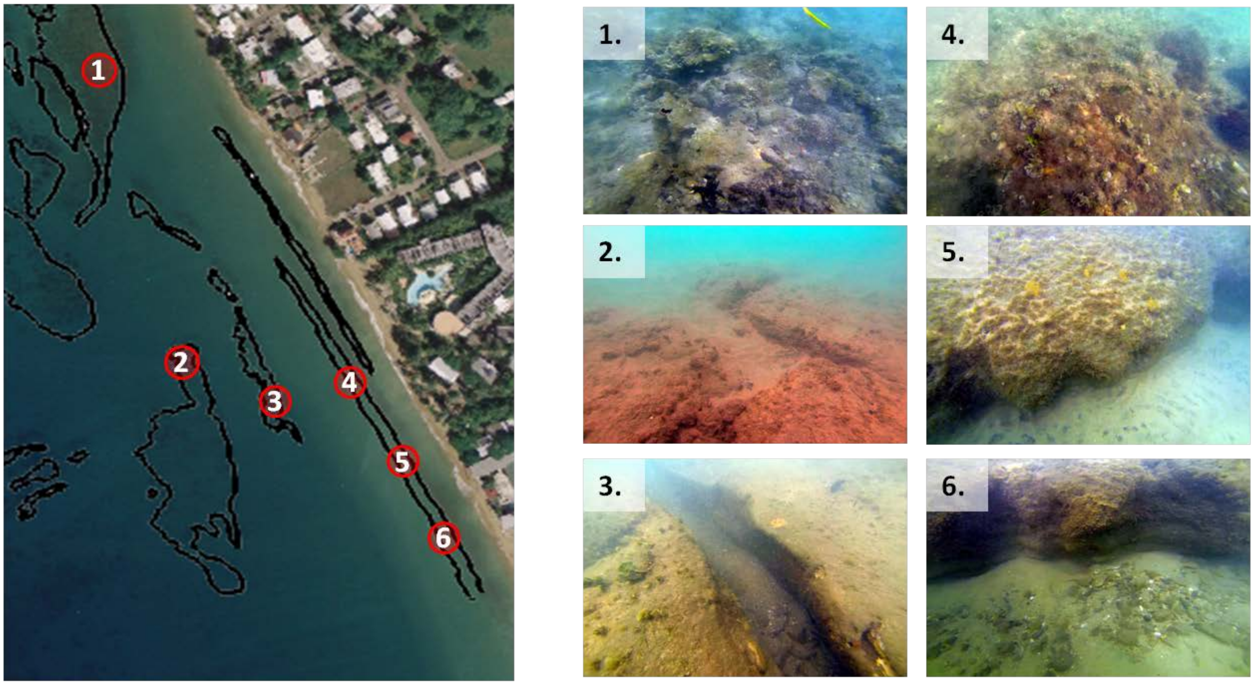

Figure 1.4: Geological formations (denoted by the black lines), composed of sedimentary deposits, reefs and rocks, located in the study area. The pictures on the right show seabed formations and were taken on the numbered locations shown on the picture in the left.

Blanco sandbar (Figure 1.3) are the dominant features. This study seeks to examine storm-induced nearshore morphology change in Rincón, taking into account the wave forcing and the complicated bathymetry of the study site, as outlined in the preceding paragraphs. The following chapter lays out the specific objectives of the present study.

Chapter 2

OBJECTIVES

The present study seeks to understand and quantify the morphological changes which occur in the nearshore region of the municipality of Rincón, Puerto Rico, by collecting detailed bathymetric data and conducting numerical model simulations. The specific objectives are as follows:

- Develop an inexpensive jetski-based bathymetric surveying system that can be deployed before and after extreme storm events, which are the major cause of severe morphological changes.
- Use the jetski-based bathymetric surveying system, collect bathymetric data before and after major storm events and quantify erosion and accretion patterns in the nearshore region.
- Implement and validate a coupled wave, current and sediment transport model, the USACE Coastal Modeling System (CMS), for the region in an effort to better understand the response of the nearshore morphology to extreme wave events.

It is expected that these hydrographic surveys and numerical simulations will allow a better understanding of the morphodynamic behavior of the region, and that this data will help oceanographers and coastal engineers design possible shoreline protection alternatives for Rincón, such as beach nourishment and offshore breakwaters. This information should also allow personnel from state and federal agencies to inform coastal residents and stakeholders about the sediment transport pathways and possible causes leading to the observed erosion.

2.1 Structure of the thesis

The goal of this thesis is to increase the understanding of sediment transport and coastal erosion in Rincón. This thesis is divided into two major components: field observations and numerical simulations. Chapter 3 includes a technical description of the development of the bathymetric surveying system and a detailed analysis of pre and post-storm bathymetric surveys. Chapter 4 deals with the implementation of the coupled wave, current and sediment transport model, model validation, and a qualitative comparison between the observed and modeled morphology change. The material contained in Chapters 3 and 4 have been submitted as separate articles to peer-reviewed scientific journals. Concluding remarks and final recommendations are given in Chapter 5.

Chapter 3

MONITORING MORPHODYNAMIC CHANGES IN RINCÓN, PUERTO RICO USING A JETSKI-BASED BATHYMETRIC SURVEYING SYSTEM

The material presented in this chapter is an expanded version of the article *"Monitoring Morphodynamic Changes in Rincón, Puerto Rico using a jetski-based bathymetric surveying system"* by Patricia Chardón and Miguel Canals, which has been submitted to a peer-reviewed scientific journal.

3.1 Introduction

The municipality of Rincón, located in Puerto Rico's west coast (Figure 1.3), has suffered from severe erosion affecting its beaches (Thieler et al., 2007), which are a major tourist attraction. This erosion is believed to be caused by intense tropical storms and hurricanes as well as North Atlantic winter storms. A detailed understanding of coastal processes such as wave forcing and morphology change in the region is vital to determine the causes of these erosion events, as well as recommending potential solutions to the problem, such as shoreline protection and beach nourishment. To monitor these erosion events, a flexible system, that can be rapidly deployed to collect data across the surf zone before and after storm events, was developed by using a personal watercraft as a bathymetric surveying system. This chapter reports on the design and calibration of the system as well as the analysis of pre- and port-storm hydrographic surveys.

3.2 Jetski-based bathymetric surveying system

The jetski-based bathymetric surveying system, named as Tarzan, was developed to navigate in the surf zone and in very shallow water. Figure 3.1 shows the developed system with the main instruments used for data acquisition (Chardón, 20). The surveying platform is based on previously developed systems, such as the Beach et al. (1994) coastal profiling system (CPS), the Morris et al. (2000) surf and coastal area measurement platform (SCAMP), the MacMahan (2001) modified version of the CPS model, and on the surveying platform developed by van Son et al. (2009). Of these systems, the SCAMP was the most accurate system, with vertical errors less that 0.05 m due to the implementation of a highly sensitive real time kinematic (RTK) GPS system.

The platform used in the present study is a 2011 four-stroke Yamaha VXR WaveRunner, chosen due to its stability, ease of deployment and fuel efficiency. An Airmar P66 single beam echo-sounder (SBES), mounted in the bottom of the watercraft hull at a distance of 0.35 meters below the waterline, has the capacity to measure depth up to 450 meters with a 200 kHz operating frequency and a 15 degree beam width. A towed Starfish side scan sonar unit with a 1 MHz operating frequency and 60 degree vertical beam width allows the acquisition of high quality imagery in the form of false-color images of the sea floor, with a maximum lateral range of 30 meters at either side of the jetski (StarFish, 2010). The echo-sounder is connected to a Garmin GPS 546s receiver which has less than 3 meters of error in horizontal position (Garmin, 2012).

The power supply for the instrumentation consists of an Epcom 50 Watt solar panel mounted in the front of the jetski, which provides power to a waterproof 12 volt battery. To consolidate all data streams, an onboard laptop is connected to a detailed NMEA 0183 (National Marine Electronics Association) network (Actisense, 2011). The laptop is mounted using a watertight case modified to provide visual access to the operator. The network uses NMEA 0183 ASCII character sentences to control all data acquisition, which allows real-time synchronization of all data streams.

Figure 3.1: Personal watercraft instrumentation: (1) watertight laptop case; (2) Garmin GPS receiver; (3) side scan sonar tow stand; (4) single beam echo-sounder (SBES); (5) Starfish side scan sonar; (6) solar panel.

3.3 Field deployments

Hydrographic surveys were conducted from July to November 2012, which is before and after the active storm season. A total of nine cross-shore surveys were conducted within the study period. For each hydrographic survey, environmental conditions were carefully observed to ensure data quality and the safety of the operator. To perform good hydrographic surveys, the following measures were taken into consideration before deployment:

- Offshore wave heights below 1.0 meter (as observed by the CariCOOS buoy, Figure 1.3), to ensure low surf zone conditions and to minimize the air bubbles generated by breaking waves
- Wave periods longer than 5 seconds, allowing a smooth and calm ocean for better maneuverability of the system
- Surveys were conducted in the early morning hours to work with suitable wind conditions below 8 knots. When the wind increased significantly, surveys were quickly aborted and resumed the next morning.

The wave data was provided by the CariCOOS Datawell Directional Waverider Buoy, which is located 1 mile off the Rincón Lighthouse (Figure 1.3) in a water depth of 33 meters (Figure 3.2a). In addition to the wave data provided by this buoy, nearby meteorological stations and two NOAA tide gauges provided real-time environmental conditions. The inset in Figure 1.3 shows the location of the two tide gauges depicted by red circles. The CariCOOS Nearshore Wave Model, Figure 3.2b, provided the wave forecasts used to plan the surveys.

Table 3.1 shows the details and environmental conditions during each survey. The first four surveys were conducted to obtain the baseline bathymetry, shown in Figure 3.3a. The other five surveys allowed to quantify morphology change before and after two storm events that affected

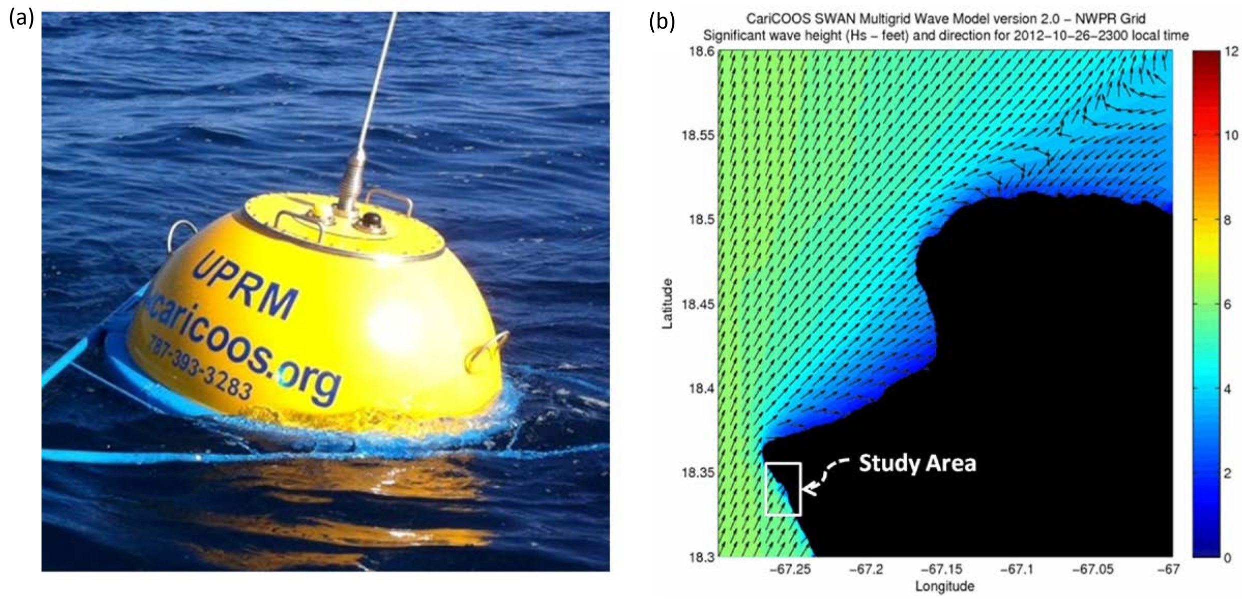

Figure 3.2: (a) CariCOOS Rincón Datawell Waverider buoy, (b) CariCOOS SWAN Multigrid Wave Model, Northwest Puerto Rico Grid (vectors represent wave direction).

Table 3.1: Details and environmental conditions during the bathymetric surveys; surveys 1 through 4 correspond to the baseline surveys.

Survey	1	2	3	4	5[a]	6[b]	7[c]	8[d]	9[e]
Date (2012)	7/24	7/26	8/7	8/10	8/21	8/27	9/20	10/24	11/9
Wave height (m) at Rincón buoy	0.5	0.3	0.2	0.4	0.6	0.5	0.6	1.0	0.5
Mean wave period (s)	7	7	5	8	5	7	6	8	12
Wind speed (kts)	3-6	2-4	3-7	2-4	2-4	1-4	1-2	2-4	1-3
Wind direction	SE	SE	NE	SE	SE	SE	SE	SE	SE
Water temperature(°C)	28.5	28.1	27.9	28	28.1	27.3	29	27.3	28
Average transect distance (m)	750	750	750	750	600	750	500	450	550
Surveying time (h:mm)	5:30	6:20	5:45	4:15	7:00	3:30	4:30	3:00	3:15

[a]Survey conducted three days before Tropical Storm Isaac.
[b]Survey conducted three days after Tropical Storm Isaac.
[c]Survey conducted 15 days after Tropical Storm Isaac to monitor seabed recovery from erosion.
[d]Survey conducted two days before Hurricane Sandy.
[e]Survey conducted 24 days after Hurricane Sandy.

Rincón during the study period. To analyze pre- and post-storm bathymetric surveys, multiple transects were selected as shown in Figure 3.3b.

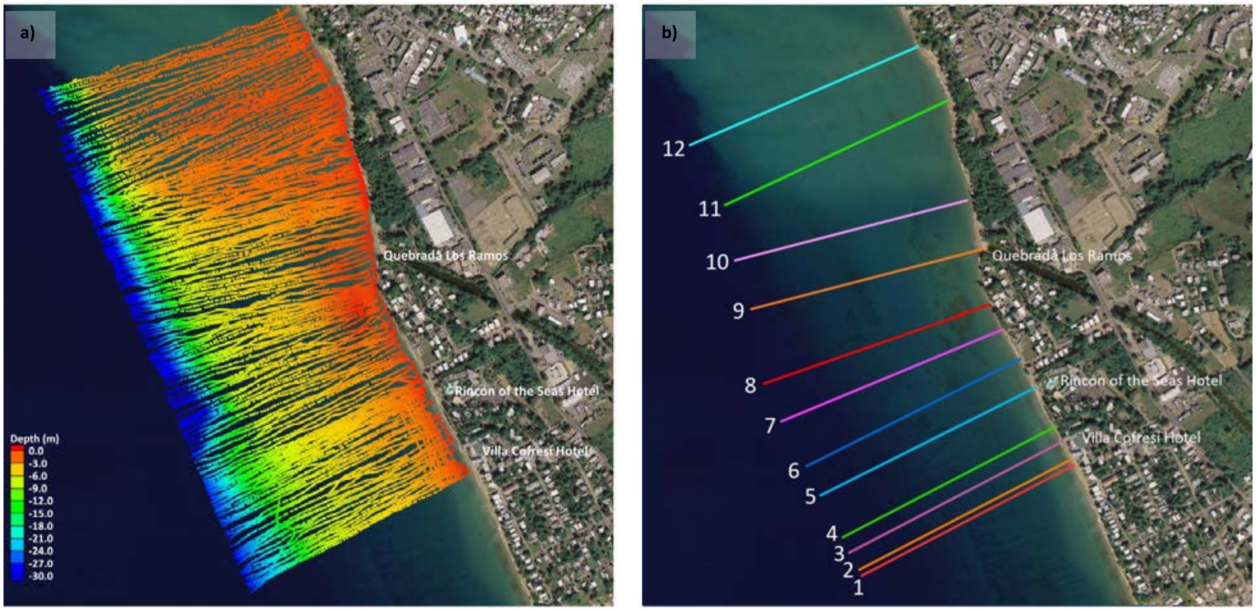

Figure 3.3: (a) Baseline bathymetry and (b) cross-shore transects selected to analyze morphological changes.

3.4 Data processing

The methodology used to acquire, process and analyze the bathymetric data necessary to quantify morphology change is shown in Figure 3.4. While the days selected for the surveys were chosen based on optimal environmental conditions, there are still significant errors that were induced by waves, wind, instrument position and others.

The use of an NMEA 0183 network allowed time frame synchronization between the GPS receiver and SBES transducer. Employing MATLAB, NMEA 0183 sentences were read and processed to minimize the errors due to low satellite connectivity, vertical position errors caused by tidal changes, jetski pitch, roll and heave, and other variables. The following actions were performed to minimize the errors and translate the raw data into meaningful bathymetric data:

1. Correct horizontal offset between GPS receiver and SBES
2. Filter noise spikes due to vessel heave using a moving average filter
3. Adjust the depth data due to tidal fluctuations and reference them to Mean High Water (MHW) tidal datum

These actions are described in detail below.

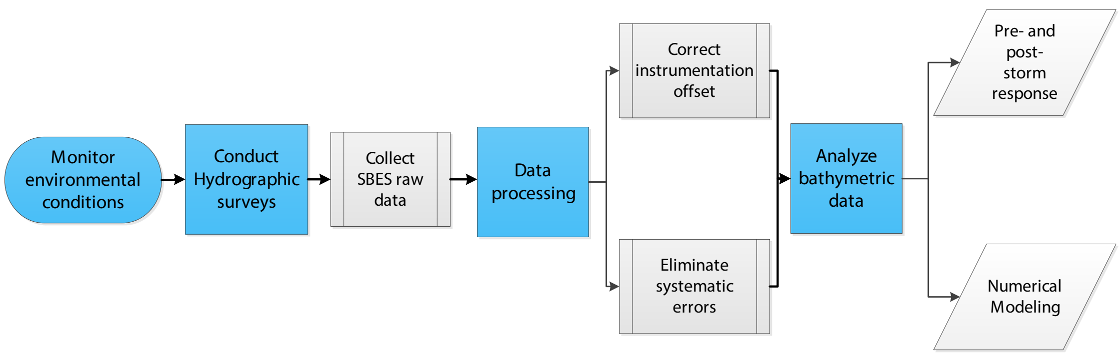

Figure 3.4: Methodology used to collect, process, and analyze bathymetric data.

3.4.1 Offset correction between GPS receiver and SBES

The GPS receiver, mounted near the jetski handlebar, is offset horizontally by a distance of 1.78 meters along the vessel centerline and offset 0.40 meters in the direction perpendicular to the jetski centerline, as shown in Figure 3.5. To correct for this offset, the surveying system heading, θ_H, was used to project the GPS coordinates towards the transducer location as follows:

$$X' = X_{GPS} + \sin(\theta_H) * \left(\frac{1.78m}{\lambda}\right) + \cos(\theta_H) * \left(\frac{0.40m}{\varphi}\right) \tag{3.1}$$

$$Y' = Y_{GPS} - \cos(\theta_H) * \left(\frac{1.78m}{\lambda}\right) - \sin(\theta_H) * \left(\frac{0.40m}{\varphi}\right) \tag{3.2}$$

where X' and Y' are the adjusted coordinates; X_{GPS} and Y_{GPS} are the original coordinates output from the GPS, λ= 111,321 meters per degree of longitude; and φ= 111,132 meters per degree of latitude.

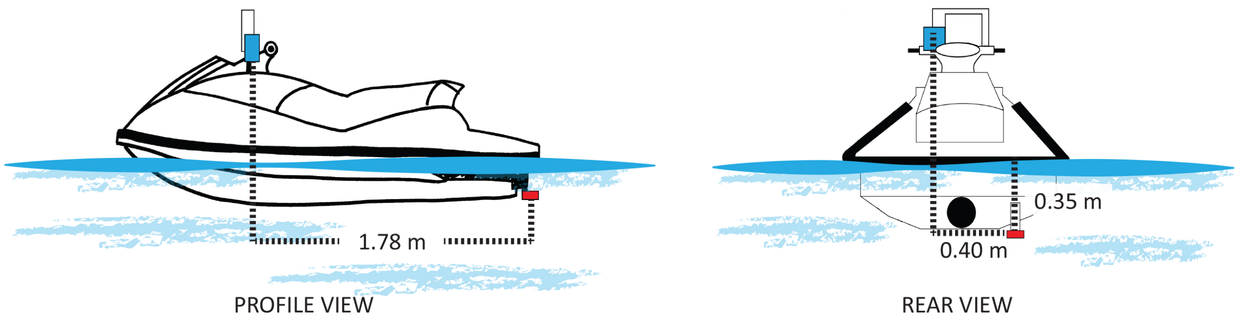

Figure 3.5: Offset between GPS receiver and single beam echo-sounder transducer (SBES).

3.4.2 Error correction due to vessel heave motion

The single beam echo-sounder (SBES) emits and receives a series of energy pulses in the form of sound waves. These waves can contain signal and/or noise; the latter is an unwanted error when collecting depth data. This error can be attributed to different sources such as:

· The jetski propulsion system, which induces turbulent water motion near the transducer

· Jetski motion due to wave conditions or operator error

· Signal distortion due to the presence of bubbles generated by breaking waves and turbulence

The spikes generated by these high frequency fluctuations are not bathymetric features, and the raw signal must to be filtered. A moving average filter (MAV) was applied to reduce random noise and smooth the SBES signal. The MAV mathematical form is:

$$y[i] = \frac{1}{R}\sum_{j=0}^{R-1} x[i+j] \tag{3.3}$$

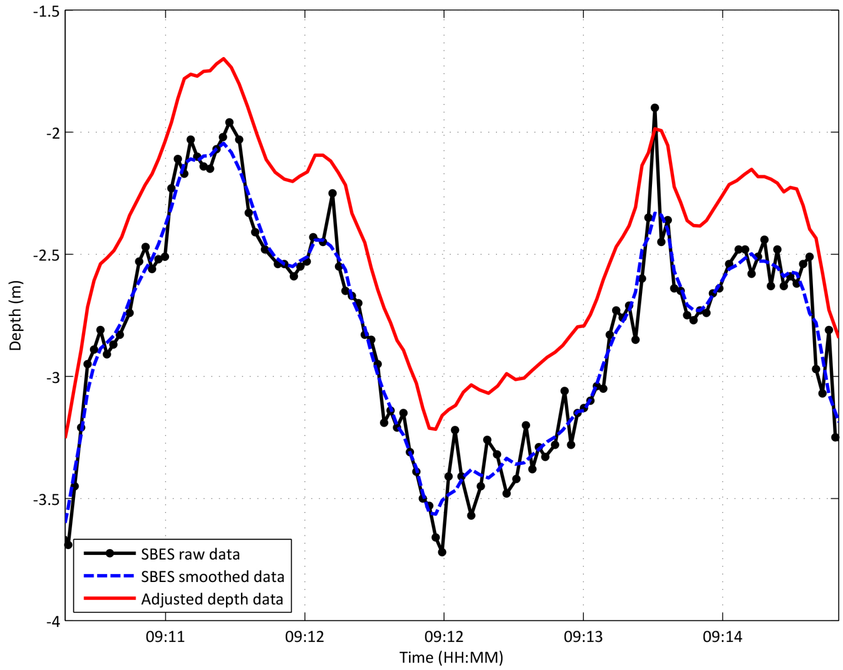

Figure 3.6: Data filtering and datum adjustment: the black line represents the single beam echo-sounder raw data and the blue line represents the filtered bathymetric data using a Moving Average Filter (MAV). The red line shows the filtered data which was referenced to the Mean High Water vertical tidal datum.

where y is the output signal, x is the SBES raw signal; i is the first point in the signal; j computes an indexed sum; and R is the number of points used in the MAV. A 3-point filter (R=3) was used to avoid filtering out actual morphological features. Figure 3.6 shows the signal (blue line) obtained after the SBES raw signal (black line) was filtered.

3.4.3 Vertical adjustments and vertical datum referencing

As shown in Figure 3.5, there is a vertical offset of 0.35 meters between the transducer and the water line. This distance was added to the raw sounder data, and then all depths were referenced to a common vertical tidal datum. Due to the lack of a tide gauge in Rincón, two nearby stations located in the municipalities of Aguadilla and Mayagüez were used (see Figure 1.3 for local reference). To estimate tidal values for the study site, a time shift was computed using the mean value between the high and low tide for each survey day in each station. Applying a linear interpolation, the estimated time-dependent water surface elevations were obtained and the tidal fluctuations were removed from the SBES bathymetry data. The transformations from one vertical datum into another were accomplished using the V-Datum transformation tool (NOAA, 2013). Developed by NOAA, this tool allows the conversion of data from diverse sources into a common tidal datum, and in the case of this study to the MHW tidal vertical datum. The red line in Figure 3.6 shows the adjusted and transformed depth data.

3.5 System calibration and error estimation

To ensure that the acquired data was correct, the bathymetric data was evaluated in two ways. First, four transects were selected and surveyed multiple times to compare the depth values. The collected data was then compared with existing LIDAR bathymetric data. On October 24, 2012, transects 1, 4, 5 and 6, shown in Figure 3.7, were surveyed multiple times. The length of each transect was approximately 400 meters long. At slow speeds, the effects of wind and waves upon the vessel prevents the jetski operator to navigate in a perfect straight line, making it difficult to cover exactly the same transect in each measurement. However, these measurements are useful in determining the errors considered when comparing different depth profiles to quantify morphology change caused by a storm.

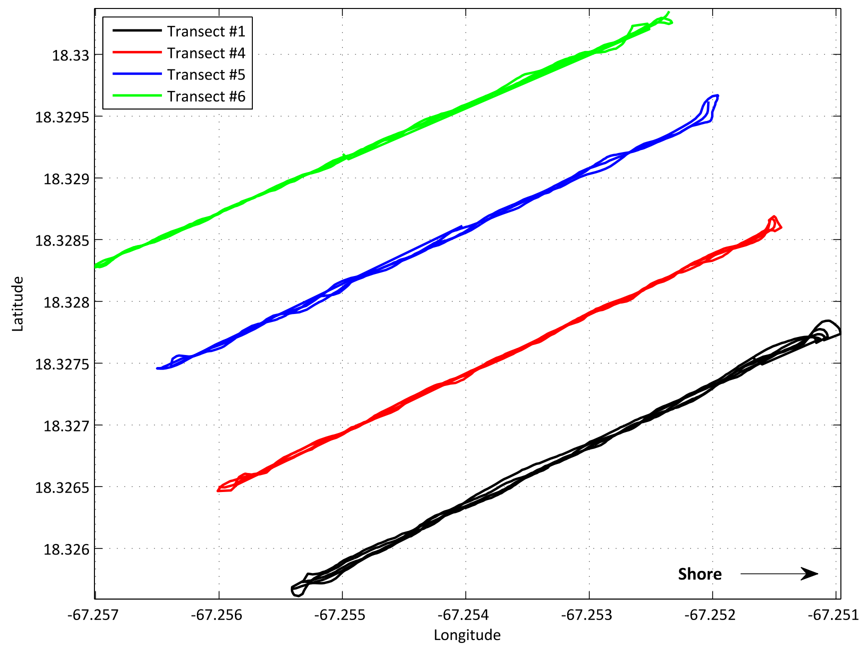

Figure 3.7: Location of the cross-shore transects used for error estimation (see Figure 3.3b for local reference).

To estimate the uncertainty in the observations, the horizontal distance from each data point to the theoretical centerline for each transect was determined. All points with a distance larger than 3 meters from the centerline were discarded, based on the 3 meter accuracy of the WAAS-corrected GPS receiver (Garmin, 2012). The resulting data points then resided in a 6-meter wide band around the centerline of each transect. Each transect was then discretized into two meter segments, and at each of these points, the standard deviation of all depth data points within a radius of two meters was calculated. The 2 meter radius was determined by calculating the maximum radius of coverage of the single beam echo-sounder, given the 15° beam width. Figure 3.8 shows the standard deviation at a spacing of 2 meters for each transect. The higher standard deviation values were associated, in general, with areas with larger seabed slopes, as would be expected. The errors contained in these standard deviation estimates can be attributed to the following reasons:

- Difficulties encountered by the vessel operator to sail exactly the same transect
- Changes in slope of the seabed may cause significant errors in echo-sounder bathymetry

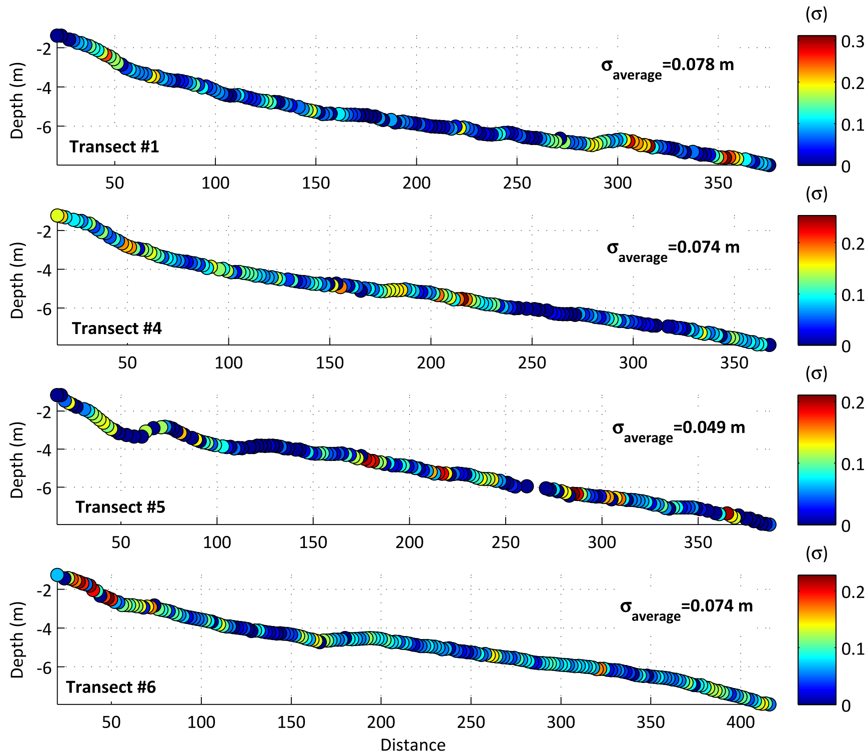

Figure 3.8: Standard deviation as a function of horizontal distance from shore. The color scheme depicts the standard deviation. The higher standard deviation values were associated, in general, with areas with larger seabed slopes. The average standard deviation for each transect is indicated in each figure. These values were then averaged and used to determine the 95% confidence intervals for the bathymetry profiles.

- Effects of waves on jetski motion, which may have been unaccounted for in the filtering procedure previously described

These values of standard deviation allowed the estimation of the 95% of confidence levels, given by $\pm 2\sigma$, in order to provide an uncertainty estimate of the cross-shore depth profiles to be discussed later on.

The collected baseline bathymetric data was then compared with existing USGS LIDAR bathymetry. The USGS bathymetric data was obtained in 2007 using LIDAR (Taylor et al., 2008) at a 10 meter horizontal resolution. Multiple transects were selected to compare these two datasets. Figure 3.9 shows the selected transects comparing depth profiles between the USGS data and the data collected with the surveying system. Close to shore there were significant differences between

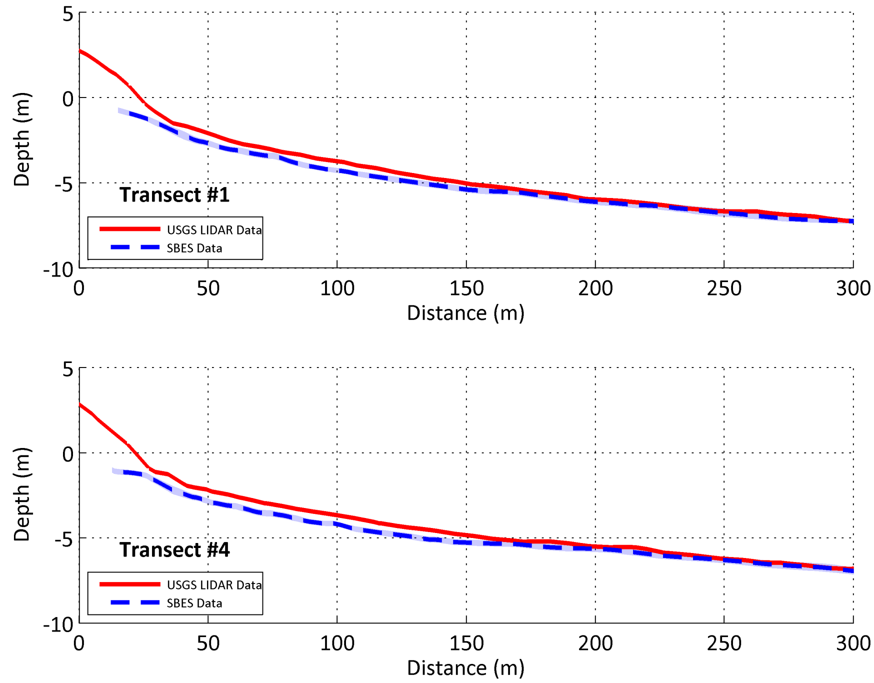

Figure 3.9: Comparison between USGS LIDAR (red line) and jetski surveying system data (blue line) profiles obtained from transects 1 and 4. Significant differences between the USGS and the SBES data were observed in the nearshore region, but in deeper water bothagreed very well. The shaded area depicts the 95 % confidence level of the observations, given by $\pm 2\sigma$.

the USGS and the SBES data, but in deeper water both agreed very well. This suggests that the collected data represents well the bathymetric profile. Differences in the nearshore region were likely associated with the seasonality of the erosion and accretion processes in Rincón or with errors in the LIDAR data interpolation close to shore. These errors in LIDAR are well known to occur very close to shore due to the presence of bubbles and suspended sediment (Science Delivery Division, 2013). Furthermore, the collected bathymetry provided better resolution, due to the ability of the system to reach very shallow water depths, which allowed the characterization of seabed formations close to shore.

3.6 Field observations of storm-induced nearshore morphology change

Hydrographic surveys were conducted from July to early November 2012. Two storms impacted the area during that period: Tropical Storm Isaac passed south of Puerto Rico in August 2012, and Hurricane Sandy generated a very large wave event in October 2012. Both of these events caused severe coastal erosion, with significant damage to coastal infrastructure, as shown in Figure 3.10. Given that beach erosion was widely documented by residents, the field surveys were designed to understand erosion in the nearshore subaqueous region, where morphology changes had never been quantified.

3.6.1 Measurements of the morphological response after Tropical Storm Isaac

On August 23-24, 2012, Tropical Storm Isaac had maximum sustained winds of 40 knots and was moving westward at a speed of 16 knots (National Weather Service, 2012). Figure 3.11 shows the path of the storm moving away from the island. Storm waves generated by Isaac were felt in Rincón on August 24-25, 2012 after the storm was located south of Puerto Rico and was moving westward in the Caribbean Sea. The maximum significant wave height observed was of 1.8 meters with a peak period of 9 seconds. These short period storm waves are typical of the waves generated by tropical storms in the Caribbean Sea. Figure 3.12 shows the wave height, period, and direction observed at the Rincón CariCOOS wave buoy from August 19 through September 24, 2012. While these were not very large waves, the peak wave direction was 230 degrees, and this southwesterly direction is extremely rare for this stretch of coast. Because of this wave direction, strong waves pounded an otherwise calm section of the coast, causing severe damage to the coasts of Rincón, destroying structures and causing a significant loss of beach sand. Figure 3.13 shows the output from the CariCOOS Nearshore Wave Model during the peak of the wave event.

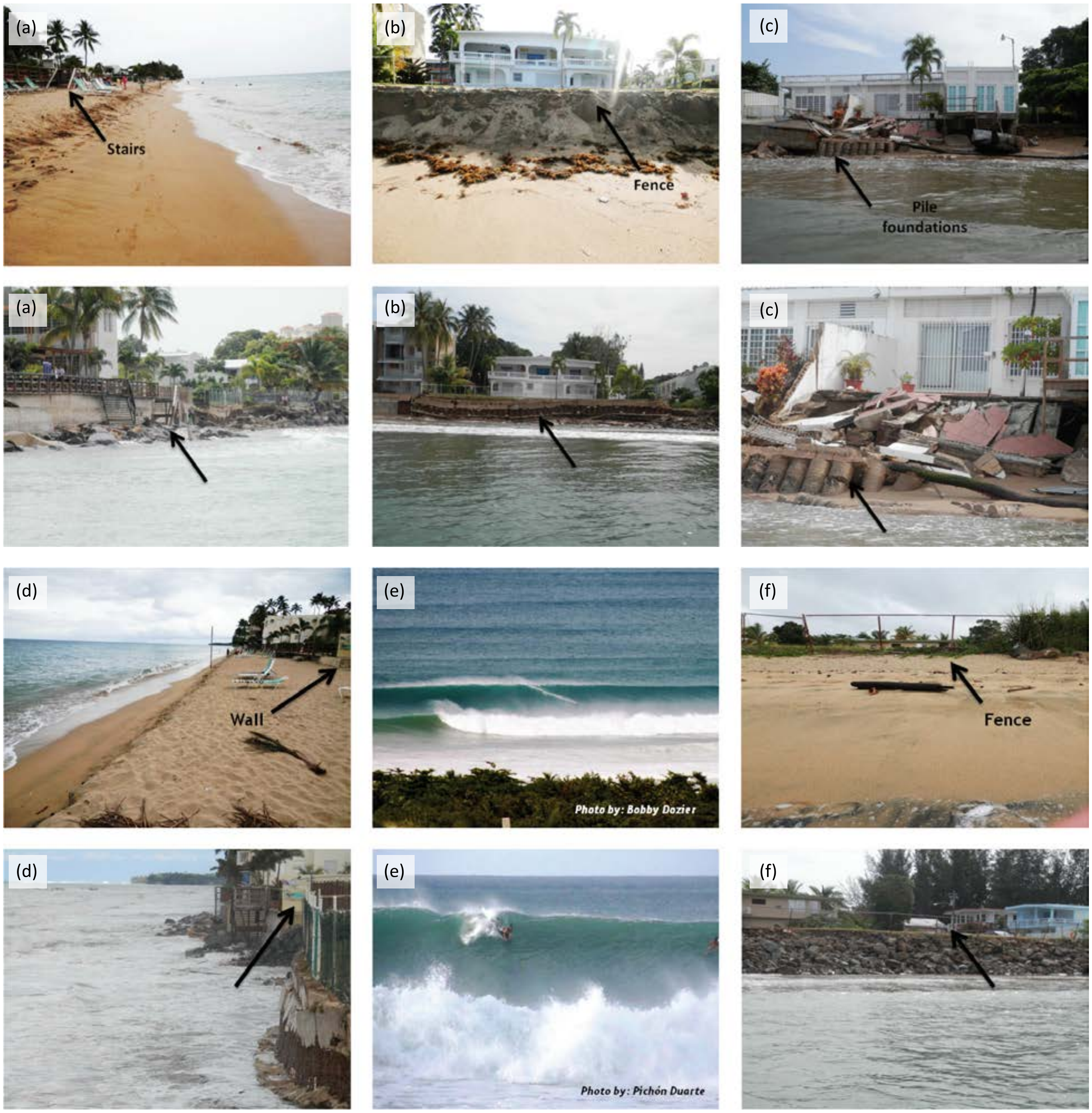

Figure 3.10: Photographs illustrating the effects of Tropical Storm Isaac (top two rows) and Hurricane Sandy (bottom two rows) in Rincón's beaches. The photos identified by the same letter represent the same location.

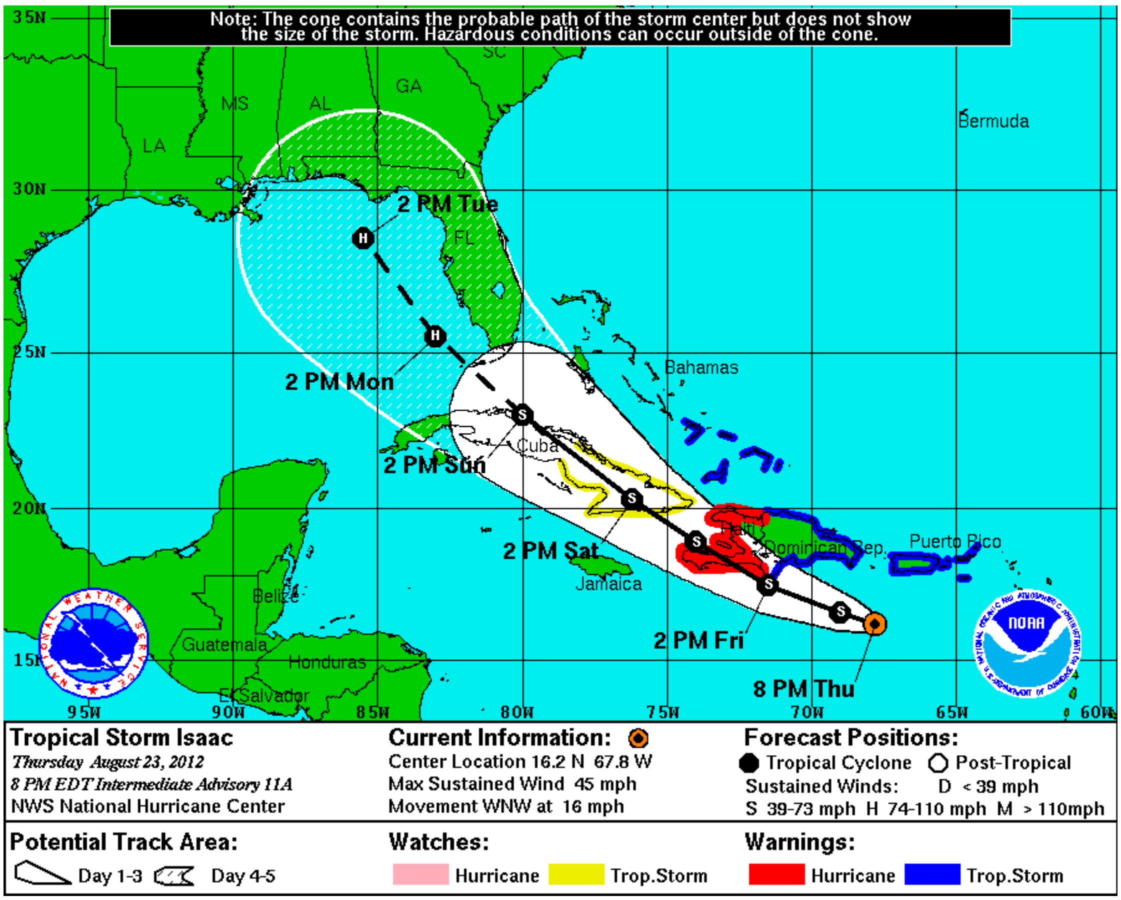

Figure 3.11: Path of Tropical Storm Isaac moving westward in the Caribbean Sea (from the National Weather Service, 2012).

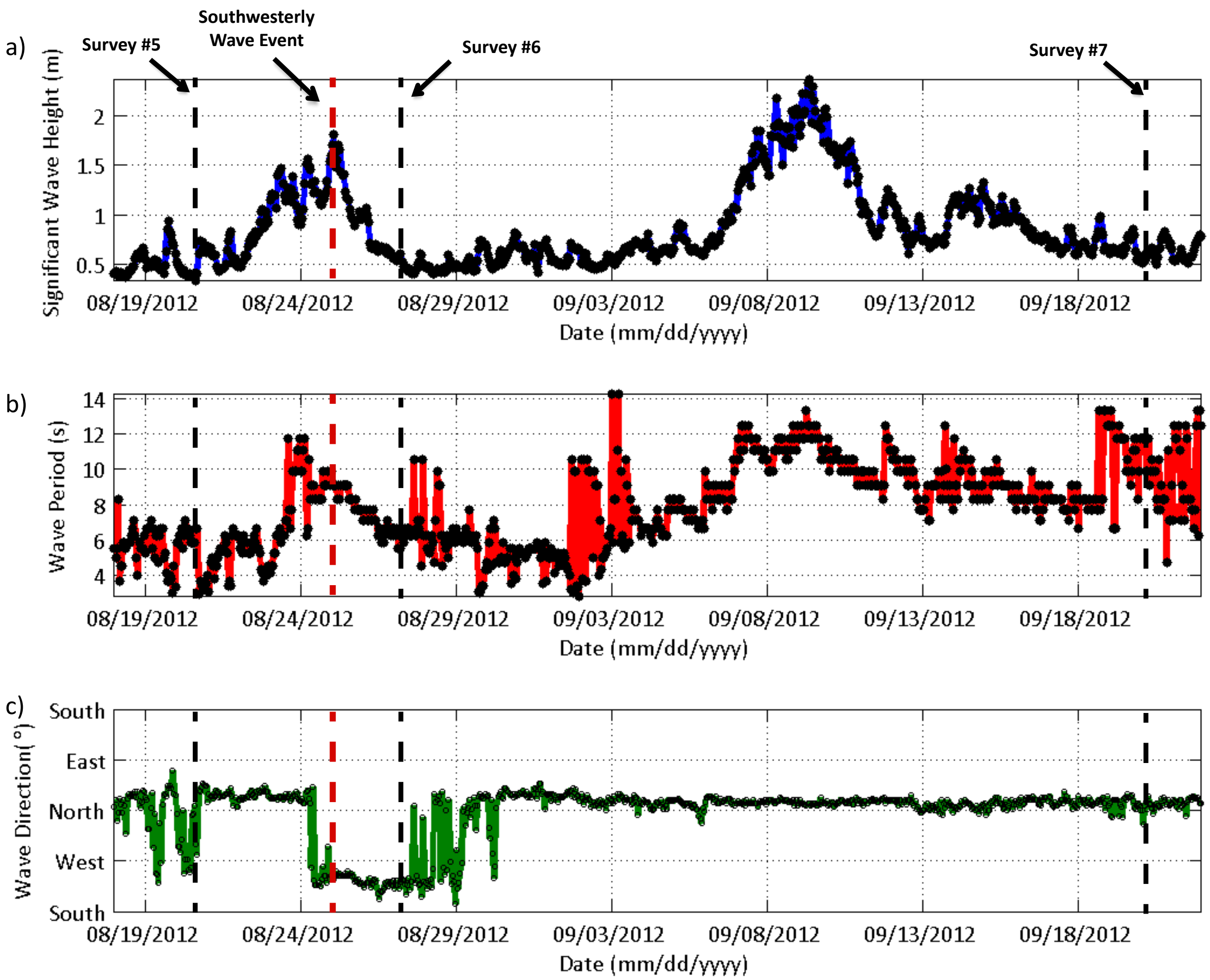

Figure 3.12: Tropical Storm Isaac environmental conditions observed at Rincón offshore buoy: a) significant wave height, b) peak wave period, c) peak wave direction.

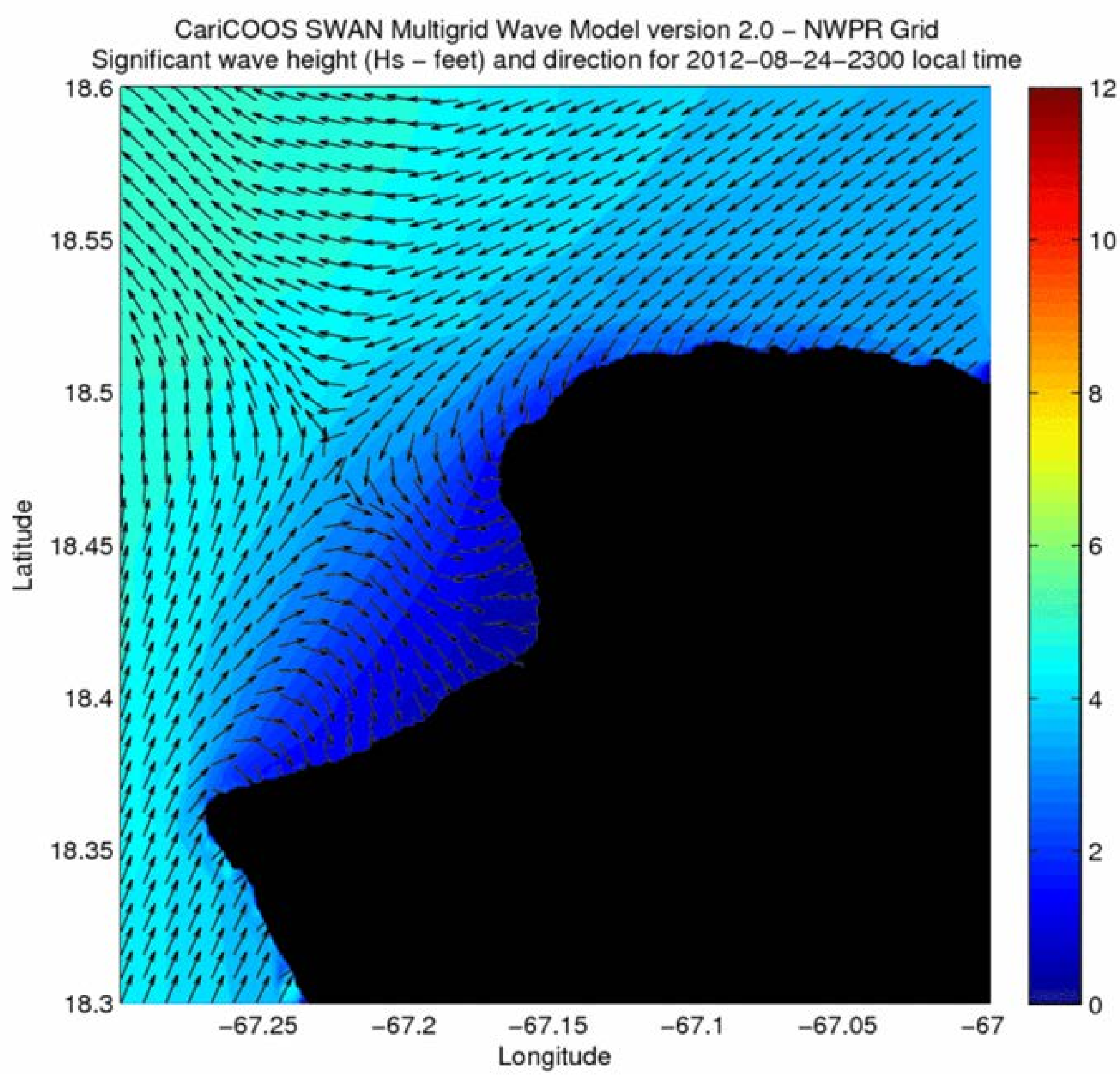

Figure 3.13: CariCOOS Nearshore Wave Model data for Tropical Storm Isaac. This image corresponds to the peak of the southwest wave event, with a significant wave height of 1.8 meters, 9.0 seconds peak period and peak wave direction of 230° as measured at the CariCOOS Rincón wave buoy. Colors denote wave height and the vectors indicate wave direction.

To measure the morphological response of the coast to Tropical Storm Isaac, three separate hydrographic surveys were conducted. One survey was conducted three (3) days before and another three (3) days after the storm. Another survey was conducted 24 days after Isaac, on September 20, 2012, to obtain data that allowed to document the recovery of the seabed. Figure 3.12 shows the date of each of these surveys in relation to the wave data measured at the CariCOOS Rincón wave buoy.

Figures 3.14 to 3.17 show a comparison between the bathymetric data obtained from pre- and post-storm surveys. The baseline bathymetry data, as well as the data from the recovery period, for several of the transects is shown in Figure 3.3. For transects 1 and 4 there is a similar behavior since there is significant sand deposition after the storm (blue line) in the area between 20 to 80 meters away from the coast, suggesting that the sand which eroded from the beach was transported offshore, driven by wave-induced currents. The largest vertical difference was observed in transect 4 (Figure 3.16). Transects 1, 2 and 4 suggest that after 24 days the seabed is already recovering from the severe storm caused by Isaac, and there is clear evidence that the sediment is slowly moving shoreward. These observations agree with anecdotal evidence from residents, who indicated that the beach was already slowly recovering when the last hydrographic survey was conducted.

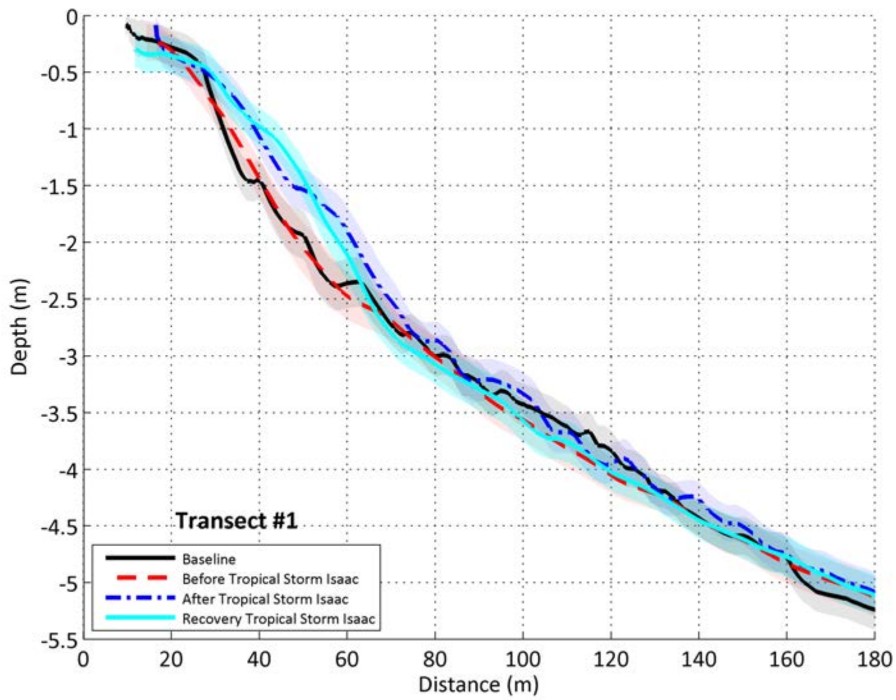

Figure 3.14: Comparison between the baseline bathymetry (black line), pre-storm survey (red line), post-storm survey (blue line) and 24 days after (cyan line) Tropical Storm Isaac in transect 1. The shaded area depicts the 95% confidence level ($\pm 2\sigma$).

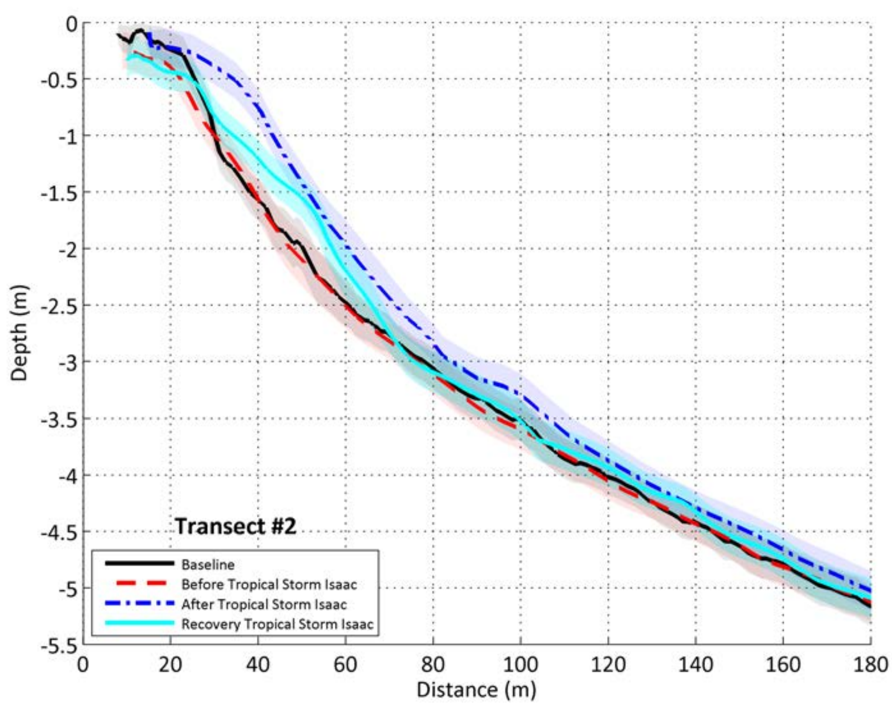

Figure 3.15: Comparison between the baseline bathymetry (black line), pre-storm survey (red line), post-storm survey (blue line) and 24 days after (cyan line) Tropical Storm Isaac in transect 2. The shaded area depicts the 95% confidence level ($\pm 2\sigma$).

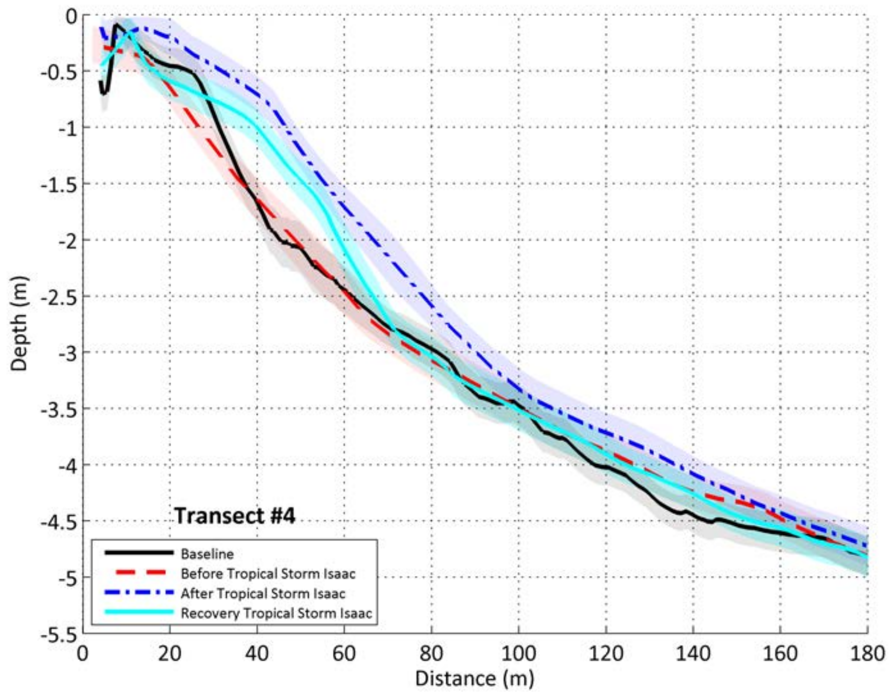

Figure 3.16: Comparison between the baseline bathymetry (black line), pre-storm survey (red line), post-storm survey (blue line) and 24 days after (cyan line) Tropical Storm Isaac in transect 4. The shaded area depicts the 95% confidence level ($\pm 2\sigma$).

Unlike the other profiles, transect 5 (Figure 3.17) shows limited morphological changes. This transect is located in an area with hard substrate (rocky reefs), shown in Figure 1.4. There is a possibility that this underlying geology may have caused this unique behavior. It is evident, as seen in the recovery period profiles, that landward sediment transport occurred when storm waves subside. This dynamic behavior agrees particularly well with the cyclic morphological behavior observed by Ojeda et al. (2010) after storm waves subside. The mentioned sandbars gradually diminish in size and appear to migrate shoreward. Given this evidence about the morphological response of the seabed to Isaac, one can infer that storm waves coming in from a southwesterly direction generate offshore sediment transport, and later on the calm wave conditions cause a slow shoreward sediment transport which helps restore the beach. This result agrees with the onshore and offshore migration of sandbar formations observed by Ruggiero et al. (2009) in sandy beaches of Washington State, USA.

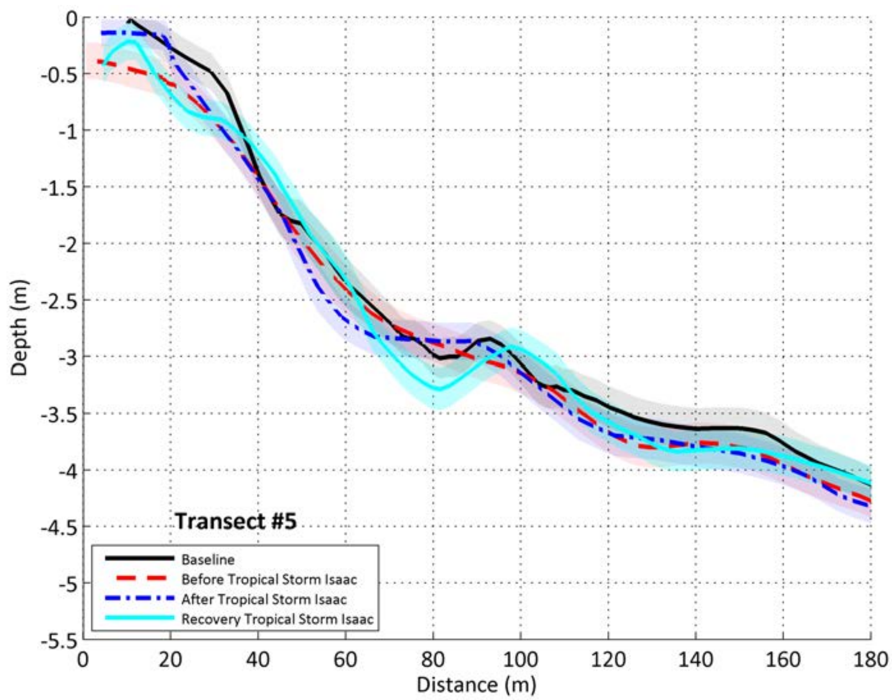

Figure 3.17: Comparison between the baseline bathymetry (black line), pre-storm survey (red line), post-storm survey (blue line) and 24 days after (cyan line) Tropical Storm Isaac in transect 5. The shaded area depicts the 95% confidence level ($\pm 2\sigma$).

3.6.2 Two-dimensional analysis: Tropical Storm Isaac

To quantify the morphological response for each storm event, cumulative accretion and erosion was computed. The morphological response of Tropical Storm Isaac was calculated by subtracting the survey conducted 24 days after Isaac from the baseline bathymetry data. Figure 3.18 shows cumulative accretion/erosion pattern after Tropical Storm Isaac, where the red color (+) indicates accretion, blue (-) indicates erosion and white indicates no morphological change. Along the shoreline, strong sediment deposition was observed seaward of bedrock formations, and some erosion behind them. This behavior appears to be significantly influenced by the geological formation in the study site. In general, this analysis shows the formation of a large shore-parallel sandbar. The nature of this accumulated sand is unknown, although it is likely that at least some of the sand comes from the beach face.

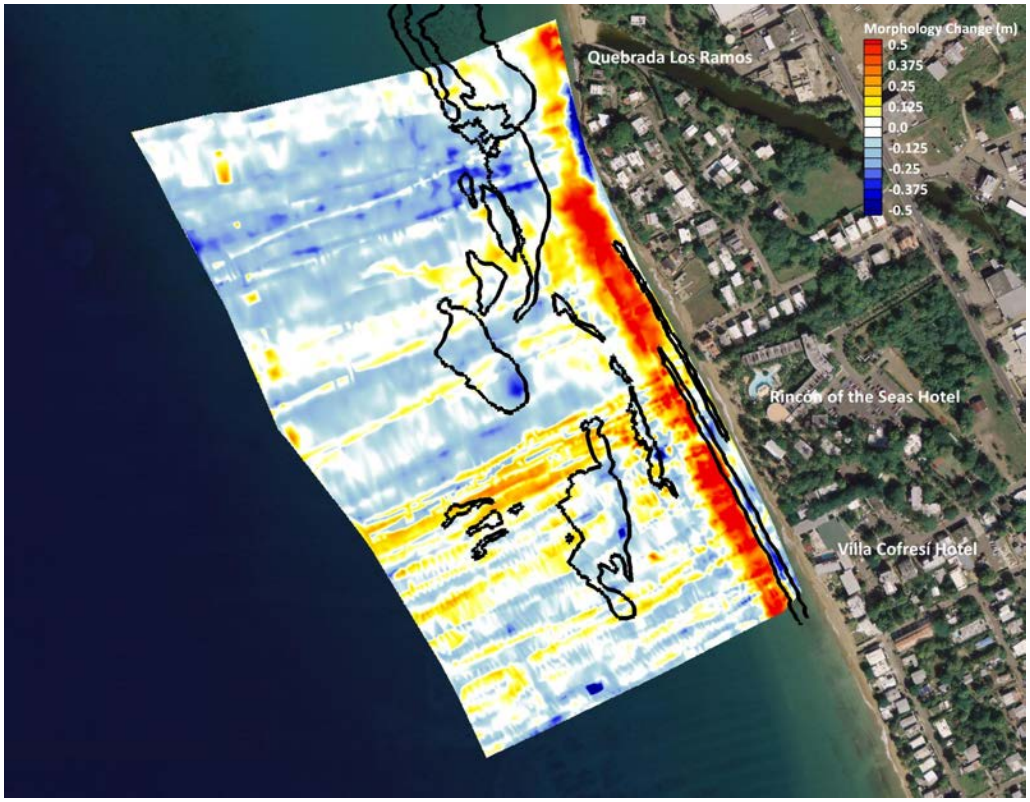

Figure 3.18: Two-dimensional analysis between the baseline bathymetry and the recovery period of Tropical Storm Isaac. The red color (+) indicates accretion, blue (-) indicates erosion, white indicates no morphological change, and black lines mark the presence of hard substrate, as inferred from aerial imagery.

3.6.3 Measurements of the morphological response after Hurricane Sandy

On October 22-23, 2012, Hurricane Sandy was moving as a tropical storm over the Caribbean Sea with maximum sustained winds of 39 knots and a northward trajectory at 2.6 knots (National Weather Service, 2012). The storm continued intensifying, and eventually became a hurricane on October 24. After Sandy made landfall near Cuba, with winds of 96 knots, the system became disorganized and changed its trajectory toward the northwest. Figure 3.19 shows the path of Hurricane Sandy over the Caribbean. Shortly thereafter, on October 25, Rincón began to feel the effects of the hurricane waves coming in from a southwesterly direction. Figure 3.20 shows the output from the CariCOOS Nearshore Wave Model during the peak of the southwest wave event.

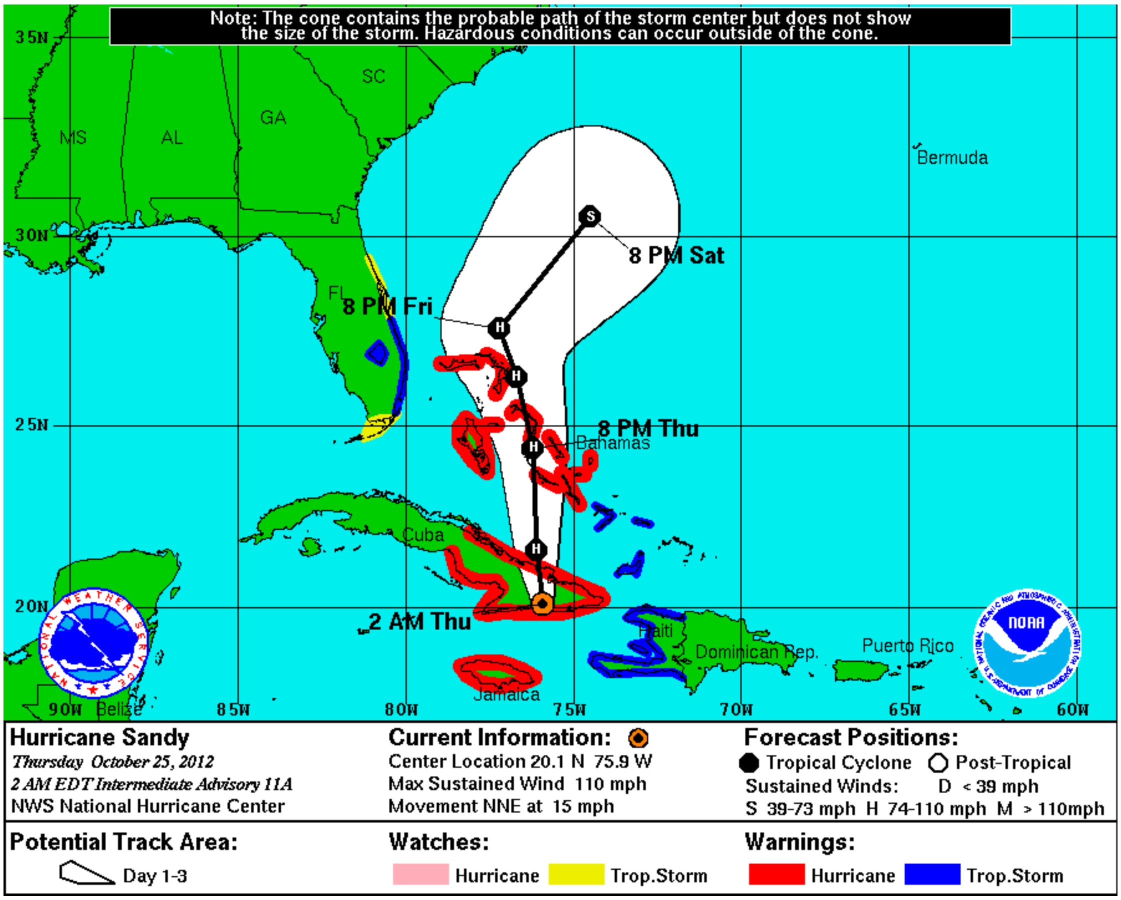

Figure 3.19: Path of Hurricane Sandy over the Caribbean (from the National Weather Service, 2012)

.

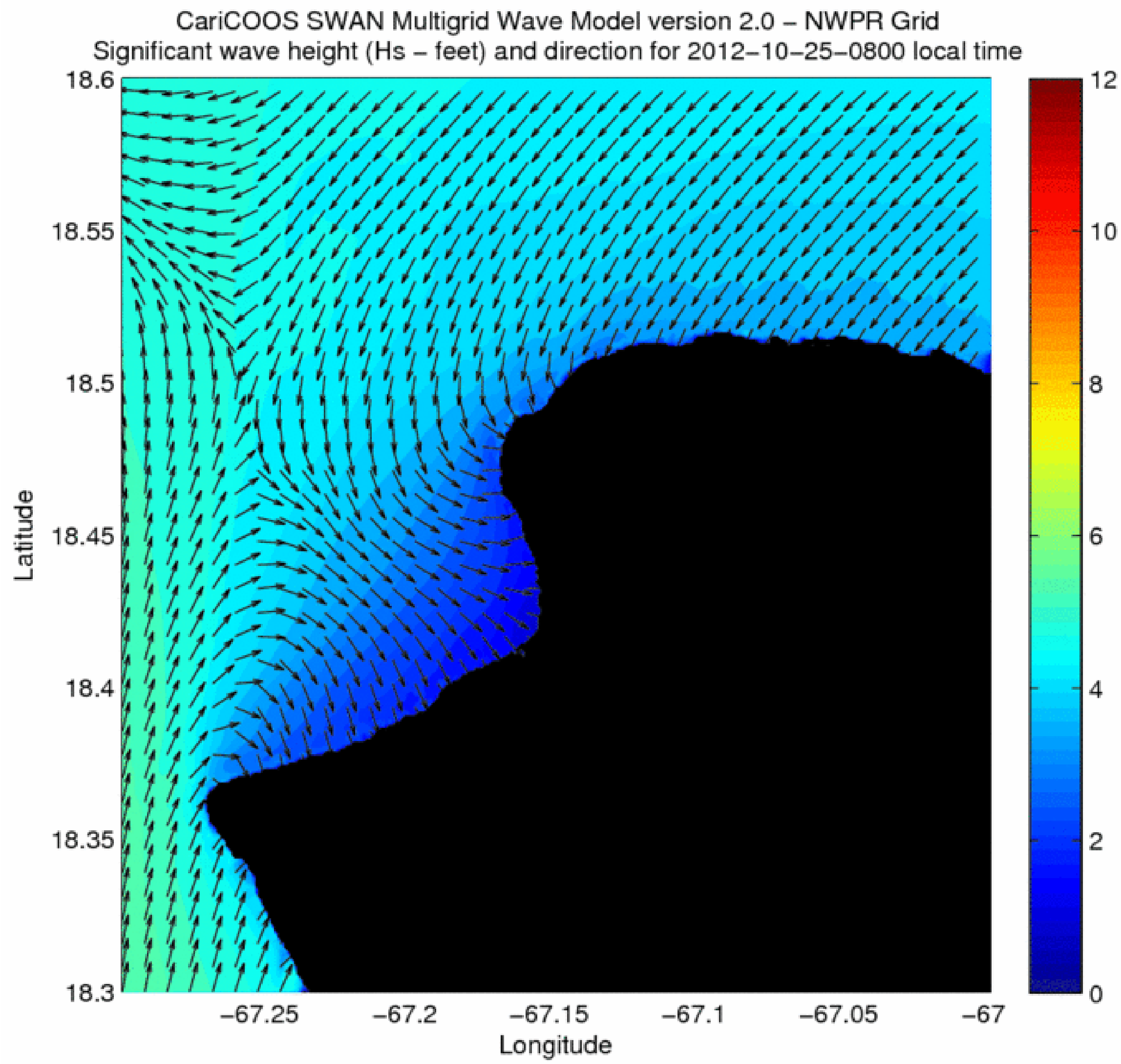

Figure 3.20: CariCOOS Nearshore Wave Model data for Hurricane Sandy on October 25, 2012. This corresponds to the peak of the southwest wave event, with a significant wave height of 1.7 meters, peak period of 11.0 seconds and a peak wave direction of 270° as measured at the CariCOOS Rincón wave buoy. Colors denote wave height and the vectors indicate wave direction.

After briefly weakening to a tropical storm on October 27, Sandy approached a trough, causing the system to re-intensify into a hurricane. A secondary peak was reached on October 29 with maximum sustained winds of 78 knots (National Weather Service, 2012). Figure 3.21 shows the path of Hurricane Sandy after it re-intensified in the Atlantic Ocean. This strengthening caused drastic changes in the swell direction. The waves started coming into Rincón from a northwesterly direction generating peak conditions by October 30. The maximum significant wave height observed at the CariCOOS Rincón wave buoy was of 3.6 meters and a peak period of 12.5 seconds. Figure 3.22 shows the output from the CariCOOS Nearshore Wave Model during the peak of the northwest wave event. Figure 3.23 shows the wave conditions observed at the Rincón buoy during the Hurricane Sandy wave event.

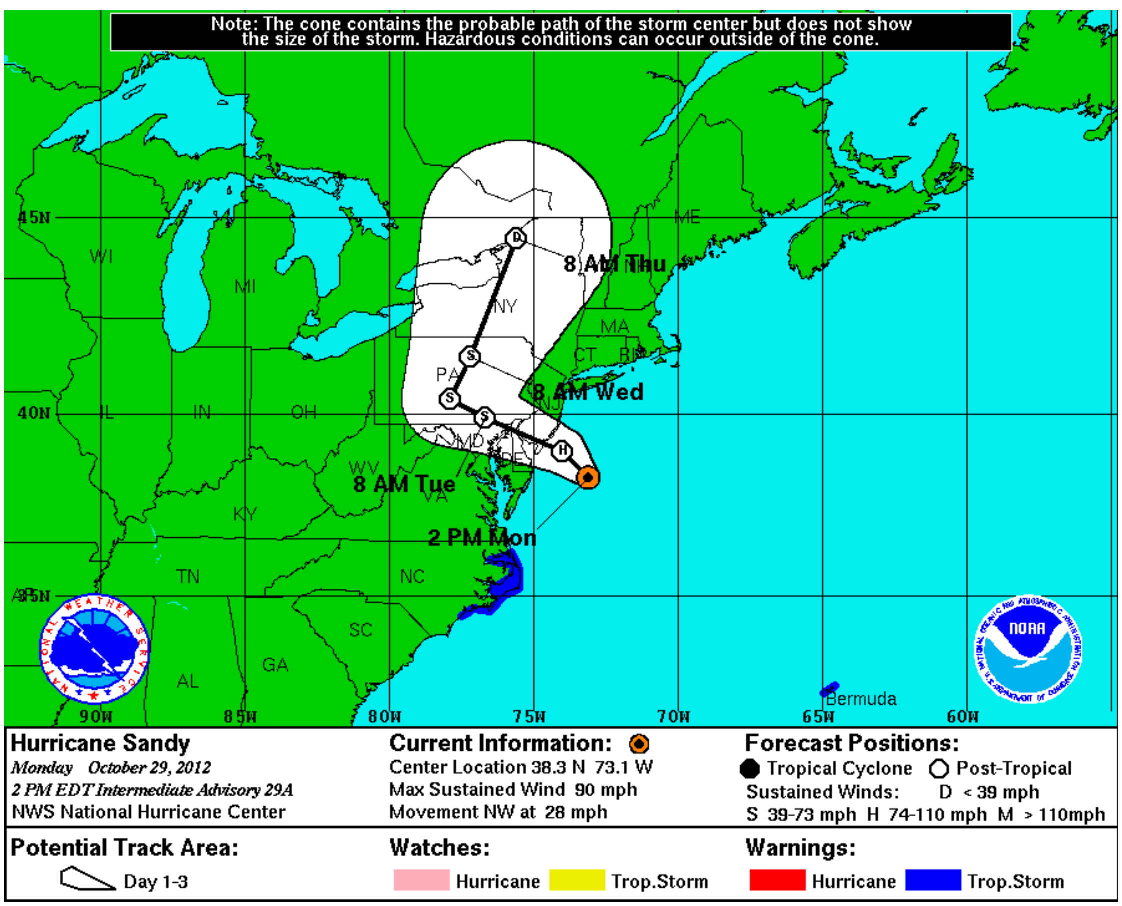

Figure 3.21: Path of Hurricane Sandy after system re-intensified in the Atlantic Ocean (from the National Weather Service, 2012).

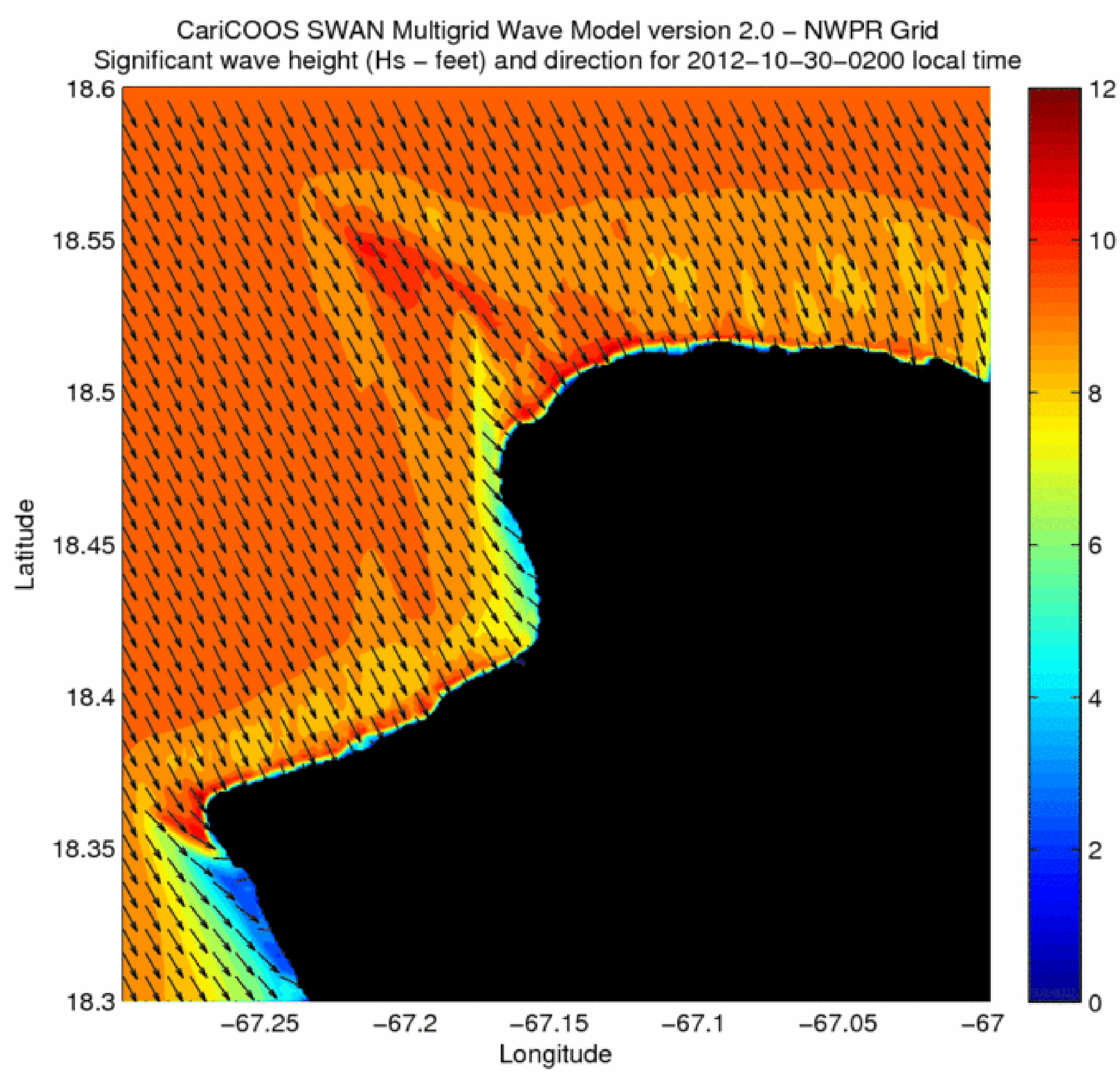

Figure 3.22: CariCOOS Nearshore Wave Model data for Hurricane Sandy on October 30, 2012. This corresponds to the peak of the northwest wave event, with a significant wave height of 3.6 meters, 12.5 seconds peak period and a peak wave direction of 334° as measured at the CariCOOS Rincón wave buoy. Colors denote wave height and the vectors indicate wave direction.

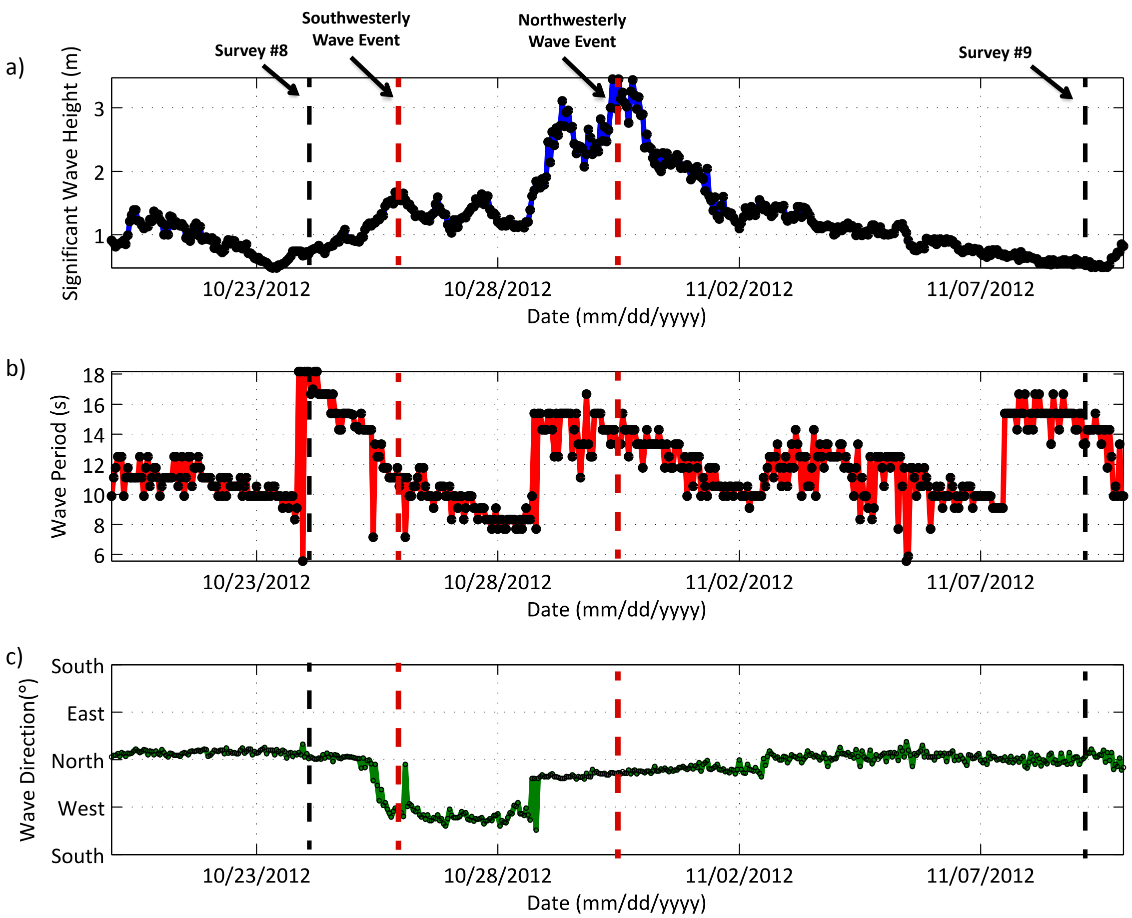

Figure 3.23: Hurricane Sandy wave conditions observed at the Rincón wave buoy: a) significant wave height, b) peak wave period, c) peak wave direction.

To measure the morphological response of Hurricane Sandy, two separate surveys were conducted. One survey was conducted one (1) day before the southwesterly wave event and another ten (10) days after the northwesterly wave event. Due to the rough weather right after the southwest wave event, it was not possible to conduct a hydrographic survey and it was necessary to wait until the northwest storm waves subsided. Figures 3.24 through 3.27 show a comparison between the bathymetric data obtained from pre- and post-Sandy surveys and the baseline bathymetry data.

After the storm waves subsided (blue line), significant sand deposition was observed between 65 to 180 meters away from the coast in each plot for transects 1, 4, and 6. This response suggests that the sand which eroded from the beach face was transported offshore. Moving farther inshore, a smaller difference between the profiles than the Isaac event can be observed, which suggests that sediments began moving shoreward to replenish the coast. The largest vertical difference was observed in transect 5 and as mentioned before this may be due to the underlying geology causing this unique behavior. In this case, significant sand deposition was observed as opposed to the morphological response to Tropical Storm Isaac. Given this evidence about the morphological response of the seabed to Hurricane Sandy, it is inferred that the long period storm waves coming in from a northwesterly direction caused shoreward sediment transport, allowing a faster restoration of the beach compared to the recovery period of Tropical Storm Isaac.

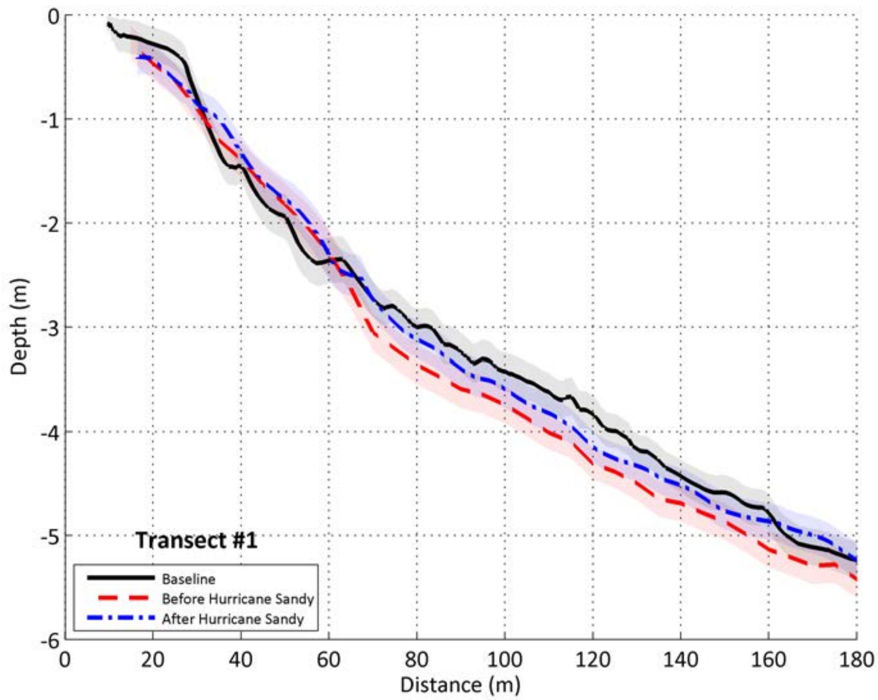

Figure 3.24: Comparison between the baseline bathymetry (black line), pre-storm survey (red line) and post-storm survey (blue line) for Hurricane Sandy in transect 1. The shaded area depicts the 95% confidence level ($\pm 2\sigma$).

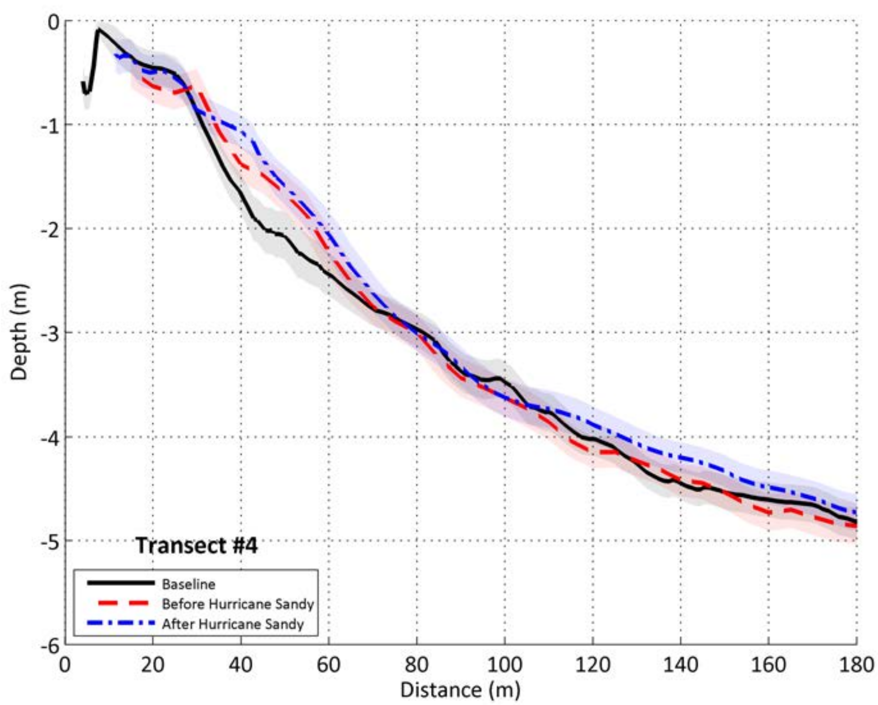

Figure 3.25: Comparison between the baseline bathymetry (black line), pre-storm survey (red line) and post-storm survey (blue line) for Hurricane Sandy in transect 4. The shaded area depicts the 95% confidence level ($\pm 2\sigma$).

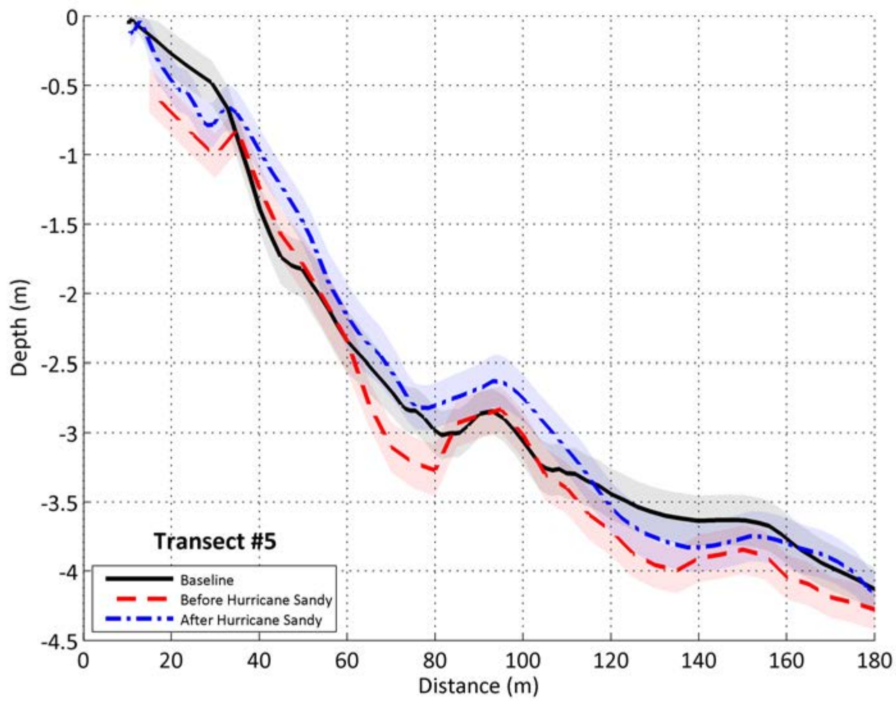

Figure 3.26: Comparison between the baseline bathymetry (black line), pre-storm survey (red line) and post-storm survey (blue line) for Hurricane Sandy in transect 5. The shaded area depicts the 95% confidence level ($\pm 2\sigma$).

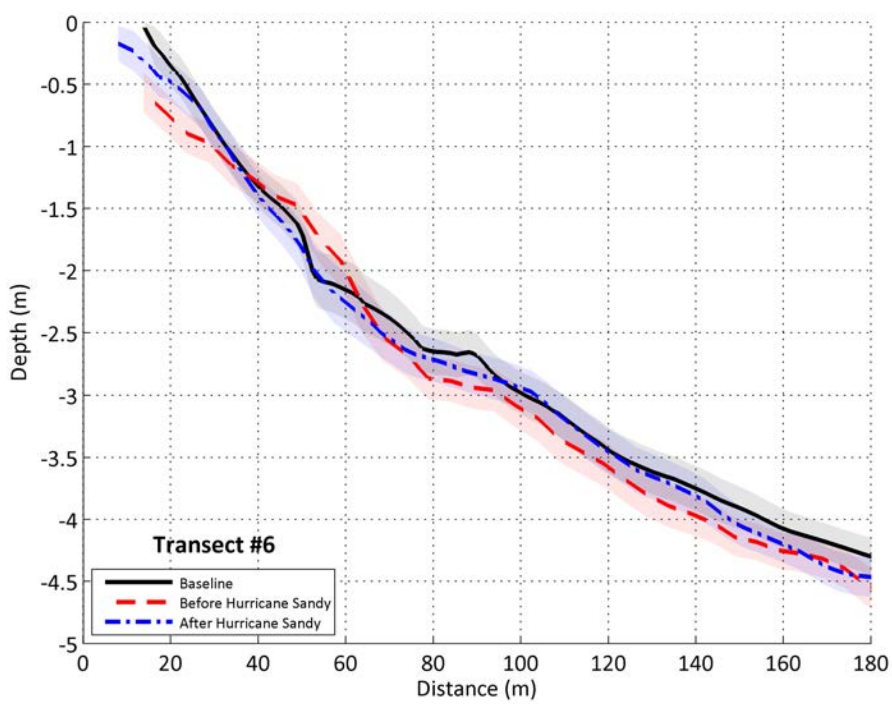

Figure 3.27: Comparison between the baseline bathymetry (black line), pre-storm survey (red line) and post-storm survey (blue line) for Hurricane Sandy in transect 6. The shaded area depicts the 95% confidence level ($\pm 2\sigma$).

3.6.4 Two-dimensional analysis: Hurricane Sandy

The morphological response for Hurricane Sandy was calculated by subtracting the survey conducted after Sandy from the baseline bathymetry data. Figure 3.28 shows the cumulative accretion/erosion pattern after Hurricane Sandy, where the red color (+) indicates accretion, blue (-) indicates erosion and white indicates no morphological change. Along the shoreline, sediment deposition was again observed seaward of bedrock formations, in a pattern very similar to that observed after Tropical Storm Isaac. It is important to recall that the nature of this accumulated sand is unknown, although it is likely that at least some of the sand comes from the beach face, as mentioned earlier on.

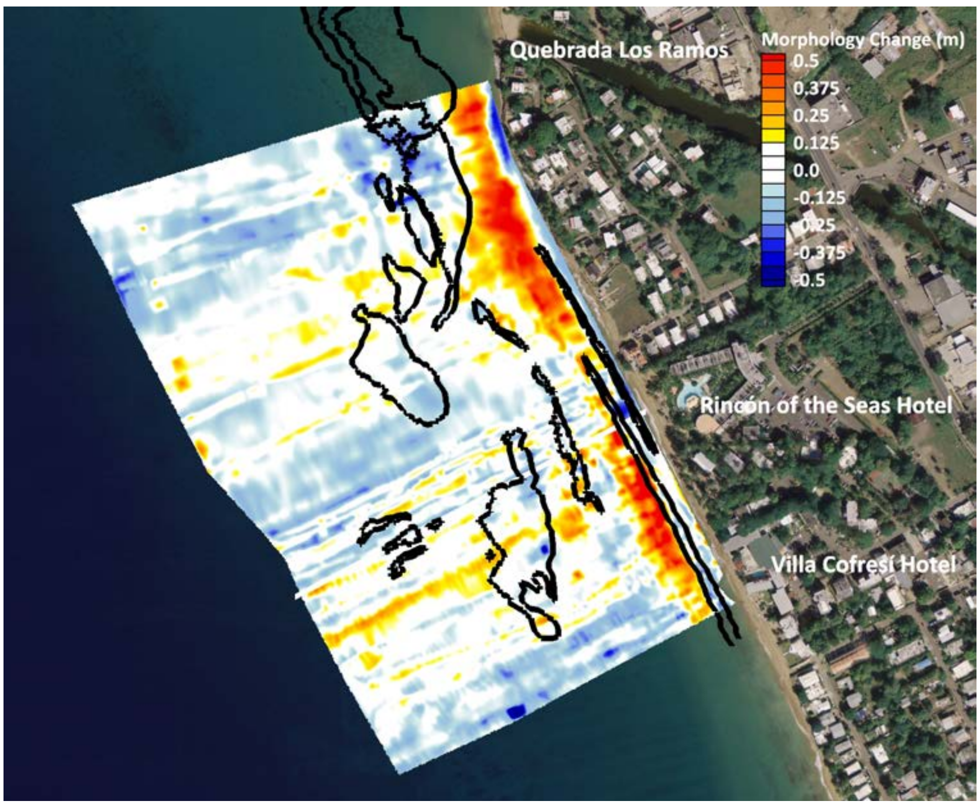

Figure 3.28: Two-dimensional analysis between the survey conducted 24 days after Tropical Storm Isaac and after Hurricane Sandy. The red color (+) indicates accretion, blue (-) indicates erosion, white indicates no morphological change, and black lines mark the presence of hard substrate as inferred from aerial imagery.

3.7 Concluding remarks

This chapter focused on the analysis of field observations in order to understand the response of the nearshore region in the west coast of Rincón, Puerto Rico to storm events. The developed jetski-based bathymetric surveying system was able to measure short-term nearshore morphology change caused by Tropical Storm Isaac and Hurricane Sandy with vertical errors less that 0.1 m. It should be noted that this is the first time that the surf zone of Puerto Rico has been monitored in order to observe short-term morphological changes. The bathymetric data allowed quantification of the morphological response to the action of storm waves during the study period. The main observations that can be obtained from these field surveys can be summarized as follows:

- The southwesterly wave events caused by Isaac and Sandy generated significant offshore sediment transport and the formation of large shore-parallel sandbars.
- This offshore sediment transport observed in the subaqueous region agrees with photographic evidence which shows significant erosion of the beach face as a result of these two storms.
- It is hypothesized that at least some of the sand which was observed to have accumulated in the nearshore zone may have come from the eroded beach face.
- The northwesterly wave event caused by Sandy appears to have transported some of the eroded sediment during the Sandy southwesterly wave event in the shoreward direction.
- The presence of hard substrate seems to play a large role in the nature of sediment transport in the study area, although more research should be conducted to evaluate this role.

Although the short-term morphology change of Rincón was analyzed with only two storms, one can hypothesize that southwesterly wave events will, in general, generate offshore sediment transport. This may lead to a possible loss of nearshore sand, and northerly long-period waves may help replenish the beach. In the following chapter, an attempt is made at simulating storm-induced sediment transport in the study area in response to Tropical Storm Isaac and Hurricane Sandy, and a comparison is made between the simulation results and the erosion and accretion patterns discussed in the present chapter.

Chapter 4

NUMERICAL MODELING OF STORM-INDUCED NEARSHORE MORPHOLOGY CHANGE IN RINCÓN, PUERTO RICO

The material presented in this chapter is an expanded version of the article *"Numerical modeling of storm-induced nearshore morphology change in Rincón, Puerto Rico"* by Patricia Chardón and Miguel Canals, which has been submitted to a peer-reviewed scientific journal.

4.1 Introduction

The coastal zone of Rincón, Puerto Rico is a complex and dynamic system, dominated by a highly energetic and varied wave climate. The most significant wave events are generated by tropical storms or hurricanes as well as North Atlantic winter storms. In this chapter, a coupled wave-current-sediment transport numerical model, the Coastal Modeling System (CMS), developed by the U.S. Army Corps of Engineers (Sánchez et al., 2012), was implemented in order to simulate the morphological response of the seabed in the vicinity of several Rincón beaches to the significant wave events caused by Tropical Storm Isaac and Hurricane Sandy. These two events affected the study area during the 2012 hurricane season, as explained in the preceding chapter. The ability of the model to reproduce the region's hydrodynamics was evaluated using observations of nearshore current velocities obtained with an acoustic Doppler current profiler (ADCP). The model reproduced very well the strong wave-induced flows which are believed to dominate sediment transport in Rincón. As explained in the preceding chapter, using a jetski-based bathymetric surveying system, the storm-induced nearshore morphology changes generated by both Tropical Storm Isaac and Hurricane Sandy were measured and quantified. The computed morphological changes qualitatively agreed with the large-scale erosion and accretion patterns observed in the bathymetric surveys, which were presented in the preceding chapter.

4.2 The Coastal Modeling System

The Coastal Modeling System (CMS), developed by the United States of America Corps of Engineers (USACE), is an integrated modeling system for simulating nearshore waves, currents, water levels, sediment transport, and morphology change (Sánchez et al., 2012). CMS includes a flow model (CMS-Flow) and a spectral wave model (CMS-Wave). CMS-Flow is a two-dimensional depth-averaged nearshore circulation model, which calculates hydrodynamics and sediment transport. CMS-Wave is a spectral wave transformation (phased-averaged) model solving the wave-action balance equation using a forward marching Finite Difference Method (Sánchez et al., 2012). The wave and circulation models are coupled in order to compute morphology change in the presence of complex coastal processes, as shown in Figure 4.1. The next section briefly describes the governing equations and the mathematical basis for each of the two models: CMS-Flow and CMS-Wave. For a detailed description of the equations, parameters and algorithms please refer to Coastal Modeling System User Manual (Sánchez et al., 2012).

4.2.1 CMS-Flow model

The CMS-Flow model solves the two dimensional, depth-integrated continuity and momentum equations using the finite-volume method. The depth-integrated continuity equation is written as

$$\frac{\partial h}{\partial t} + \frac{\partial (hV_j)}{\partial x_j} = 0 \tag{4.1}$$

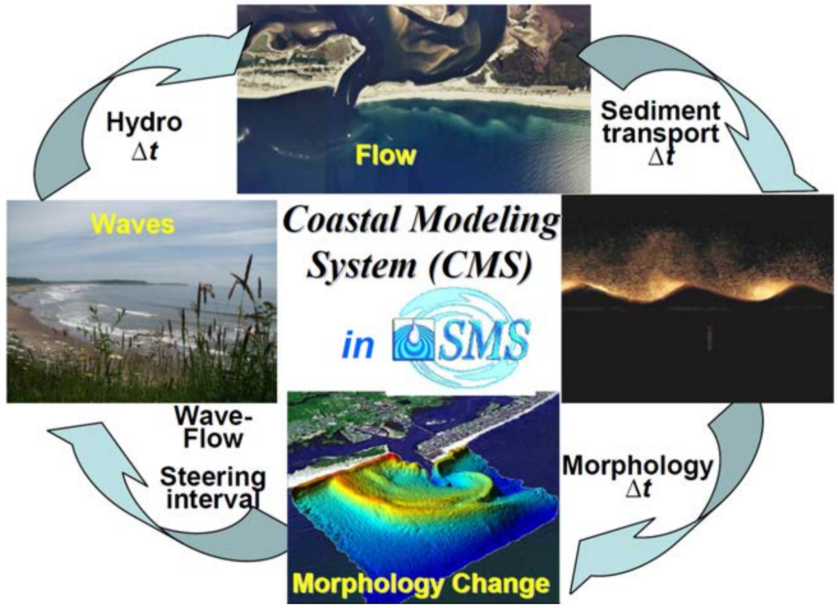

Figure 4.1: CMS modeling framework, from Sánchez et al. (2012).

and the two-dimensional momentum equation is given by

$$\frac{\partial(hV_i)}{\partial t}+\frac{\partial(hV_iV_j)}{\partial x_j}=-gh\frac{\partial\eta}{\partial x_i}-\frac{h}{\rho}\frac{\partial p_a}{\partial x_i}+\varepsilon_{ij}f_chU_j+\frac{\partial}{\partial x_j}\left(\nu_t h\frac{\partial V_i}{\partial x_j}\right)-\frac{1}{\rho}\frac{\partial}{\partial x_j}(S_{ij}+R_{ij}-\rho hU_{wi}U_{wj})+\tau_{si}-\tau_{bi} \tag{4.2}$$

where $h=\zeta+\eta$ is the total water depth, as shown in Figure 4.2; $V_i=U_i-U_{wi}$ is the wave-averaged depth-integrated mass flux velocity; U_i is the phase- and depth-averaged current velocity; U_{wi} is the depth-averaged wave velocity; g is the gravitational constant; f_c is the Coriolis parameter; p_a is the atmospheric pressure; ρ_0 is a reference water density; ν_t is the turbulent eddy viscosity; τ_{si} is the surface wind stress; τ_{bi} is the combined wave-current mean bed shear stress ; ε_{ij} is the permutation parameter. The stresses induced by breaking wave bores are included as a roller stress term, $R_{ij}=2E_rw_iu_j$, where E_r is the surface roller energy. These stresses can generate significant wave induced currents and surface wave setup (Calvete et al., 2012). The term S_{ij} represents the wave radiation stress:

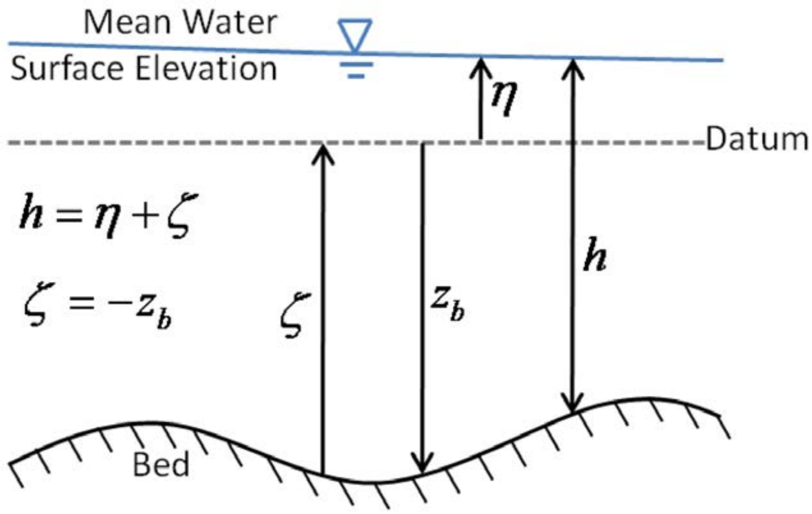

Figure 4.2: CMS vertical coordinate system, from Sánchez et al. (2012).

$$S_{ij} = \int \int E_w \left[n w_i w_j + \delta_{ij} \left(n - \frac{1}{2} \right) \right] df d\theta \tag{4.3}$$

where f is wave frequency (s^{-1}); θ is the wave direction; δ_{ij} is the Kronecker delta; and $n = \frac{1}{2}\left(1 + \frac{2kh}{sinh2kh}\right)$. The stresses associated with wave forcing are provided to CMS Flow by the CMS Wave model through a steering mechanism. The CMS Wave model is explained below.

4.2.2 CMS-Wave model

Phase-averaged models can take into account most of the significant shallow-water processes, e.g., depth refraction and shoaling, current, quadruplet and triad interactions, wind input, whitecapping, depth-induced breaking, and bottom friction (Booji et al., 1999; Ris et al., 1999). The CMS-Wave model solves the two-dimensional variation of spectral wave energy in space using the following equation (Lin and Demirbilek, 2012):

$$\frac{\partial N}{\partial t}+\frac{\partial \dot{C}_{gx}N}{\partial x}+\frac{\partial \dot{C}_{gy}N}{\partial y}+\frac{\partial \dot{C}_{g\theta}N}{\partial \theta}=\frac{\varepsilon}{\omega'}\left\{\frac{\partial}{\partial x}\left(\dot{C}_g\frac{\partial N}{\partial x}\right)+\frac{\partial}{\partial y}\left(\dot{C}\dot{C}_g\frac{\partial N}{\partial y}\right)+\dot{C}\dot{C}_g\frac{\partial^2 N}{\partial \theta^2}\right\}+S \tag{4.4}$$

where $\dot{C}$ is the wave celerity; $\dot{C}_g$ is the group celerity, defined as $\dot{C}_g = \frac{\partial \omega'}{\partial k}$; $\dot{C}_{gx}$, $\dot{C}_{gy}$, and $\dot{C}_{g\theta}$ are the characteristic wave velocities with respect to x, y, and θ; $\omega^{'}$ is the wave relative frequency; θ is wave direction; k is the wave number; S denotes the sources and sinks; ε is the coefficient of directional diffusion of wave energy and is on the order of 10^{-4}, while N is the wave-action density, defined as $N = \frac{E}{\omega'}$, where E is the wave energy as a function of frequency and direction. The spectral action balance equation, shown above, describes the evolution of wave energy in coastal regions taking into account wind energy input, energy dissipation due to bottom friction, nonlinear wave-wave interactions, wave-current interactions as well as diffraction, refraction and shoaling (Zhang et al., 2003). The wave-current interaction is calculated based on the dispersion relationship which takes into account wave blocking due to an opposing current (Larson et al., 2002). This interaction is based on the characteristic velocities $\dot{C}_{gx}$, $\dot{C}_{gy}$, and $\dot{C}_{g\theta}$, which are expressed as:

$$\dot{C}_{gx} = \dot{C}_g \cos\theta + U \tag{4.5}$$

$$\dot{C}_{gy} = \dot{C}_g \sin\theta + V \tag{4.6}$$

$$\dot{C}_{g\theta} = \left(\frac{\partial k}{\partial y}\cos\theta - \frac{\partial k}{\partial x}\sin\theta\right) \tag{4.7}$$

To compute wave breaking, CMS applies the Miche (1951) criterion for random waves, in which the wave breaking threshold, H_b, is given by:

$$H_b \leq \frac{0.64}{k_p} \tanh(k_p h) \tag{4.8}$$

where k_p is the wave number corresponding to the spectral peak period, T_p.

Sediment parameters

CMS-Flow calculates sediment transport rates and morphology change through gradients in the sediment transport rates. Three sediment transport models available in CMS are: equilibrium total load, equilibrium bed load plus advection-diffusion for suspended load, and non-equilibrium total load (NET). For this study, the NET formula was used to carry out the computations because it allows the use of an implicit numerical integration technique as well as the capability to use a telescoping Cartesian grid. The implicit solver supports longer integration time steps which are very useful for long-term hydrodynamics and sediment transport calculations (Sánchez et al., 2012). The telescoping grid provides the ability to refine the grid cell size in areas of interest and/or regions where complicated geometry or large horizontal gradients are expected.

The NET model is based on the assumption that neither the bed nor the suspended loads are in equilibrium. This model separates the sediment transport into wave and current related components. Combining the current-related bed and suspended transport into a single equation, the NET defines the two-dimensional sediment transport equation as:

$$\frac{\partial}{\partial t}\left(\frac{hC_{tk}}{\beta_{tk}}\right) + \frac{\partial(U_j h C_{tk})}{\partial x_j} = \frac{\partial}{\partial x_j}\left[\nu_s h \frac{\partial(r_{sk} C_{tk})}{\partial x_j}\right] + \alpha_t w_{sk}(C^*_{tk} - C_{tk}) \tag{4.9}$$

Here, U_j is the depth-averaged current velocity; C_{tk} is the depth-averaged total-load sediment concentration for size class $\mathbf{k}$; C^*_{tk} is the depth-averaged total-load equilibrium concentration; β_{tk} is the total-load correction factor that accounts for the time lag between flow and sediment transport because the bed load travels at a slower velocity than the depth-averaged current; r_{sk} is the fraction of suspended load in the total load for size class $\mathbf{k}$; ν_s is the horizontal sediment mixing coefficient;

α_t is the total-load adaptation coefficient; and w_{sk} is the sediment fall velocity for size class $\mathbf{k}$. The present study used the assumption that the sediment grain size is homogeneous, as a result, **k**=1. For this study, the actual depth-averaged total-load sediment concentration, C_t, which is to be solved for in the NET transport equation described above is:

$$C_t = \frac{q_t}{Uh} = \frac{q_s + q_b}{Uh} \tag{4.10}$$

where q_s and q_b are the actual suspended and bed load sediment transport. The equilibrium depth-averaged total-load sediment concentration, C_t^*, is given by:

$$C_t^* = \frac{q_t^*}{Uh} = \frac{q_s^* + q_b^*}{Uh} \tag{4.11}$$

where q_s^* and q_b^* are the equilibrium suspended and bed load sediment transport rates, respectively. To calculate the near-bed equilibrium sediment transport rates required to solve the NET sediment transport equation, three (3) transport capacity formulas are available in the CMS model: Watanabe, Lund-CIRP and Van-Rijn, which are briefly described below. The simplest model for near-bed equilibrium sediment concentration is the Watanabe formulation, in which the total suspended and bed load transport, q_{tot}^{*Wat}, is given by Sánchez et al. (2012):

$$q_{tot}^{*Wat} = A\left[\frac{(\tau_{b,max} - \tau_{cr})U_c}{\rho_w g}\right] \tag{4.12}$$

where $\tau_{b,max}$ is the maximum shear stress at the bed; τ_{cr} is the shear stress at incipient sediment motion; U_c is the depth averaged current velocity; ρ_w is the density of water; g is the acceleration of gravity; and A is an empirical coefficient that typically ranges from 0.1 to 2 and which depends on wave properties and sediment type (Paolo, 2012). The second model available in CMS is the Lund-CIRP formulation, in which the equilibrium bed load transport (q_b^{*LC}) formulation developed by Camenen and Larson (2005) is defined as:

$$\frac{q_b^{*LC}}{\sqrt{(s-1)gd_3^{50})}} = f_b\rho_s 12\sqrt{\theta_c}\theta_{cw,m}e^{\left(-4.5\frac{\theta_{cr}}{\theta_{cw}}\right)} \tag{4.13}$$

where s is the sediment specific gravity; d_{50} is the median grain size; ρ_s is the sediment density (2,650 kg m^{-3}); f_b is the bed-load scaling factor; and $\theta_{cw,m}$ and θ_{cw} are the mean and maximum Shields parameter for waves and currents. The equilibrium suspended load transport (q_s^{*LC}) for the Lund-CIRP formulation is expressed as:

$$\frac{q_s^{*LC}}{\sqrt{(s-1)gd_3^{50})}} = f_s\rho_s c_R U\frac{\varepsilon_s}{w_s}\left[1-e^{\left(-\frac{w_s}{\varepsilon_s}\right)}\right]. \tag{4.14}$$

Here, w_s is the sediment fall speed; c_R is the reference sediment concentration; and ε_s is the sediment mixing coefficient. The third available equilibrium transport model is the Van Rijn formulation, in which the equilibrium bed load transport, q_b^{*vR}, is defined as:

$$q_b^{*vR} = f_b 0.015\rho_s Uh\left(\frac{U_e-U_{cr}}{\sqrt{(s-1)gd_{50})}}\right)^{1.5}\left(\frac{d_{50}}{h}\right)^{1.2} \tag{4.15}$$

and the suspended-load transport as:

$$q_s^{*vR} = f_b 0.012\rho_s Ud_{50}\left(\frac{U_e-U_{cr}}{\sqrt{(s-1)gd_{50})}}\right)^{2.4} d_*^{-0.6} \tag{4.16}$$

where U is the depth-averaged current velocity; U_{cr} is the critical depth-averaged velocity necessary for initiation of motion; U_e is the effective depth averaged velocity calculated as $U_e = U + 0.4u_w$; u_w is the wave bottom shear velocity; f_s is the suspended-load scaling factor; and f_b is the bed-load scaling factor.

To calculate the sediment concentration and morphology changes in the present study, the Lund-Cirp transport formula was selected. This formula does well in predicting the surf zone sediment transport but tends to overestimate the transport rates near the wetting and drying limit and in deep water (>10 m) (Sánchez et al., 2012). The mean sediment particle size used in the present study is d_{50} = 0.18 mm, obtained by Vélez (2013).

The NET model incorporates a parameter defined as the adaptation length, which quantifies the distance that the sediment requires to reach a new equilibrium concentration. This adaptation length may be calculated as (Sánchez et al., 2012):

$$L_t = r_s L_s + (1 - r_s) L_b \tag{4.17}$$

where L_s and L_b are the suspended and bed transport adaptation lengths, respectively, and r_s is the suspended sediment fraction. There is some guidance in the selection of values for these adaptation lengths, for example, the bed transport adaptation lengths are related to the smallest scale bedforms expected in the study area, while the total adaptation length should be chosen depending on the smallest grid resolution of the model grid (Sánchez et al., 2012) as well as by a trial and error procedure. The adaptation length is an important parameter in the morphology change modeling; the smaller the value, the closer the model is to an equilibrium transport. In the case of this study, spatially constant total adaptation length of 10 meters was selected, based on the spatial scales and the grid resolution. Table 4.1 summarizes the parameters of the sediment transport model used for the study.

In the study area there is a mix of bottom types varying between rocky bottom, sand, and coral reef areas (Figure 1.4). The CMS sediment transport model allows for the hard-bottom areas to be assigned a non-erodible seabed boundary condition, and this was implemented by estimating hard-bottom areas from visual analysis of aerial imagery of the area.

4.3 Model setup

To perform accurate simulations of hydrodynamics and sediment transport, the two most important data sources are very high quality bathymetry data and high-quality boundary conditions to force the model. Before 2008, ocean observations in Puerto Rico were very limited, and very

Table 4.1: Sediment transport parameters

Parameter	Value
Formulation	Advection-Diffusion
Sediment density (kg m-3)	2650.0
Sediment transport formula	Lund-CIRP
Bed load scaling factor	1.0 (default)
Suspended load scaling factor	1.0 (default)
Morphologic acceleration factor	1.0 (default)
Bed slope coefficient	1.0 (default)
Sediment porosity	0.40 (default)
Transport grain size, d_{50} (mm)	0.18
Total load adaptation length method	Constant
Total load adaptation length (m)	10.0

little data was available to force coastal models. The Caribbean Coastal Ocean Observing System (CariCOOS) was developed in 2008, and since then CariCOOS efforts have led to the deployment of three full data buoys in San Juan, Ponce, and the USVI, as well as a directional Datawell Waverider buoy in Rincón (CariCOOS, 2008). In addition, a network of 13 hurricane-hardened meteorological stations has been placed in Puerto Rico and the United States Virgin Island. Figure 4.3 shows a map of all CariCOOS ocean observing assets.

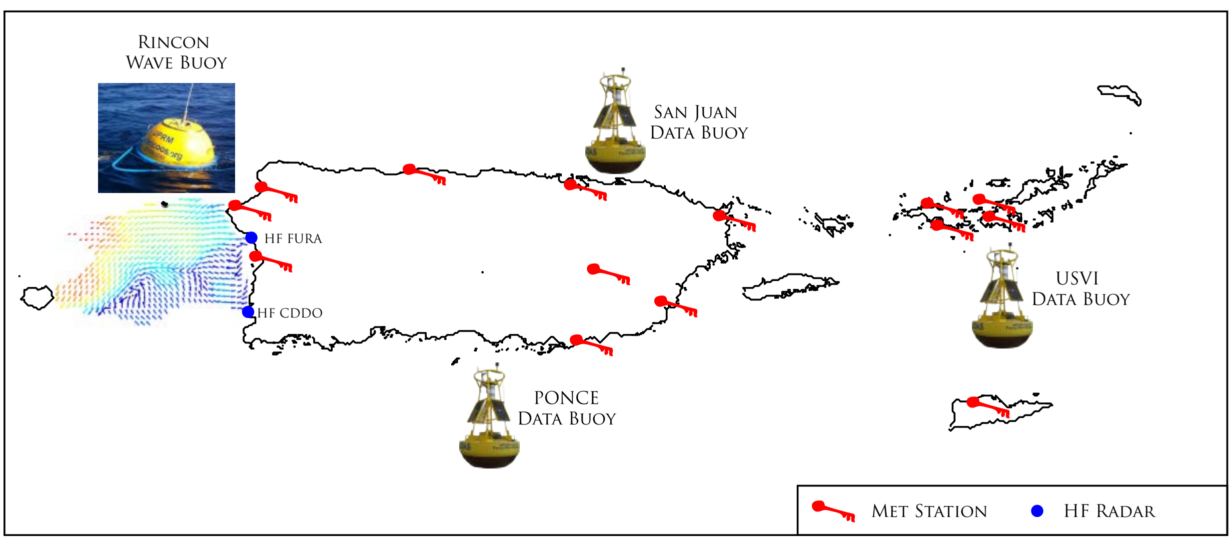

Figure 4.3: CariCOOS ocean observing assets.

The presence of these assets has allowed the use of high-quality data to force the numerical model, particularly wave and wind data from sensors within the model computational domain. Table 4.2 summarizes the physical forcing used in the simulations and the source of this data.

Table 4.2: Summary of model forcing and data source

Forcing variable	Data source	Forcing type
Tidal data	Earth and Space Research Tide Model Driver (TMD) (Padman, 2005)	Temporally and spatially variable
Wind magnitude and direction	WRF wind model, CariCOOS Rincón anemometer	Temporally variable and spatially constant
Sediment D_{50}	Granulometry by Vélez (2013)	Temporally and spatially constant
Wave parameters	CariCOOS Rincón directional wave buoy	Temporally and spatially variable

During all simulations, the CMS-Flow hydrodynamic time step was specified at one (1) hour with sediment transport, water surface elevations, and wind forcing activated. This large time step was possible due to the implicit solution scheme, which also reduces the total computational time needed to complete the simulation (Sánchez et al., 2012). The momentum equation (Equation 4.2) included advection, mixing terms, and wall friction. The default Manning's bottom friction coefficient of 0.025 was kept constant over the domain. Wetting and drying was allowed because sloped beaches and/or sand bars change with time causing cells to become wet or dry at different times. With this setup, the two storm events were simulated to understand storm-induced nearshore morphology changes. The simulation duration for Tropical Storm Isaac was of 768 hours, and 504 hours for Hurricane Sandy.

Figure 4.4 shows the bathymetry used in the computational domain for both model grids. The existing USGS LIDAR bathymetry (Taylor et al., 2008) and the baseline bathymetry obtained using the jetski-based surveying system were merged in order to create a continuous bathymetry dataset to provide the grid bathymetry for the simulations. Two Cartesian grids were generated due to limitations of the implicit solver; for the CMS-Flow model a quadtree (telescoping) grid and for the CMS-Wave model a non-uniform Cartesian grid. Spatial interpolation to pass information from one model grid to another was executed by the CMS-Flow and CMS-Wave coupling procedure.

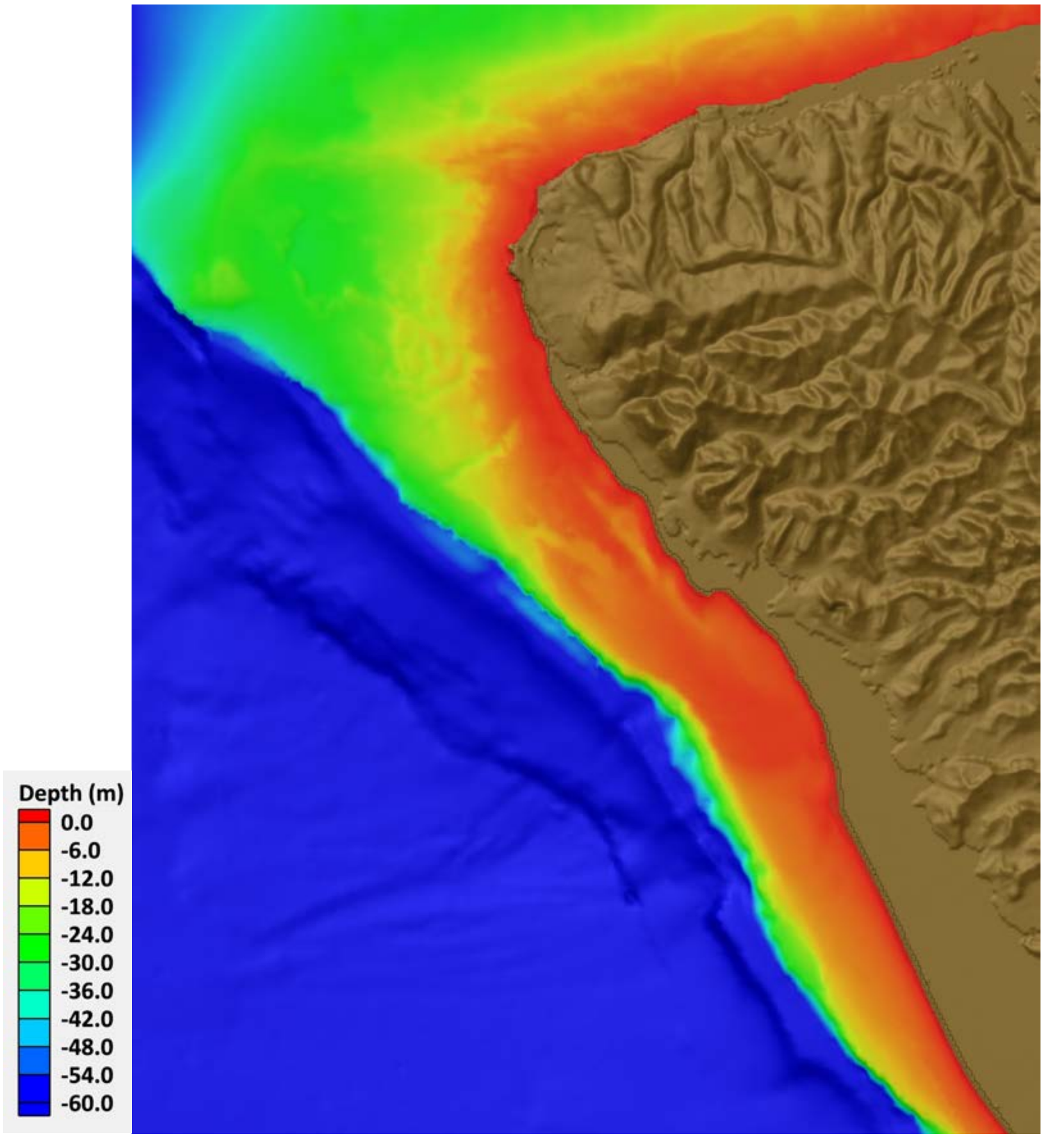

Figure 4.4: Merged bathymetry of the CMS-Flow and CMS-Wave computational domain, colors represent depth in meters.

4.3.1 CMS-Flow setup

A nested approach was used to apply tidal boundary conditions. This is because it is difficult to obtain good results of tidal flows and elevation in grids with a small spatial extent. For CMS-Flow, a large coarse resolution grid was developed with the sole purpose of simulating tides. This coarse grid then provided tidal boundary conditions to the child grid. The child grid consists of a very high-resolution telescoping grid and is the main grid used in the simulations presented in this study. In addition to the tidal forcing, wind and wave forcing was then applied to this child grid. A sketch of the nested grid approach is shown in Figure 4.5.

The high-resolution CMS domain extends approximately 6.8 kilometers alongshore and 4.0 kilometers offshore. The telescoping grid allowed variable spatial resolution, providing the ability to refine the grid cell size in areas of interest and/or regions where large horizontal gradients in wave height or current velocity were expected. The spatial grid resolution ranges from 16 meters offshore to a maximum of 1 meter in the nearshore area. Figure 4.6 shows the generated telescoping grid for CMS-Flow, including details of the model grid in the nearshore region. This range in resolution illustrates the advantage of this type of grid providing the ability of solving hydrodynamic phenomena at varying scales, while optimizing computational effort by reducing grid cells in areas in which very high spatial resolution is not necessary, such as in the open ocean.

Tidal boundary conditions

Water surface elevation boundary conditions were assigned at the north, west, and south sides of the parent grid shown in Figure 4.5. This tidal forcing data was obtained from Tide Model Driver (TMD), a MATLAB package for accessing tidal harmonic constituents for the Earth and Space Research and Oregon State University (ESR/OSU) family of high-latitude tide models, and for making predictions of tide height and currents (Padman, 2005). The extracted tidal amplitudes were obtained for the eight main tidal constituents: K_1, O_1, P_1, Q_1, N_2, M_2, S_2, and K_2.

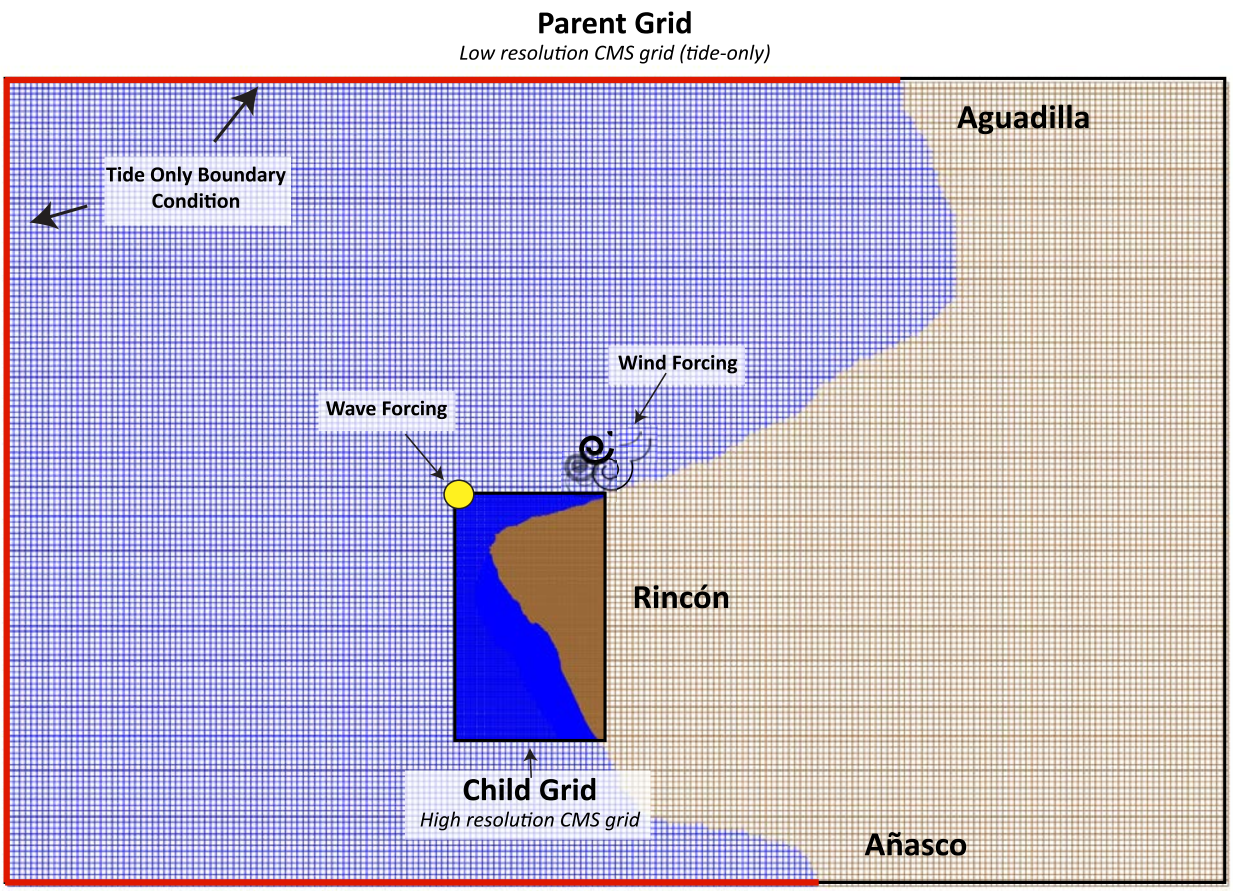

Figure 4.5: Sketch of the nested approach for the CMS-Flow model tidal run. The coarse parent grid was run in tide-only form to provide appropriate tidal forcing to the child grid. Wave and wind forcing was then added to the high-resolution grid.

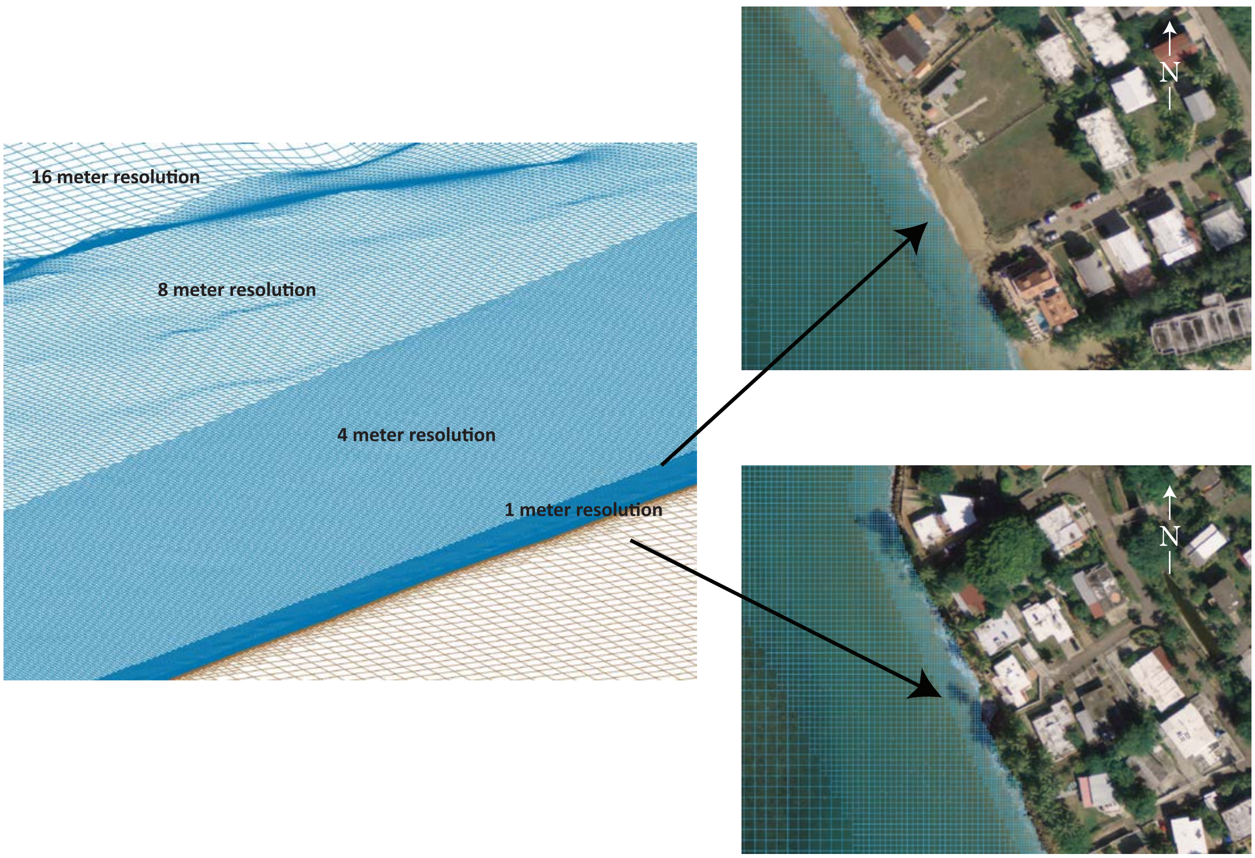

Figure 4.6: Telescoping grid for the CMS-Flow model. The grid has a spatial resolution ranging from 16 meters offshore to a maximum of 1 meter in the nearshore region. This allows the model to resolve very high-resolution circulation features in the nearshore region, while optimizing computational effort by reducing grid cells in areas in which very high spatial resolution is not necessary, such as in the open ocean.

Wind forcing

Wind magnitude and direction data was obtained from two different sources and assigned as temporally variable and spatially constant in the model. For Tropical Storm Isaac, the wind data was obtained from the CariCOOS Rincón anemometer, located in Barrio Puntas (see Figure 1.3 for local reference). Since this anemometer was located on land, the wind speed was adjusted to the 10 meter height using the logarithmic law (Simiu and Scanlan, 1996), which is given by:

$$\upsilon(z) = \frac{\mathrm{u}^*}{\kappa} ln(\frac{z}{z_0}) \tag{4.18}$$

where υ is the mean wind speed profile; u* is the friction velocity; $\kappa = 0.40$ is the von Karman constant; z is the anemometer height above sea mean level (CariCOOS Rincón anememoter height = 15 meters); and z_0 is the surface roughness. With this equation, the wind velocity was adjusted to a height of 10 meters above sea level , which is the most common reference height for near-surface ocean wind measurements. The wind data for Hurricane Sandy was obtained from WRF - Weather Research and Forecasting Model (Mesoscale and Microscale Meteorology Division, 2007), which is used as wind forcing for the CariCOOS Nearshore Wave Model.

4.3.2 CMS-Wave setup

The CMS-Wave model only operates with uniform or non-uniform grids, and does not allow for the use of a telescoping grid. In order to have adequate resolution to account for relevant nearshore physical processes, a non-uniform grid was generated, in which cell shapes vary from squares to rectangles, as shown in Figure 4.7. The grid consists of 1126 x 687 cells with a maximum resolution of 4 meters in the nearshore.

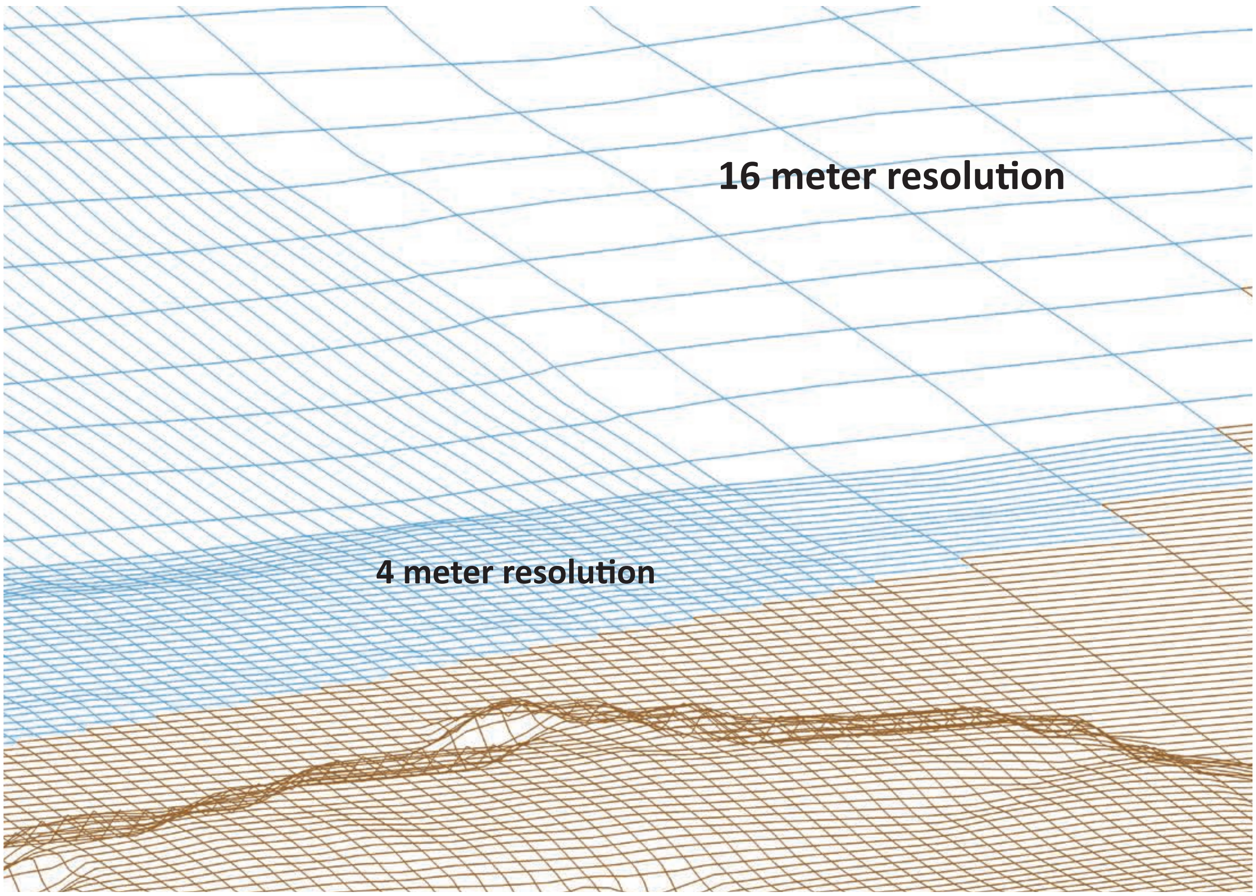

Figure 4.7: Non-uniform grid for the CMS-Wave model. This grid consists of 1126 x 687 cells with a maximum spatial resolution of 4 meters in the nearshore.

Wave forcing

Wave parameters were obtained from the CariCOOS Rincón buoy located northwest of the Rincón Lighthouse, about 1 mile offshore (see Figure 1.3 for local reference). This buoy uses accelerometers to measure horizontal and vertical displacements and pitch-roll sensors to measure wave direction. The obtained directional wave parameters were simulated using a half-plane spectral model, meaning that waves only propagate towards the coast from the seaward boundary. For coupling wave data from CMS-Wave with CMS-Flow parameters a coupling interval of one (1) hour was used.

4.4 Validation of hydrodynamic model

The most important hydrodynamic forces which will affect coastal circulation in the study area are waves and tides. Prior to attempting to simulate morphology change, the hydrodynamic component of the model must be validated. To validate the tidal model, the CMS water elevation model solution (blue line) was compared to the observed data (red line) of a nearshore tide gauge in Mayagüez Bay. Figure 4.8 shows the comparison between the observed data at the NOAA tide station in Mayaguëz, shown in Figure 1.3, and the simulated sea surface elevation. The very large distance between the tide station and the model grid precludes a quantitative comparison. It is evident, however, that the modeled surface elevation is completely in phase with the observed tidal data, which ensures that lateral tidal boundary conditions were correctly applied to the model.

In order to perform a quantitative comparison between observed and predicted current velocities, an RDI Sentinel 300 kHz Acoustic Doppler Current Profiler (ADCP) was deployed in the Tres Palmas Marine Reserve, as shown in Figure 4.9. This location was selected because very strong currents are generated at this site during large swells, making it an ideal location to evaluate the capability of CMS-Flow to reproduce wave-induced current in the nearshore region. An ADCP is an acoustic instrument which is usually deployed as a fixed mooring in the seabed

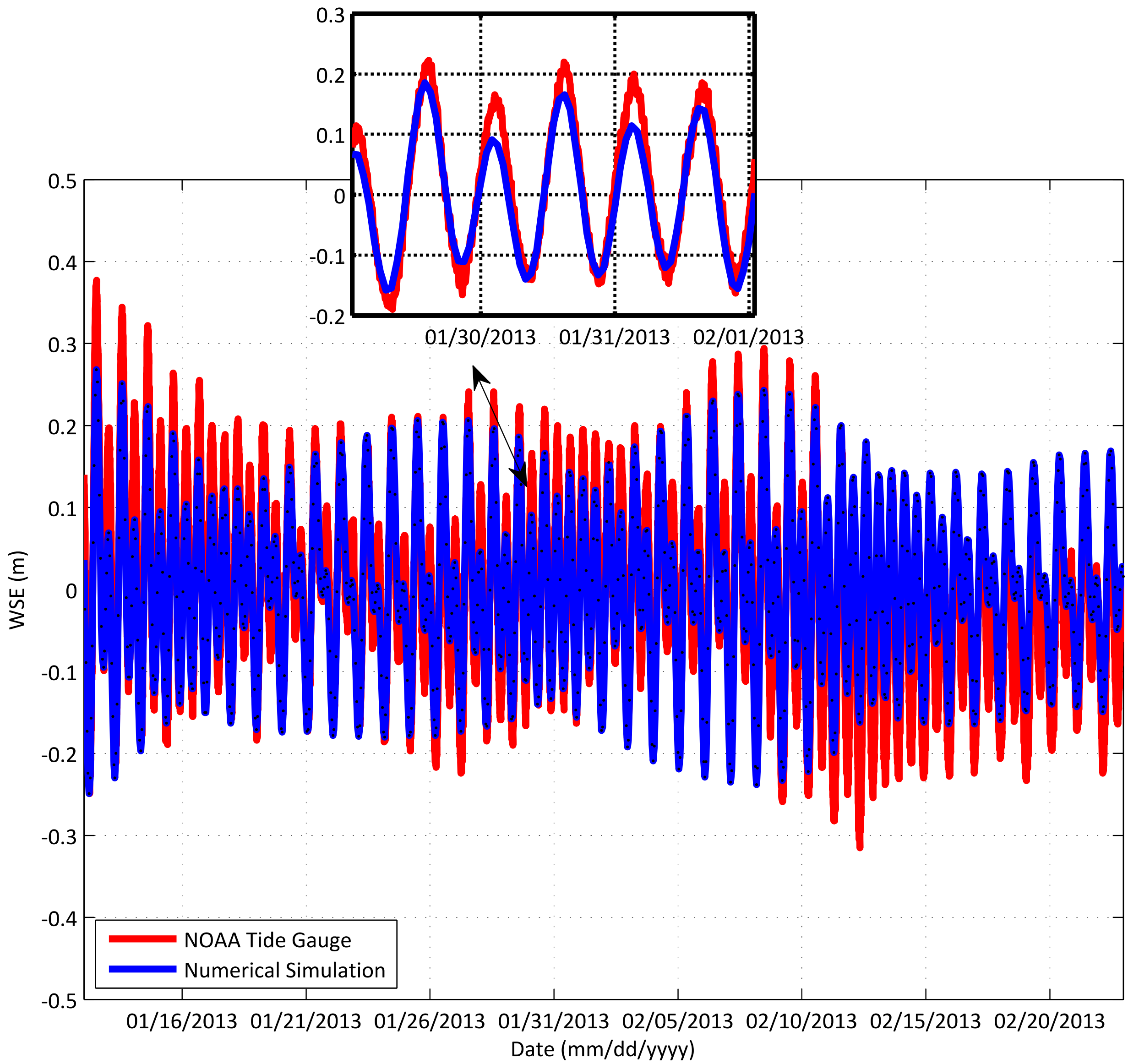

Figure 4.8: Red line: Observed water surface elevation at the Mayagüez NOAA tide station from January to February, 2013. Blue line: simulated sea surface elevation for the CMS Flow grid during the model validation period. The very large distance between the tide station and the model grid precludes a quantitative comparison, however, it is evident that the modeled surface elevation is in phase with the observed tidal data, which ensures that lateral tidal boundary conditions were correctly applied to the model.

Figure 4.9: Location of the Acoustic Doppler Current Profiler (ADCP) deployed in the Tres Palmas Marine Reserve during the model validation period from January 11, 2013 through February 22, 2013.

in order to measure vertical profiles of current velocities. This ADCP was deployed in the seabed off Tres Palmas from January 11, 2013 through February 22, 2013. An ADCP provides measurements of the vertical, depth-dependent profiles of current velocities, however, since CMS is a depth-averaged model, the ADCP data was vertically integrated in order to compare the depth-averaged observed ADCP velocities with the velocities computed by CMS.

Figure 4.10 shows a comparison of the time series of computed (blue line) and observed (red line) depth-averaged north-south velocities, (V_y). Note the similarity in the time series, especially during periods of large waves. In Tres Palmas it is well known that large wave events can generate strong alongshore currents which flow in the southeasterly direction. Results show that the CMS model correctly predicts the timing and magnitude of these alongshore flows. To quantify the model performance in predicting current velocities, which is one of the most important variables in sediment transport modeling, the root mean square error was calculated as:

$$RMSE = \sqrt{\frac{\sum_{i=1}^{N}(P_i - O_i)^2}{M}} \tag{4.19}$$

where P is the CMS predicted depth-averaged current velocity; O is the vertically integrated current velocity observed by the ADCP; and M=1416 is the number of observation-prediction pairs. Figure 4.11 shows a scatter plot of observed vs. predicted current velocities. An error value of the RMSE=0.0836 m s^{-1} was found, as well as a correlation coefficient of R^2 = 0.81. Note that the model performs best when current velocities are large and the circulation is dominated by wave forcing. This validation run shows that the model provides reasonable estimates of wave-driven current velocities, making it possible to better understand the hydrodynamic conditions that caused the morphological changes generated by Tropical Storm Isaac and Hurricane Sandy.

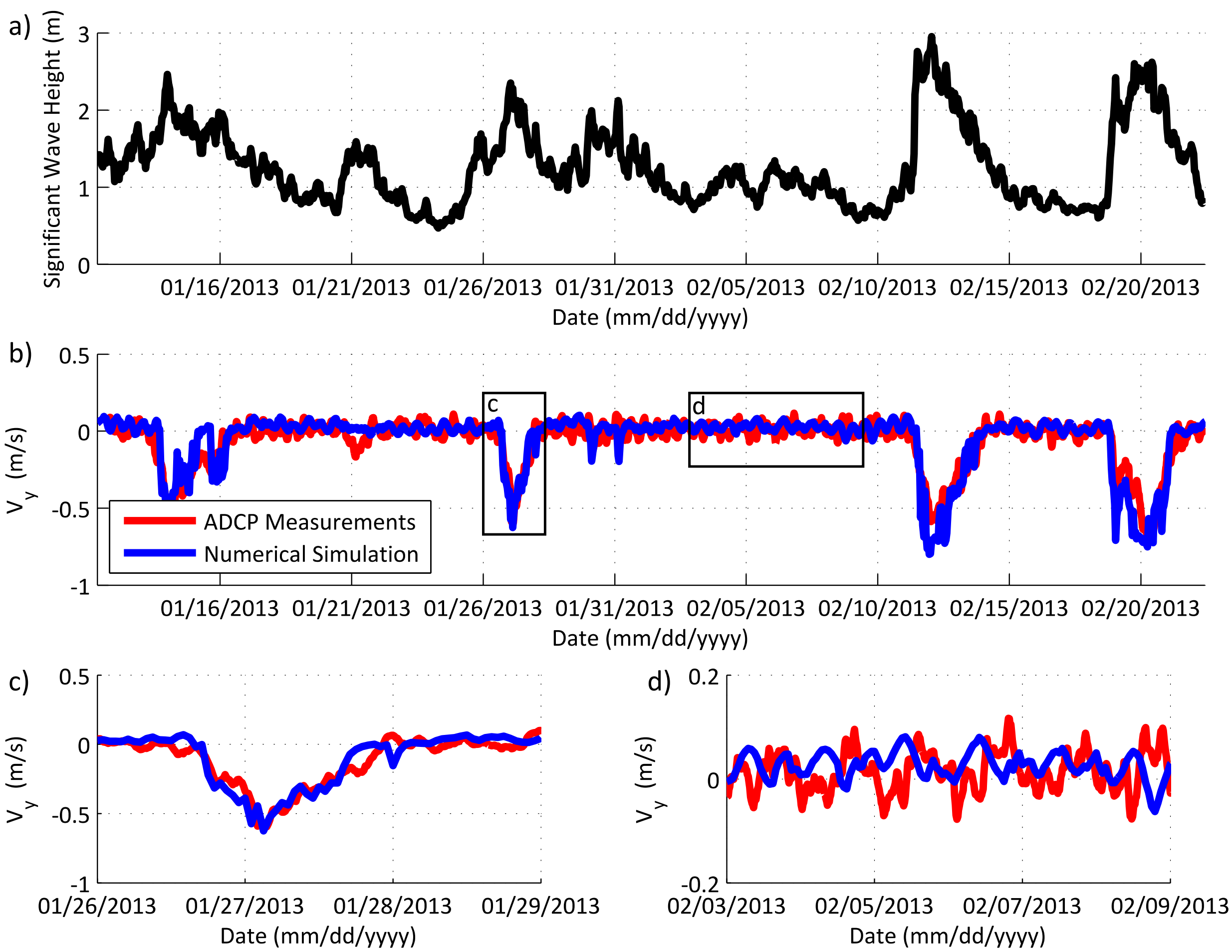

Figure 4.10: Panel (a) shows the wave height measured at the CariCOOS Rincón wave buoy during the model validation period between January 11, 2013 through February 22, 2013, and (b) shows the north-south velocity (V_y) comparison between ADCP measurements and the numerical solution. Panels (c) and (d) are a zoom of the model-data comparison for a significant wave-driven circulation event and for a normal tide-driven flow, respectively.

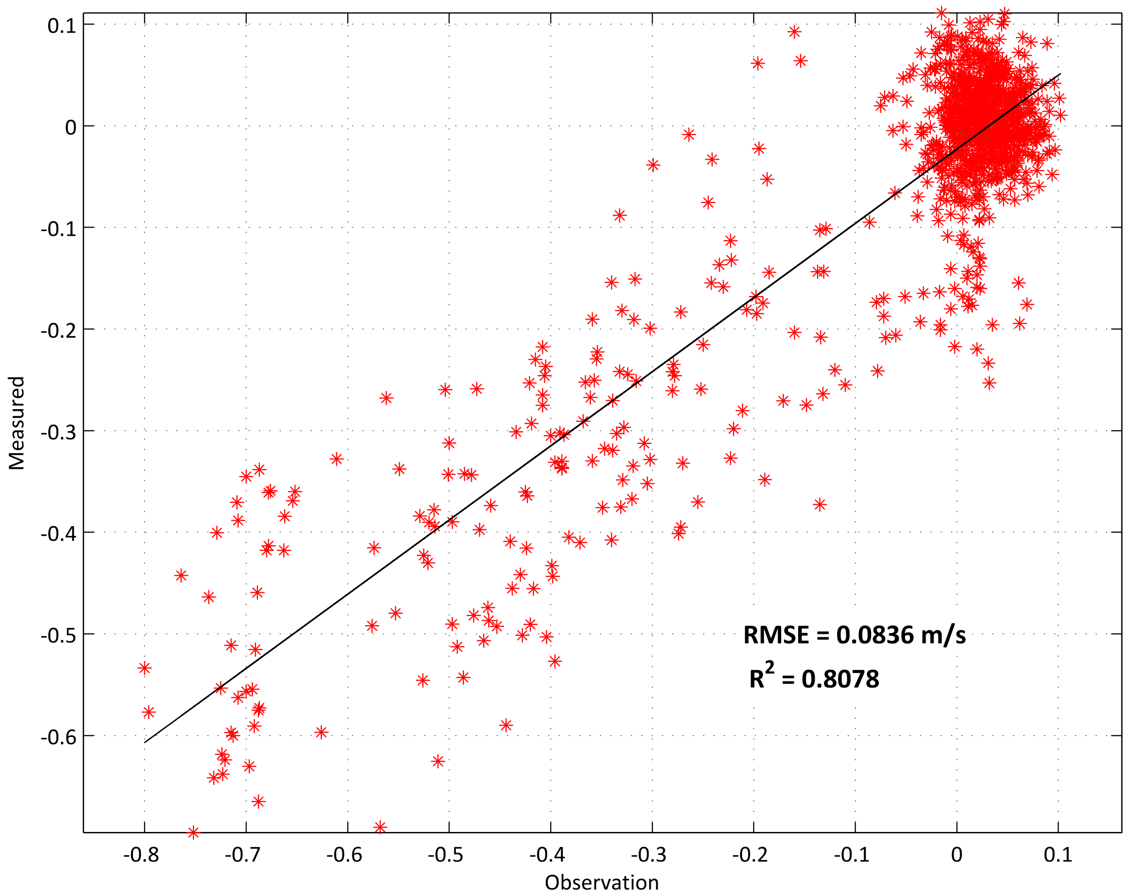

Figure 4.11: Scatter plot of observed versus simulated north-south (V_y) current velocities for the model validation period.

4.5 Model results

Model simulations for Tropical Storm Isaac and Hurricane Sandy were conducted in an attempt to reproduce the morphology change patterns observed using the bathymetric surveying system described in the preceding chapter. The next two subsections focus on the analysis of the computed storm-induced circulation and sediment transport for each storm, and provide a qualitative comparison between the computed and observed erosion and accretion patterns.

4.5.1 Computed storm-induced circulation and morphological response due to Tropical Storm Isaac

The effects of the waves generated by Tropical Storm Isaac were felt in Rincón from August 24-25, 2012. At its peak, this storm generated waves with a significant wave height of 1.8 meters and a peak period of 9 seconds, as registered by the CariCOOS wave buoy. The westward trajectory of the storm and the southwesterly direction generated a somewhat rare sea state for Rincón's coast, resulting in drastic coastal erosion and sediment transport. Figure 4.12 shows the significant wave height (color contours) and wave direction (arrows) at the peak of the storm on August 25, 2012. This figure shows the gradual dissipation of waves from deep water to shallow water, with most of the wave breaking and resulting energy dissipation occurring near the Bajo Blanco sandbar (see Figure 1.3 for local reference). Figure 4.13 shows the current patterns for the same instance as Figure 4.12. Currents within the surf zone vary between 0.01 m s^{-1} up to 0.60 m s^{-1}. The peak current velocities (0.80 m s^{-1}) are observed closest to shore, where the largest gradients in wave energy occur, as well as in the vicinity of the Rincón marina. The vector field also indicates the presence of coherent vortex motions within the surf zone.

Figure 4.14 shows a plot of the computed suspended sediment concentration (colored contours, in kg m^{-3}) and the wave-induced currents (black arrows) for the same instance as Figures 4.12 and 4.13. The largest sediment concentration is observed in the nearshore region, with values ranging from 0.5 kg m^{-3} to 1.4 kg m^{-3}. A large area with high sediment concentration is also observed in the Bajo Blanco area, which confirms the hypothesis by Thieler et al. (2007) that the Bajo Blanco sandbar was a major factor in the sediment budget of Rincón.

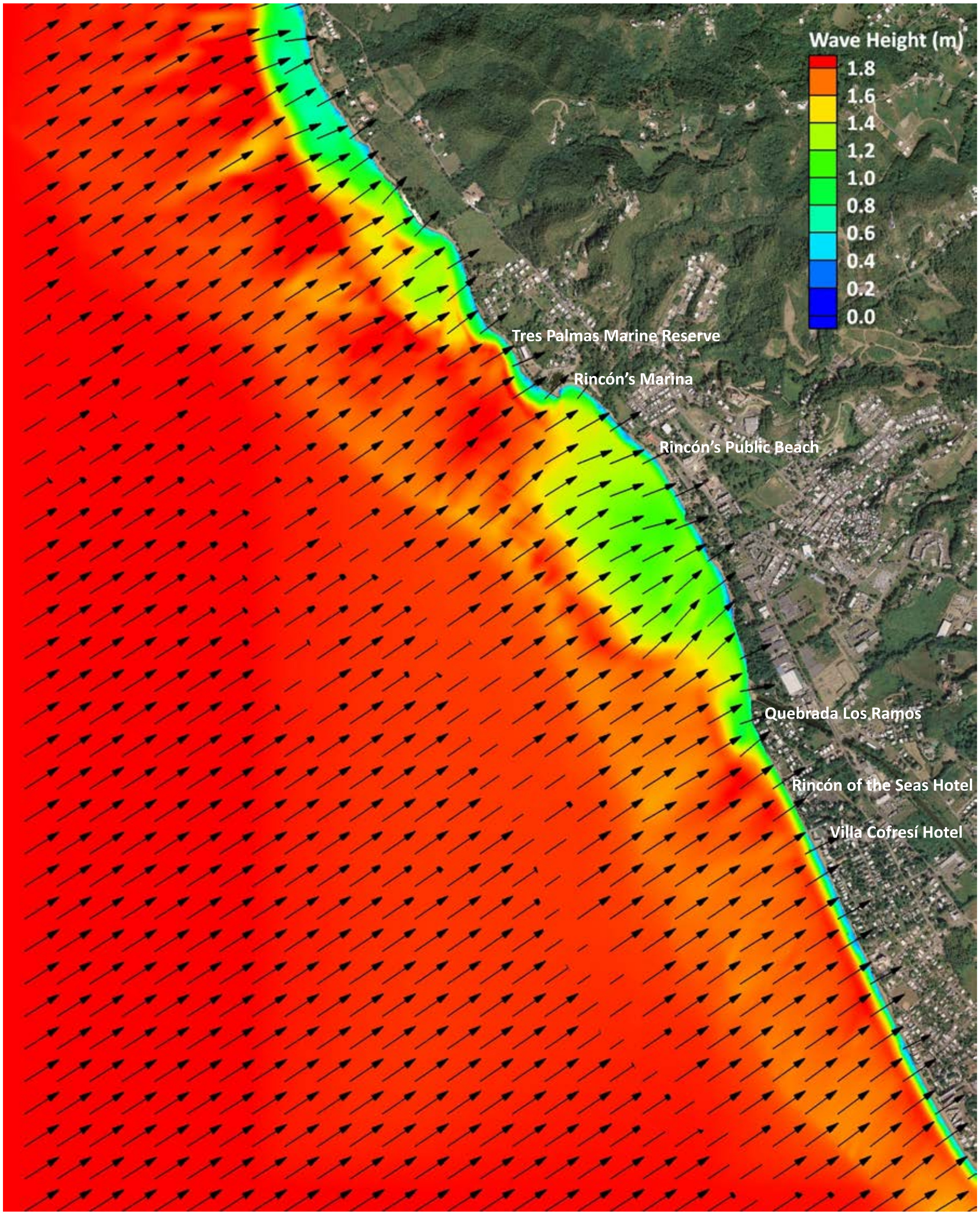

Figure 4.12: Two-dimensional wave height distribution for Tropical Storm Isaac on August 25, 2012. This corresponds to the peak of the southwest wave event, with a significant wave height of 1.8 meters, 9.0 seconds peak period and peak wave direction of 230° as measured at the CariCOOS Rincón wave buoy. Colors denote wave height and the vectors indicate wave direction.

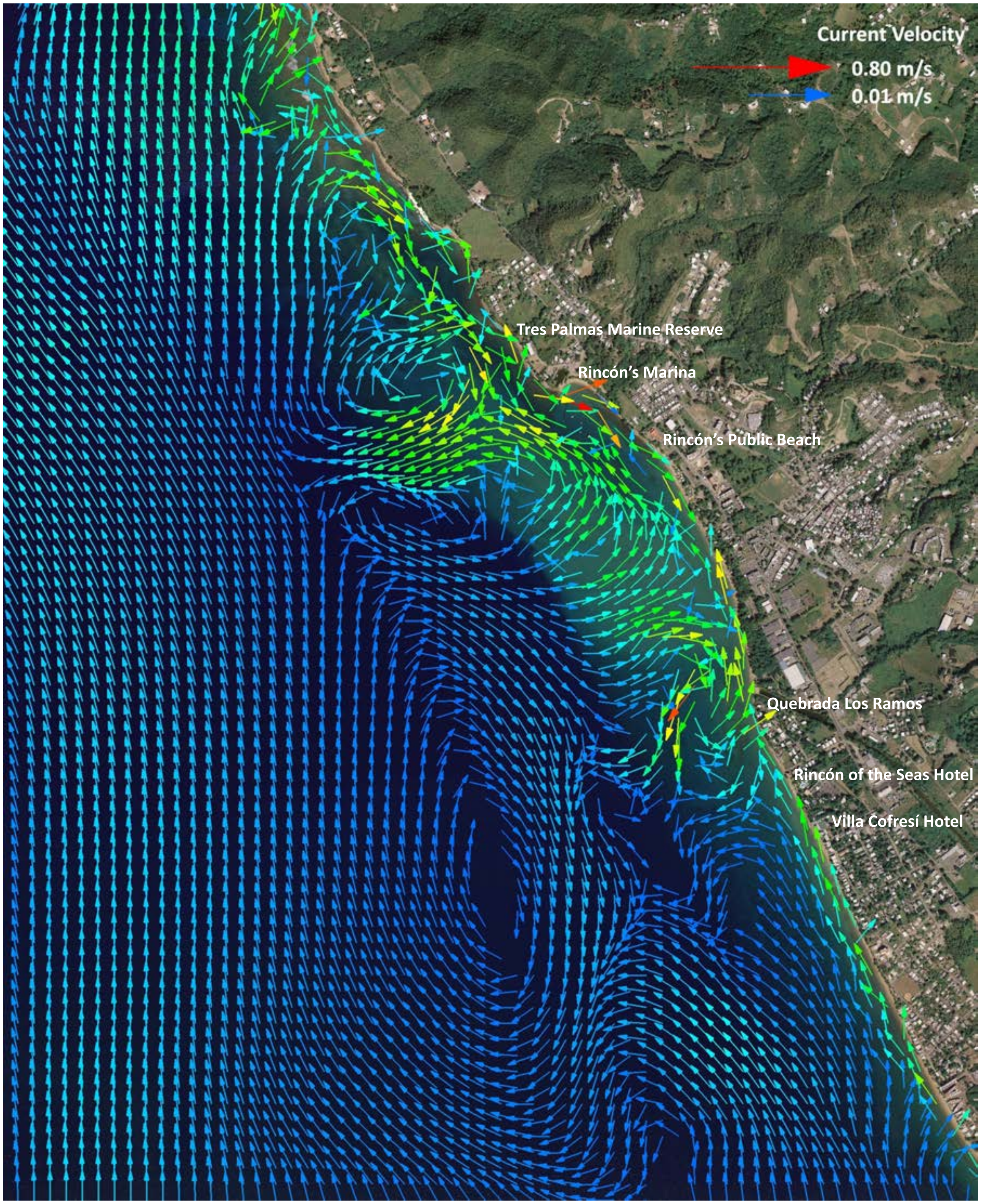

Figure 4.13: Current velocity field for Tropical Storm Isaac on August 25, 2012. This corresponds to the peak of the southwest wave event, with a significant wave height of 1.8 meters, 9.0 seconds peak period and peak wave direction of 230° as measured at the CariCOOS Rincón wave buoy. The color scheme depicts the current velocity and the vectors indicate direction. The current velocity varies from 0.01 m s^{-1} to 0.80 m s^{-1}.

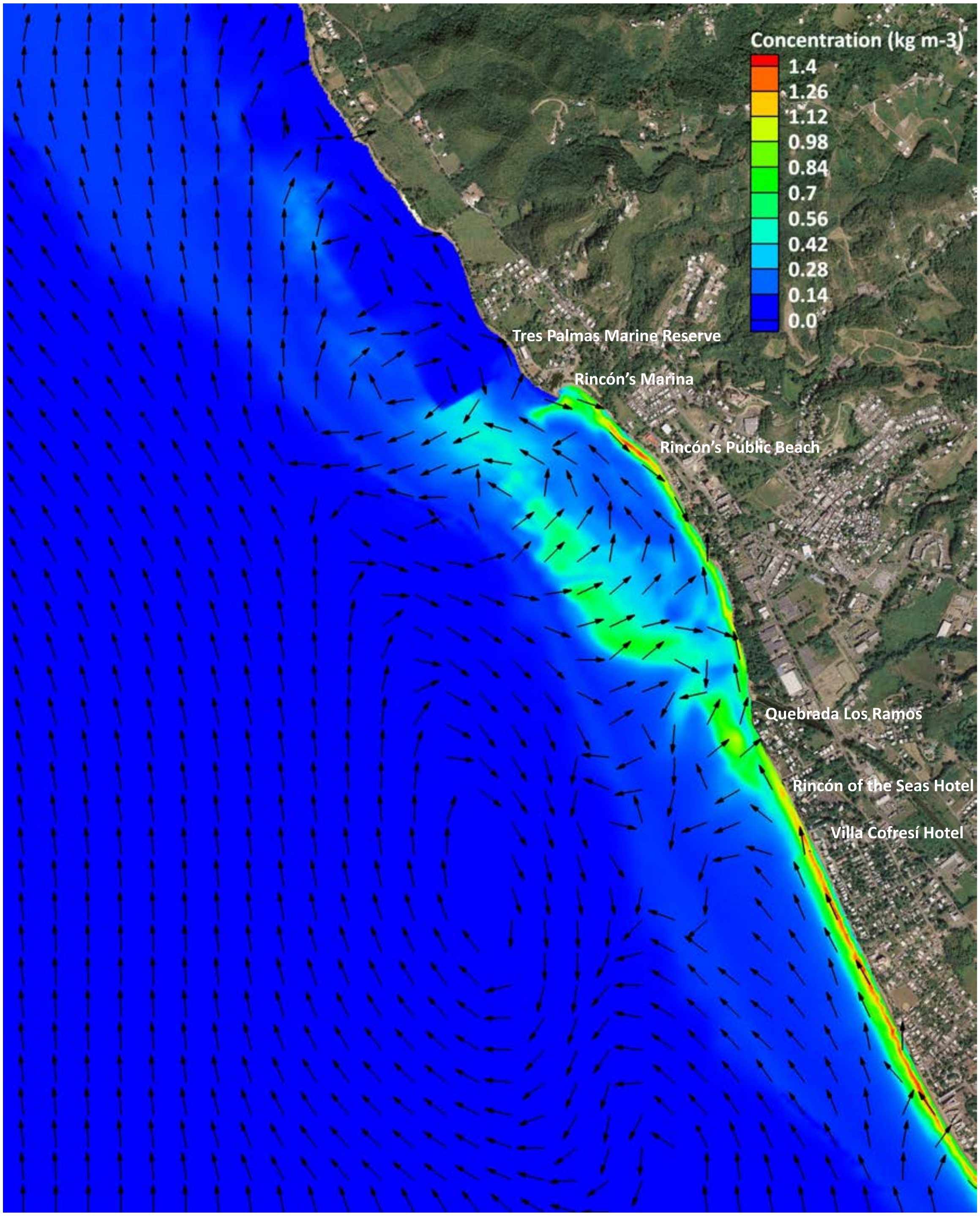

Figure 4.14: Bed and suspended sediment concentration for Tropical Storm Isaac on August 25, 2012. This corresponds to the peak of the southwest wave event, with a significant wave height of 1.8 meters, 9.0 seconds peak period and peak wave direction of 230° as measured at the CariCOOS Rincón wave buoy. The color scheme depicts the sediment concentration and the vectors indicate direction. The suspended sediment concentration varies from 0.50 kg m^{-3} to 1.40 kg m^{-3}.

Figure 4.15 shows the computed nearshore circulation patterns for the area in which the bathymetric surveys discussed in the preceding chapter were conducted, while Figure 4.16 shows a plot of the computed suspended sediment concentration and wave-induced currents during the peak of Tropical Storm Isaac. Maximum velocities are observed in a vortex-type circulation feature offshore of Quebrada Los Ramos (as seen in Figure 4.13), reaching velocities up to 0.80 m s^{-1}. These strong wave-induced currents generate an area with a large concentration of suspended sediment (0.7 to 1.4 kg m^{-3}).

The instantaneous snapshots shown in Figures 4.12 through 4.16 are useful to visualize the flow topology and the dominant circulation patterns, however, it is difficult to infer the resulting changes in the seabed from a visual inspection of these figures. CMS, however, can compute the evolution of the seabed as a function of the hydrodynamic forcing. Figure 4.17 shows the computed morphology change for the study site. From this figure, three major areas of morphology change are observed:

1. The first notable region is the Bajo Blanco sandbar, where the model suggests notable sediment deposition.

2. The second area of interest is, as expected, the nearshore zone, where alternating bands of erosion and accretion are evident along most of the coastline extending from the Rincón public beach to the area south of Villa Cofresí.

3. The third area is a localized pattern of erosion and accretion off the Quebrada Los Ramos area, where the coastline abruptly changes orientation. This is the same area in which the intense vortex circulation was observed in Figure 4.15.

The main question is whether these computed patterns and values of morphology change are reasonable at all, and for this reason the morphology change computed by CMS are compared with the morphology change observed from the jetski-based bathymetric surveys described in the

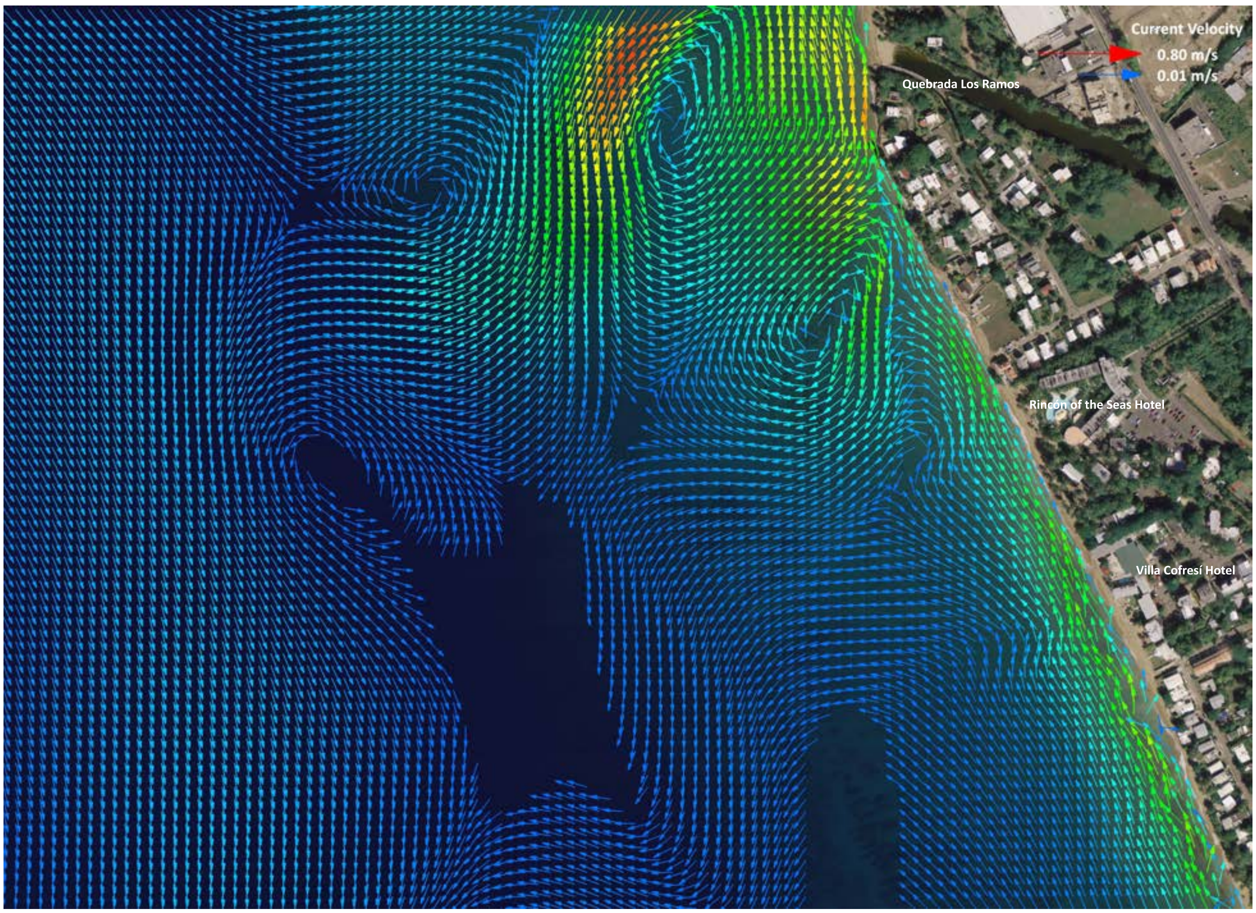

Figure 4.15: Zoom of the computed current velocities for Tropical Storm Isaac at the study site during the peak of the storm. The color scheme depicts the current velocity and the vectors indicate current direction. The current velocity varies from 0.01 m s^{-1} to 0.80 m s^{-1}.

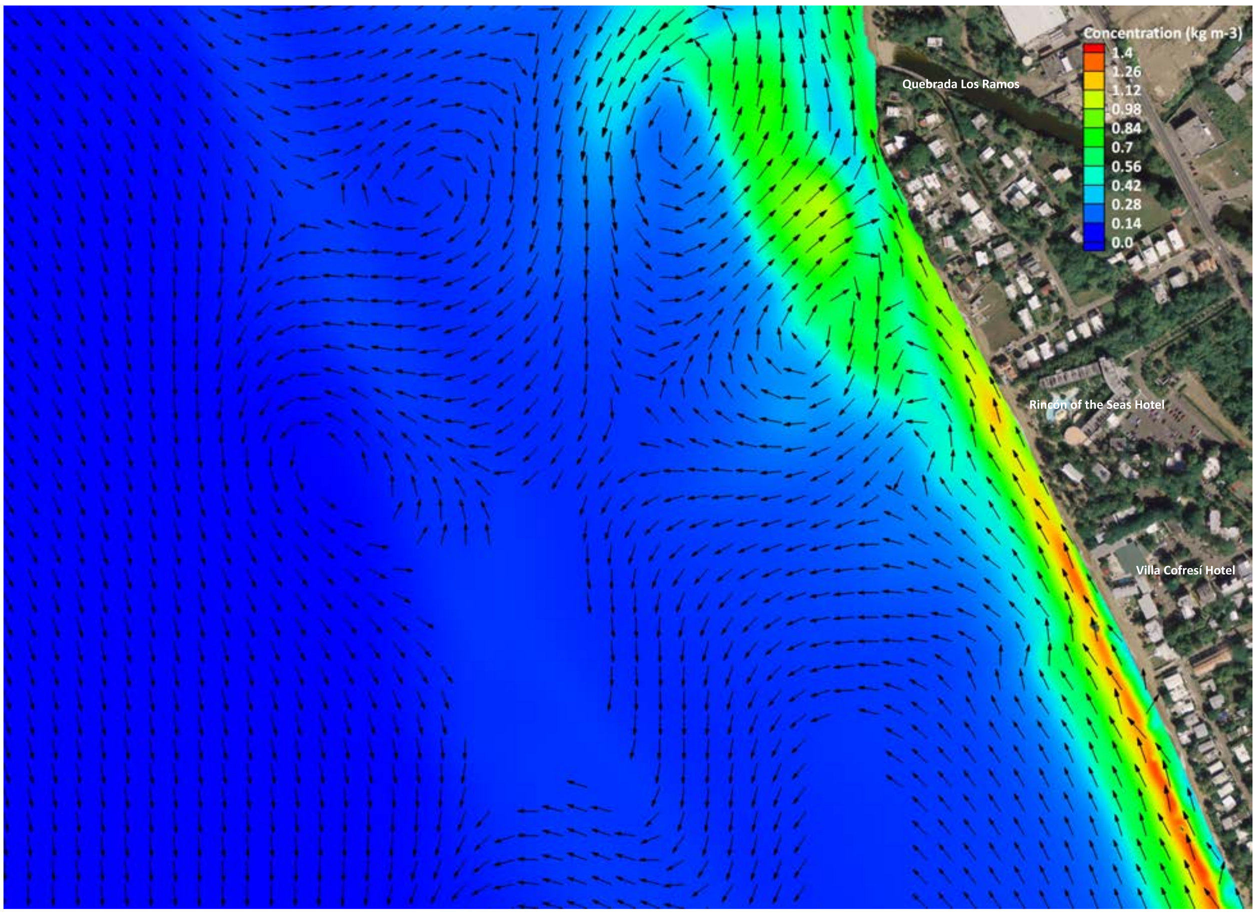

Figure 4.16: Zoom of the computed suspended sediment concentration for Tropical Storm Isaac at the study site during the peak of the storm. The color scheme depicts the sediment concentration and the vectors indicate current direction. The suspended sediment concentration varies from 0.50 kg m^{-3} to 1.40 kg m^{-3}.

preceding chapter. Figure 4.18 shows a qualitative comparison between the computed and observed morphology change. By visually comparing the two figures, it is evident that the simulated morphology change (right panel) shows several similarities to the changes measured with the surveying system (left panel). Most importantly, the computed erosion and accretion values agree very well with the maximum and minimum observed values of seabed change. This suggests that the model is correctly predicting the bulk of the sediment transport and the magnitude of morphology change occurring in the region. Both the model and the observations show elongated bands of erosion and accretion parallel to the shoreline. These areas seem to correlate well with the areas of maximum current velocities and the vortex structures shown in the snapshots of Figures 4.13 through 4.16.

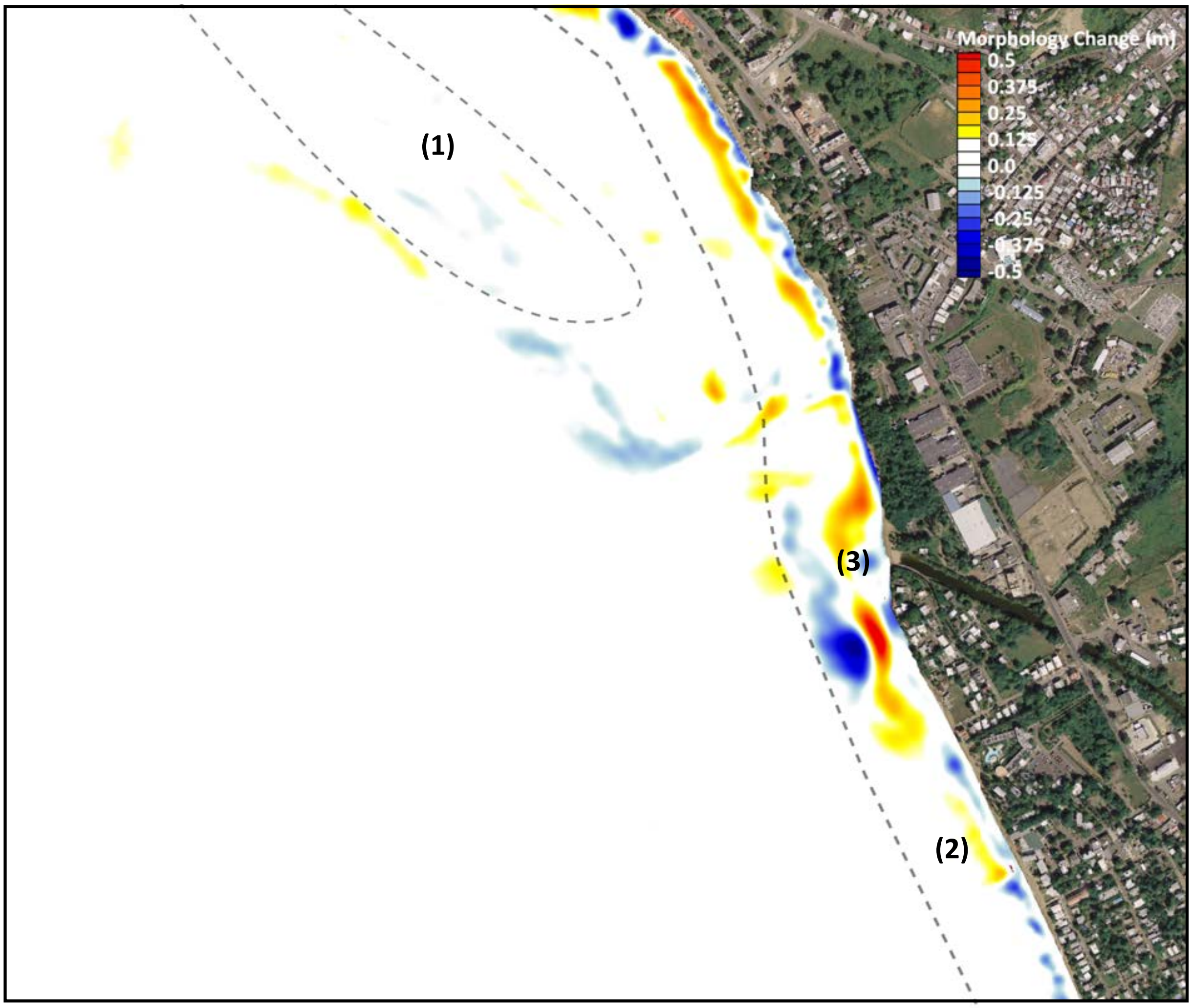

Figure 4.17: Computed morphology change for Tropical Storm Isaac on September 20, 2012. The color scheme shows the morphology change where red (+) indicates accretion and blue (−) indicates erosion. Note the presence of three areas with significant morphology change: (1) the Bajo Blanco area, (2) the nearshore region and (3) Quebrada Los Ramos.

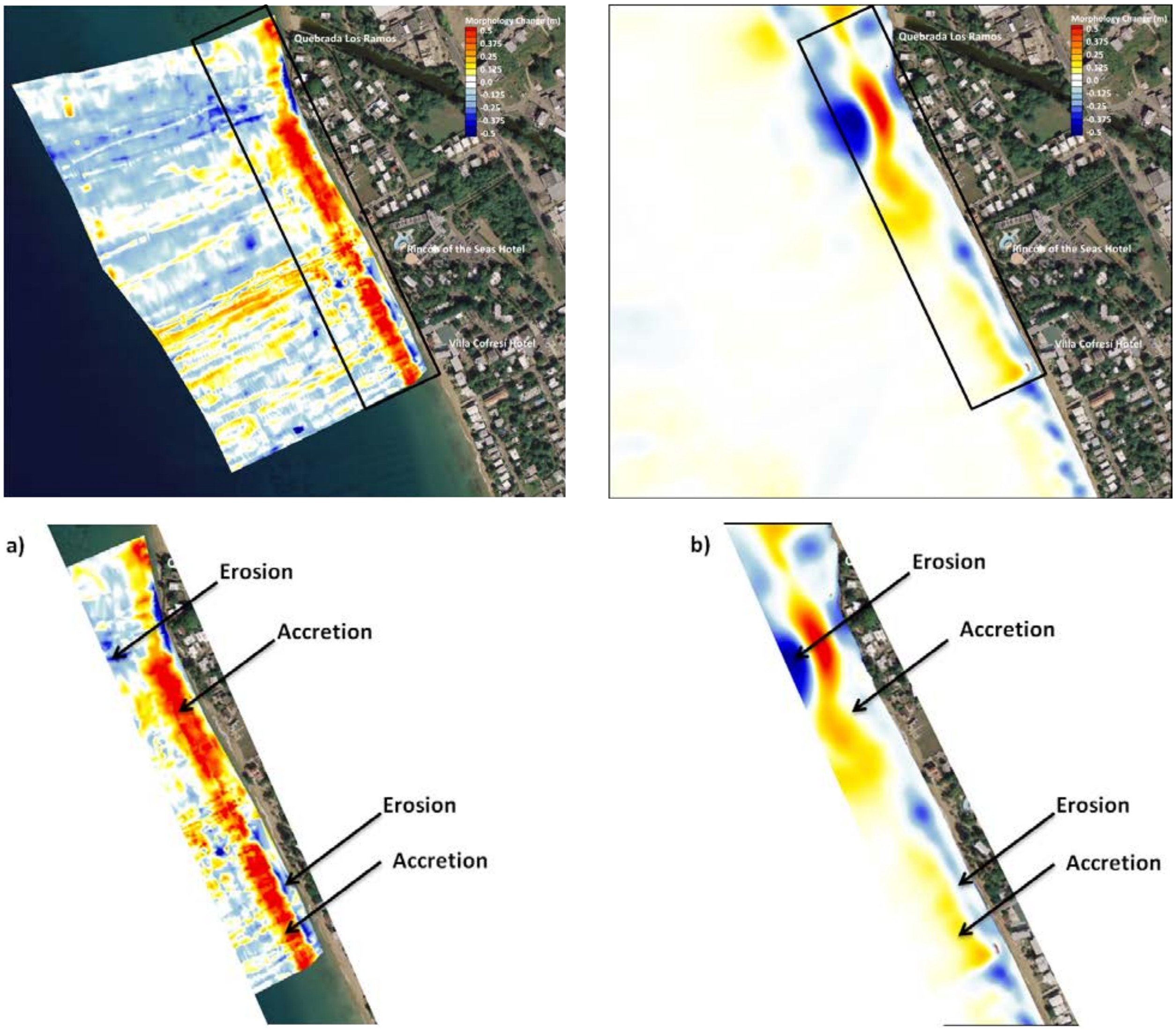

Figure 4.18: Comparison between modeled and observed morphology change for Tropical Storm Isaac: a) measured morphology change and b) simulated morphology change. The color scheme shows the morphology change where red (+) indicates accretion and blue (−) indicates erosion.

4.5.2 Computed storm-induced circulation and morphological response due to Hurricane Sandy

As explained in the preceding chapter, Hurricane Sandy was an unusual storm which generated two distinct extreme wave events within a short period of time. On October 25, Sandy generated waves from a southwesterly direction with a significant wave height of 1.7 meters and a peak period of 11 seconds. As the storm continued its trajectory towards the U.S. East Coast, Sandy intensified and sent highly energetic waves towards the north and west coast of Puerto Rico. This secondary peak generated an event with a maximum significant wave height of 3.6 meters and a peak period of 12.5 seconds. This contrast in swell direction was a very rare event for Rincón, and a detailed numerical simulation was conducted to examine the effects of this large variability in wave direction on the hydrodynamics and sediment transport patterns of the area.

Figure 4.19 shows the two-dimensional distribution of wave height and wave direction for the peak of the southwest wave event on October 26, 2012. Figure 4.20 shows the current patterns for the same instance as Figure 4.19. The peak current velocities are approximately 0.8 m s^{-1}, and the general pattern is that of a southward flow near Tres Palmas with a northward alongshore flow near the Rincón public beach. Figure 4.21, shows a plot of the computed suspended sediment concentration (colored contours, in kg m^{-3}) and the wave-induced currents (black arrows) for the same instance as Figures 4.19 and 4.20. The largest sediment concentration is observed in the nearshore region, with values ranging from 0.5 kg m^{-3} to 1.4 kg m^{-3}. Figures 4.22 and 4.23 show the wave-induced currents and sediment concentration for a zoom of the area in which the bathymetric surveying was conducted.

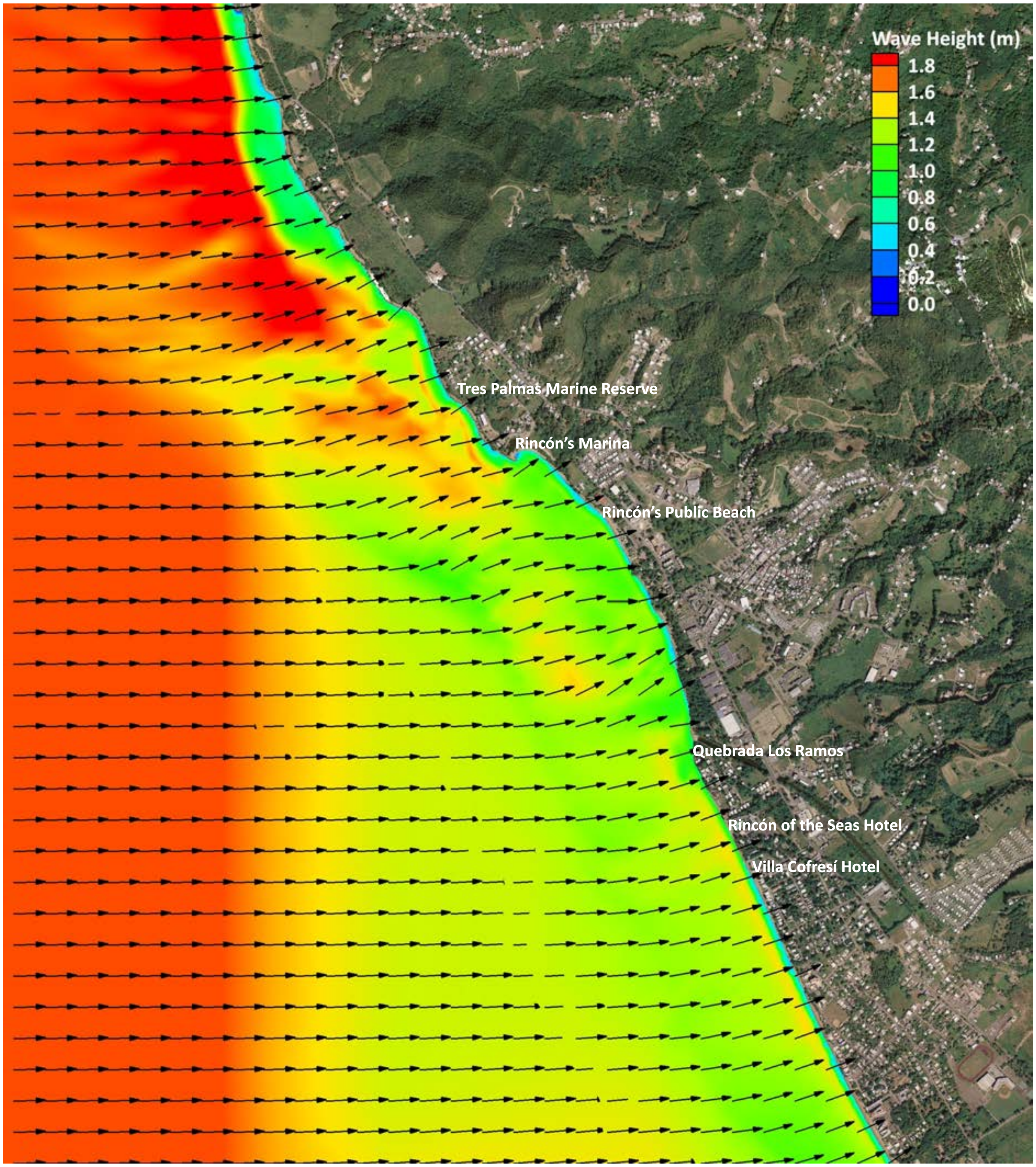

Figure 4.19: Two-dimensional wave height distribution for Hurricane Sandy on October 26, 2012. This corresponds to the peak of the southwest wave event, with a significant wave height of 1.7 meters, peak period of 11.0 seconds and a peak wave direction of 270° as measured at the CariCOOS Rincón wave buoy. Colors denote wave height and the vectors indicate wave direction.

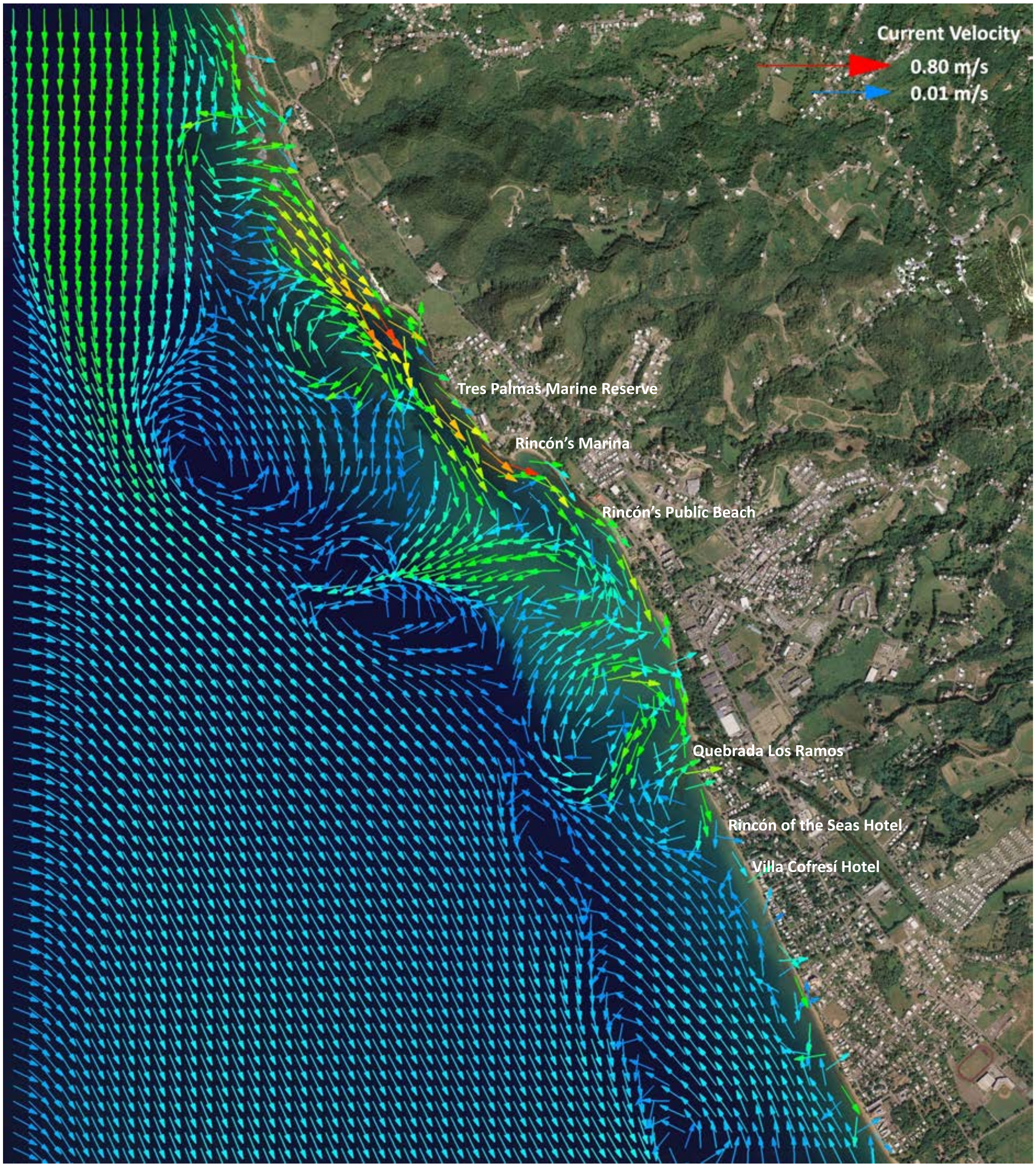

Figure 4.20: Current velocity field for Hurricane Sandy on October 26, 2012. This corresponds to the peak of the southwest wave event, with a significant wave height of 1.7 meters, peak period of 11.0 seconds and a peak wave direction of 270° as measured at the CariCOOS Rincón wave buoy. The current velocity varies from 0.01 m s^{-1} to 0.80 m s^{-1}.

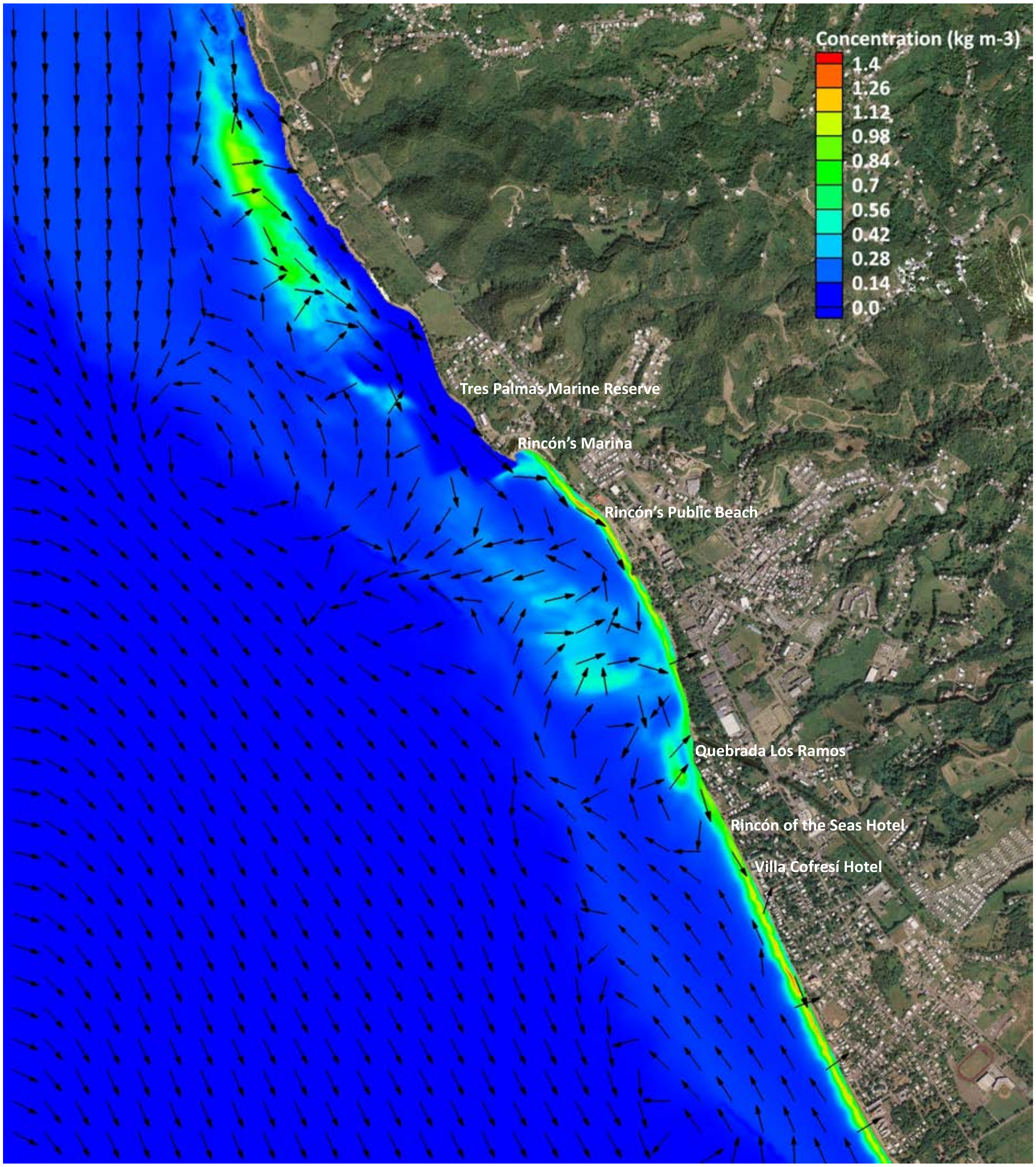

Figure 4.21: Bed and suspended sediment concentration for Hurricane Sandy on October 26, 2012. This corresponds to the peak of the southwest wave event, with a significant wave height of 1.7 meters, peak period of 11.0 seconds and a peak wave direction of 270° as measured at the CariCOOS Rincón wave buoy. The color scheme depicts the sediment concentration and the vectors indicate current direction. The suspended sediment concentration varies from 0.30 kg m^{-3} to 1.40 kg m^{-3}.

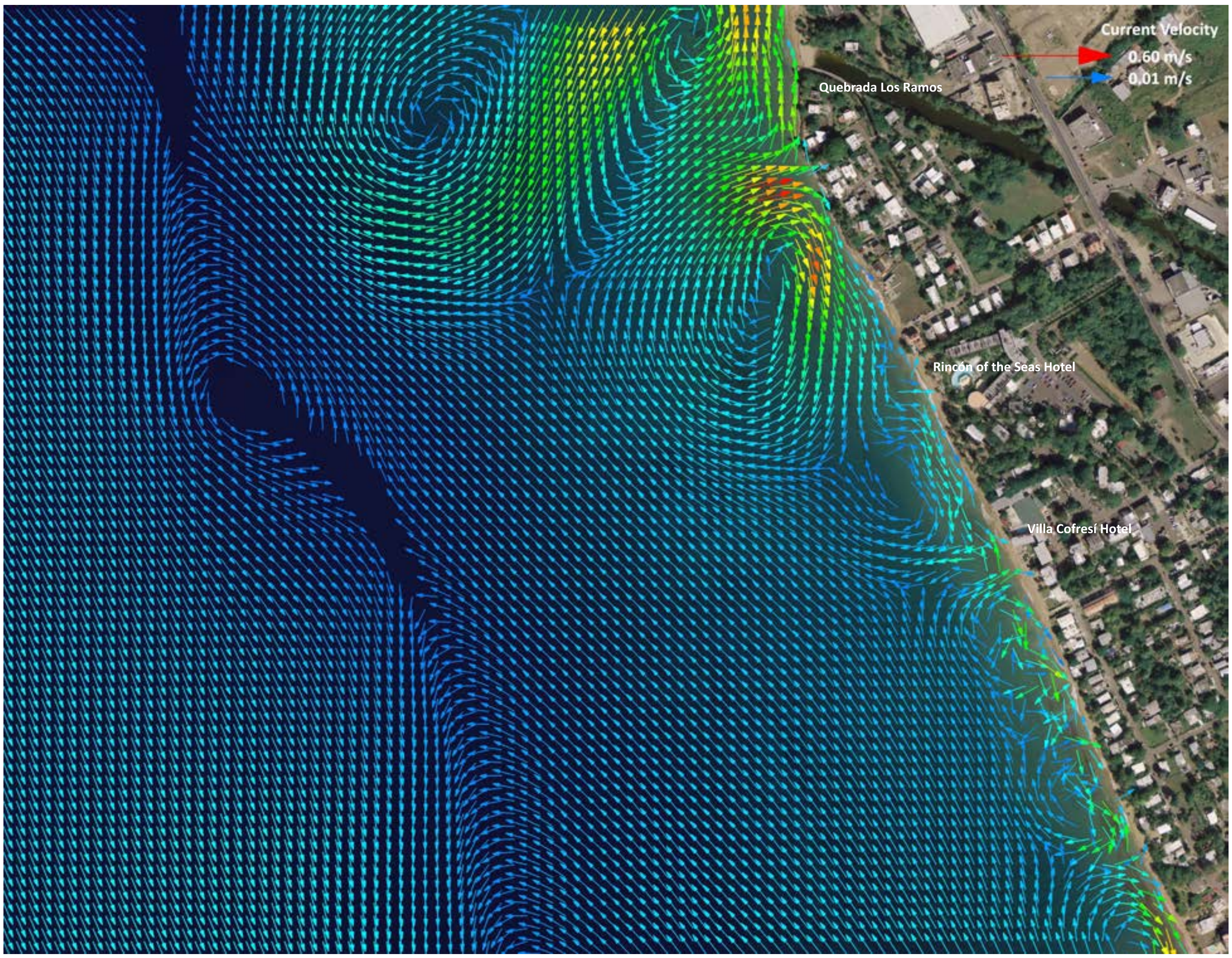

Figure 4.22: Zoom of the computed current velocities for Hurricane Sandy at the study site during the peak of the southwest wave event. The color scheme depicts the current velocity and the vectors indicate current direction. The current velocity varies from 0.01 m s^{-1} to 0.80 m s^{-1}.

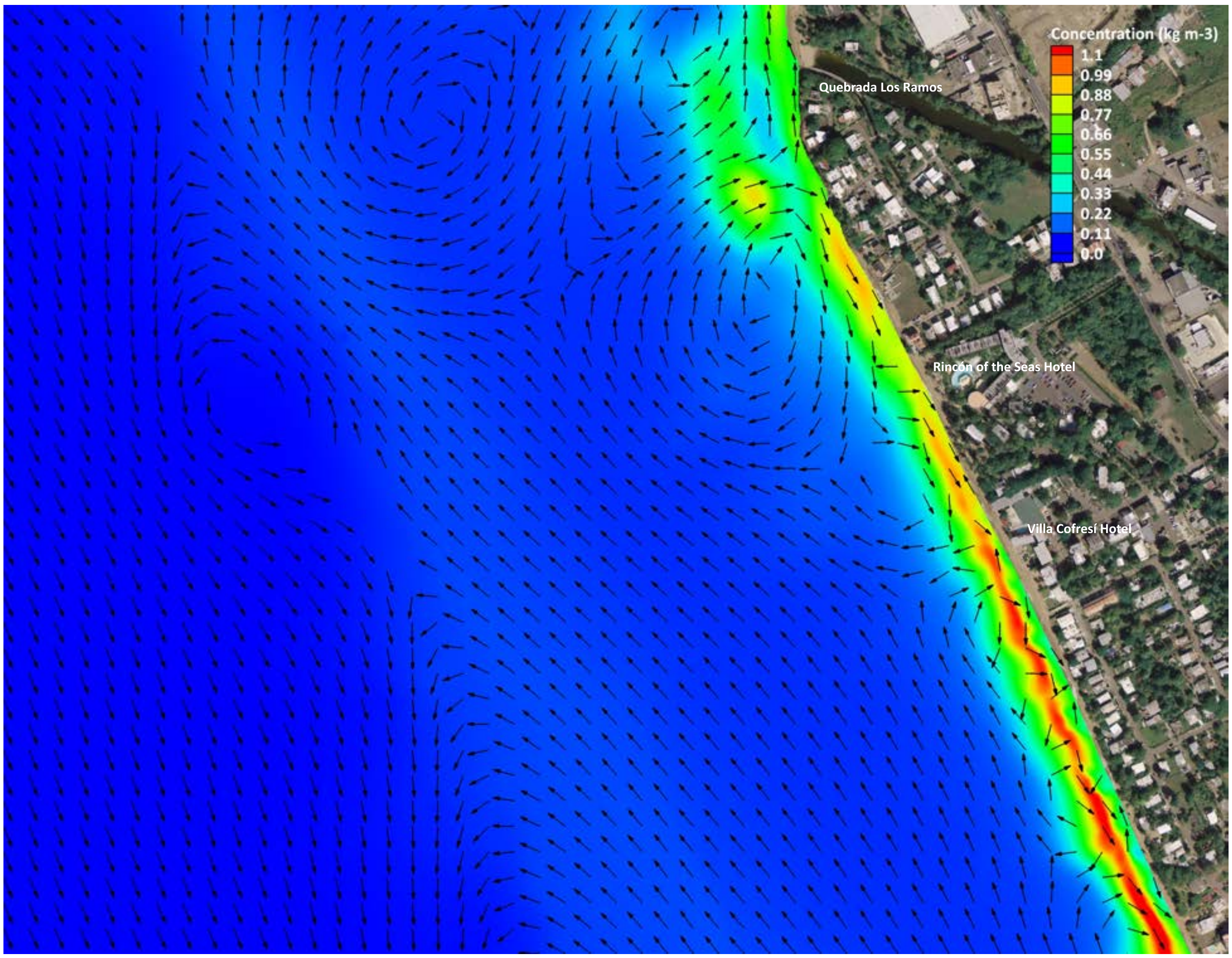

Figure 4.23: Zoom of the computed suspended sediment concentration for Hurricane Sandy at the study site during the peak of the southwest wave event. The color scheme depicts the sediment concentration and the vectors indicate current direction. Large values of suspended sediment concentration varying from 0.50 kg m^{-3} to 1.40 kg m^{-3} concentration can be observed near the shoreline where maximum currents prevail.

As Hurricane Sandy moved towards the U.S. East Coast it generated a strong wave event from a northwesterly direction. Figure 4.24 shows the wave height and direction for the peak of this event on October 30, 2012. Figure 4.25 shows the resulting current patterns for this same instance, with peak current velocities up to 2 m s^{-1} in the vicinity of Tres Palmas. Note that in this case the strong northwest component of this event caused strong alongshore flows with a mean transport towards the southeast.

Figure 4.26 shows the total sediment concentration and wave-induced currents for this instance. In contrast to previous plots, the sediment concentration is largest near Tres Palmas and much smaller than the sediment concentration observed during the southwest events caused by Sandy and Isaac. This is because during swells with a strong north component, the reefs off Tres Palmas dissipate most of the wave energy before it reaches the beaches south of the marina. For this same instance, Figures 4.27 and 4.28 show the wave-induced currents and sediment concentration for a zoom of the area in which the bathymetric surveying was conducted. A moderate alongshore current is evident very close to the coast, with a corresponding region of sediment concentration. This southward alongshore sediment transport is completely opposite to the transport observed for the southwest wave events of both Sandy and Isaac.

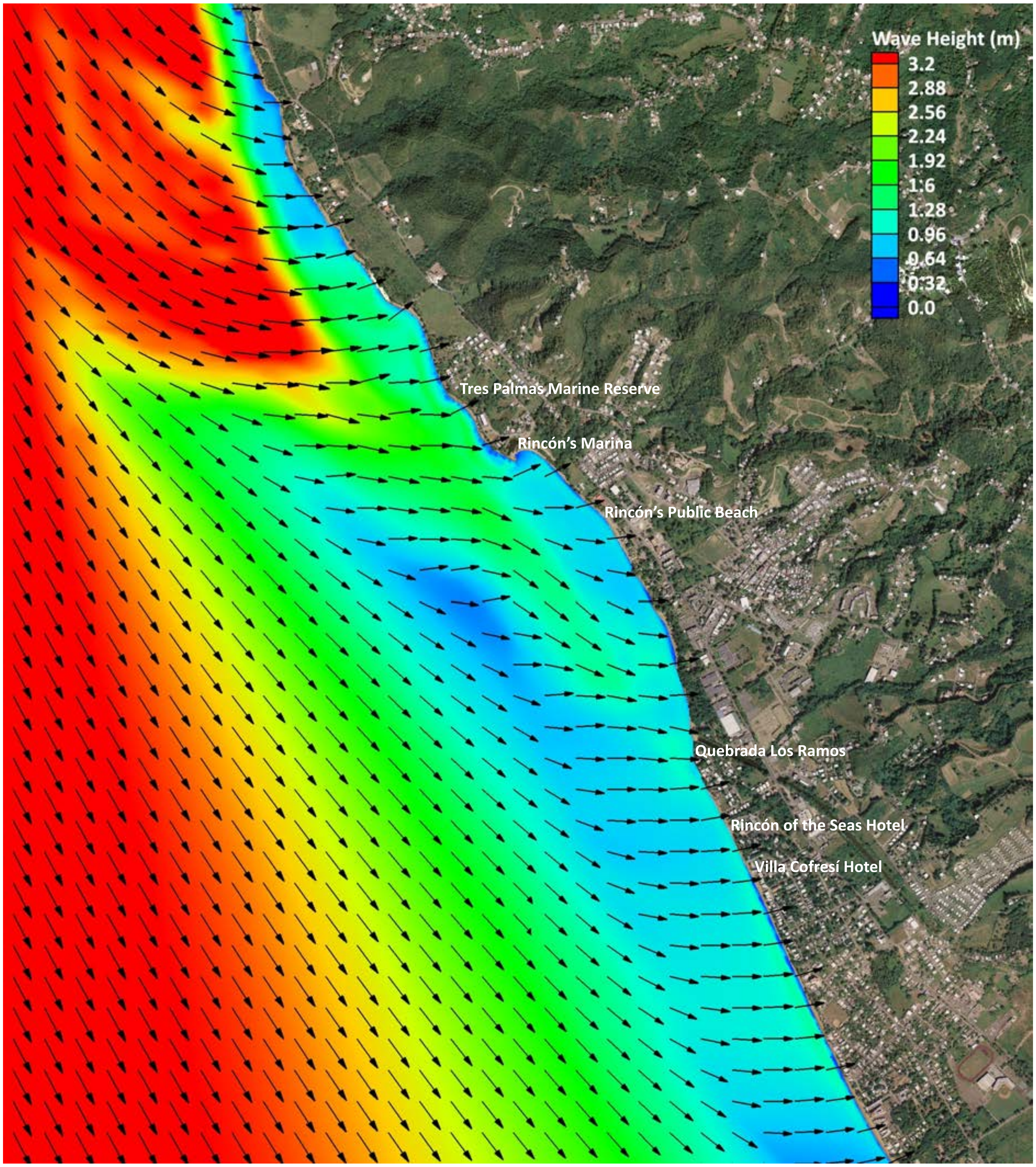

Figure 4.24: Two-dimensional wave height distribution for Hurricane Sandy on October 30, 2012. This corresponds to the peak of the northwest wave event, with a significant wave height of 3.6 meters, 12.5 seconds peak period and a peak wave direction of 334° as measured at the CariCOOS Rincón wave buoy. Colors denote wave height and the vectors indicate wave direction.

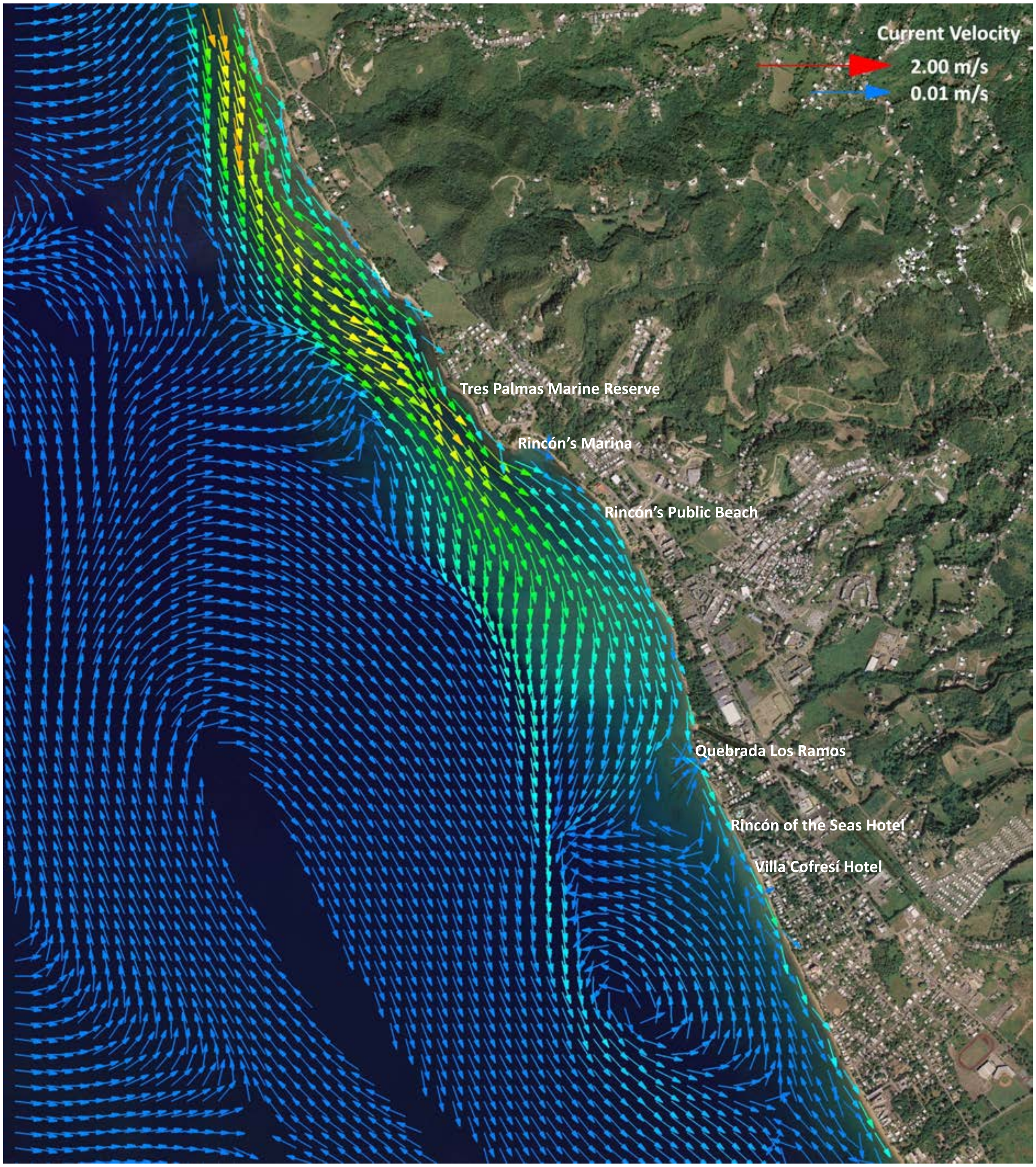

Figure 4.25: Current velocity field for Hurricane Sandy on October 30, 2012. This corresponds to the peak of the northwest wave event, with a significant wave height of 3.6 meters, 12.5 seconds peak period and a peak wave direction of 334° as measured at the CariCOOS Rincón wave buoy. The current velocity varies from 0.01 m s^{-1} to 2.0 m s^{-1}.

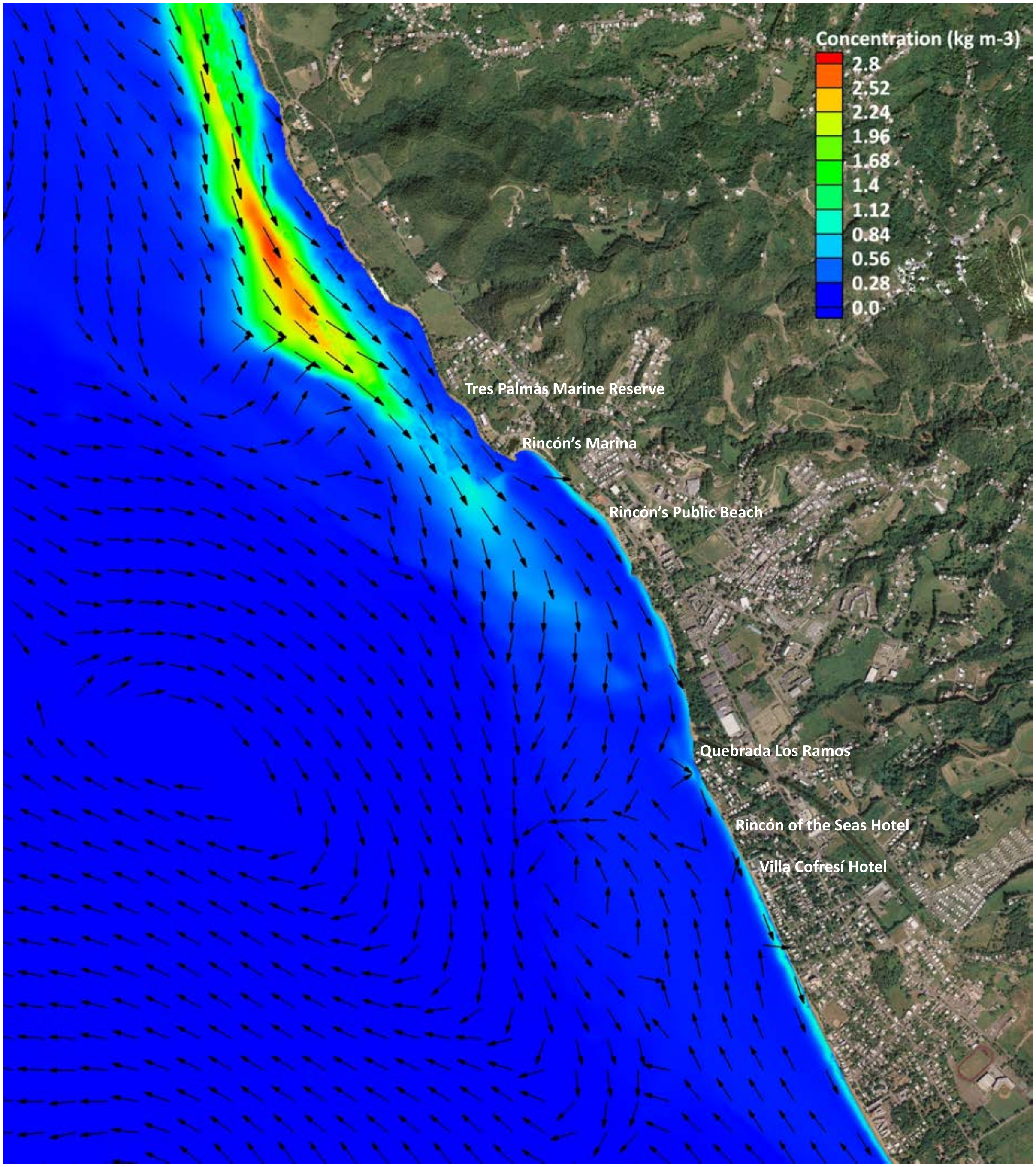

Figure 4.26: Total sediment concentration for Hurricane Sandy on October 30, 2012. This corresponds to the peak of the northwest wave event, with a significant wave height of 3.6 meters, 12.5 seconds peak period and a peak wave direction of 334° as measured at the CariCOOS Rincón wave buoy. The color scheme depicts the sediment concentration and the vectors indicate current direction. The total sediment concentration varies from 0.50 kg m^{-3} to 2.80 kg m^{-3}.

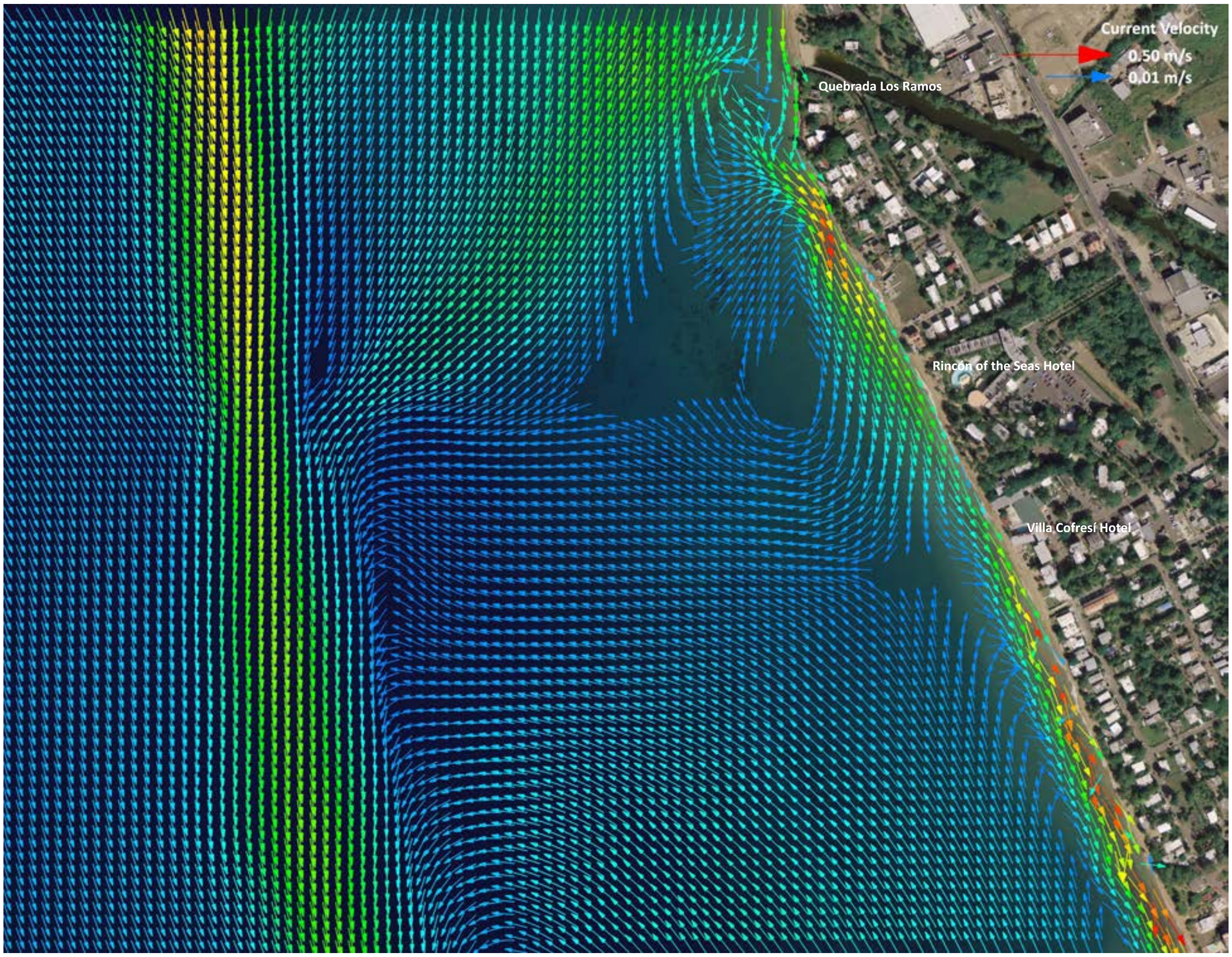

Figure 4.27: Zoom of the bathymetric surveying study area showing wave-induced currents for Hurricane Sandy on October 30, 2012. This corresponds to the peak of the northwest wave event, with a significant wave height of 3.6 meters, 12.5 seconds peak period and a peak wave direction of 334° as measured at the CariCOOS Rincón wave buoy.

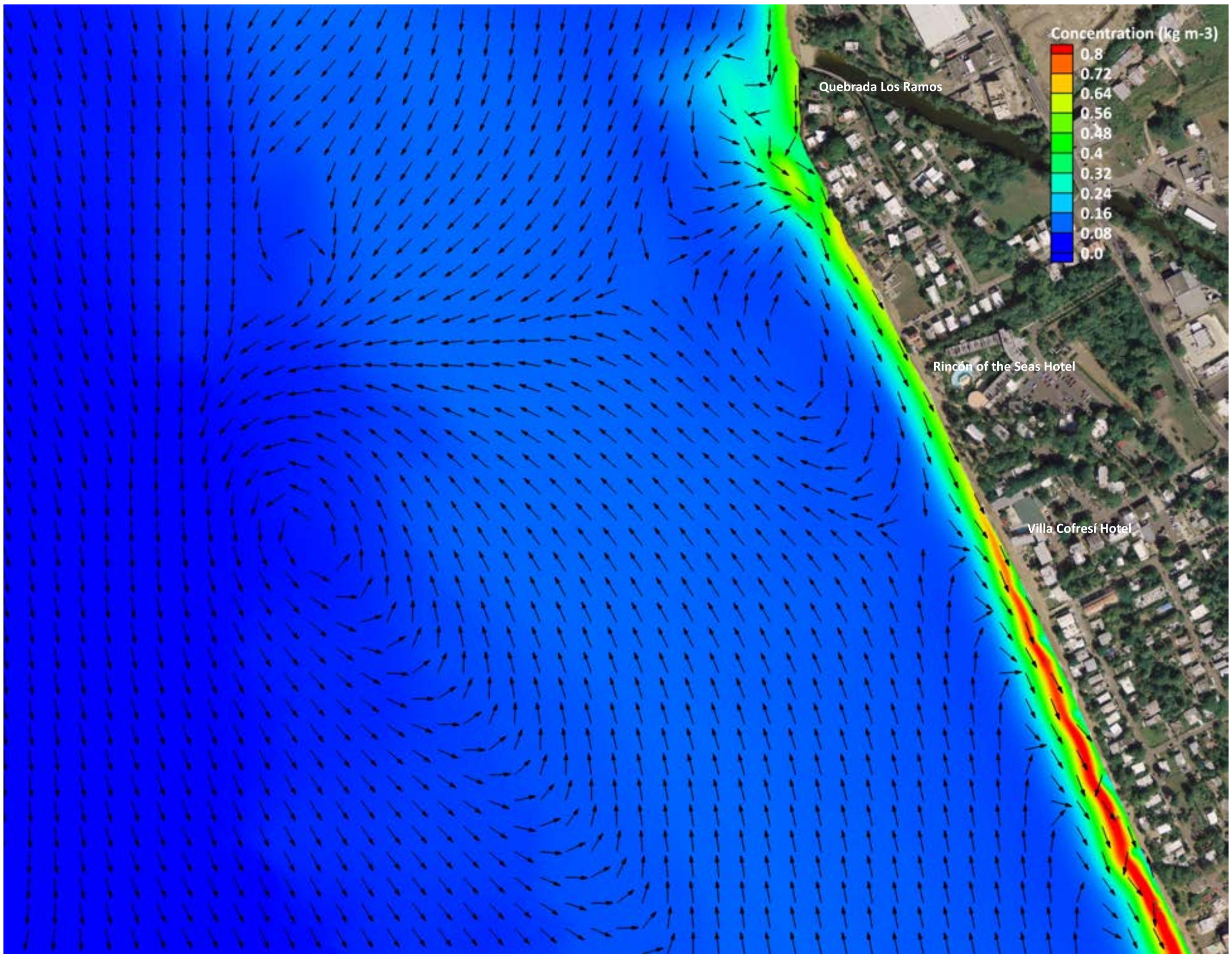

Figure 4.28: Zoom of the bathymetic surveying study area showing total sediment concentration for Hurricane Sandy on October 30, 2012. This corresponds to the peak of the northwest wave event, with a significant wave height of 3.6 meters, 12.5 seconds peak period and a peak wave direction of 334° as measured at the CariCOOS Rincón wave buoy. The color scheme depicts the total sediment concentration and the vectors indicate current direction.

Figure 4.29 shows the computed morphology change for Hurricane Sandy after the southwest wave event. In the nearshore zone, bands of erosion and accretion are evident along most of the coastline which was also observed for the Isaac event. Figures 4.29 and 4.30 show the computed morphology change for Hurricane Sandy after the southwest and northwest wave events, respectively. In Figure 4.30 there is a very significant region of large accretion in the Bajo Blanco area, with higher seabed accretion than Issac, at least for this area, but this area of strong sediment deposition is not apparent in Figure 4.29. This suggests that this large area of sediment deposition is due to the northwest swell following the southwesterly wave event caused by Sandy, something which did not happen in the event caused by Tropical Storm Isaac.

To qualitatively validate these computations, Figure 4.31 shows a visual comparison between the computed and observed accretion and erosion patterns. Again, at least from a qualitative perspective, the range of the computed values are very similar to the observed values, and similar patterns of erosion and accretion can be observed, at least from a large-scale perspective. It must be noted that the observations of bed change are somewhat noisy due to the fact that they were obtained using a single beam echo-sounder.

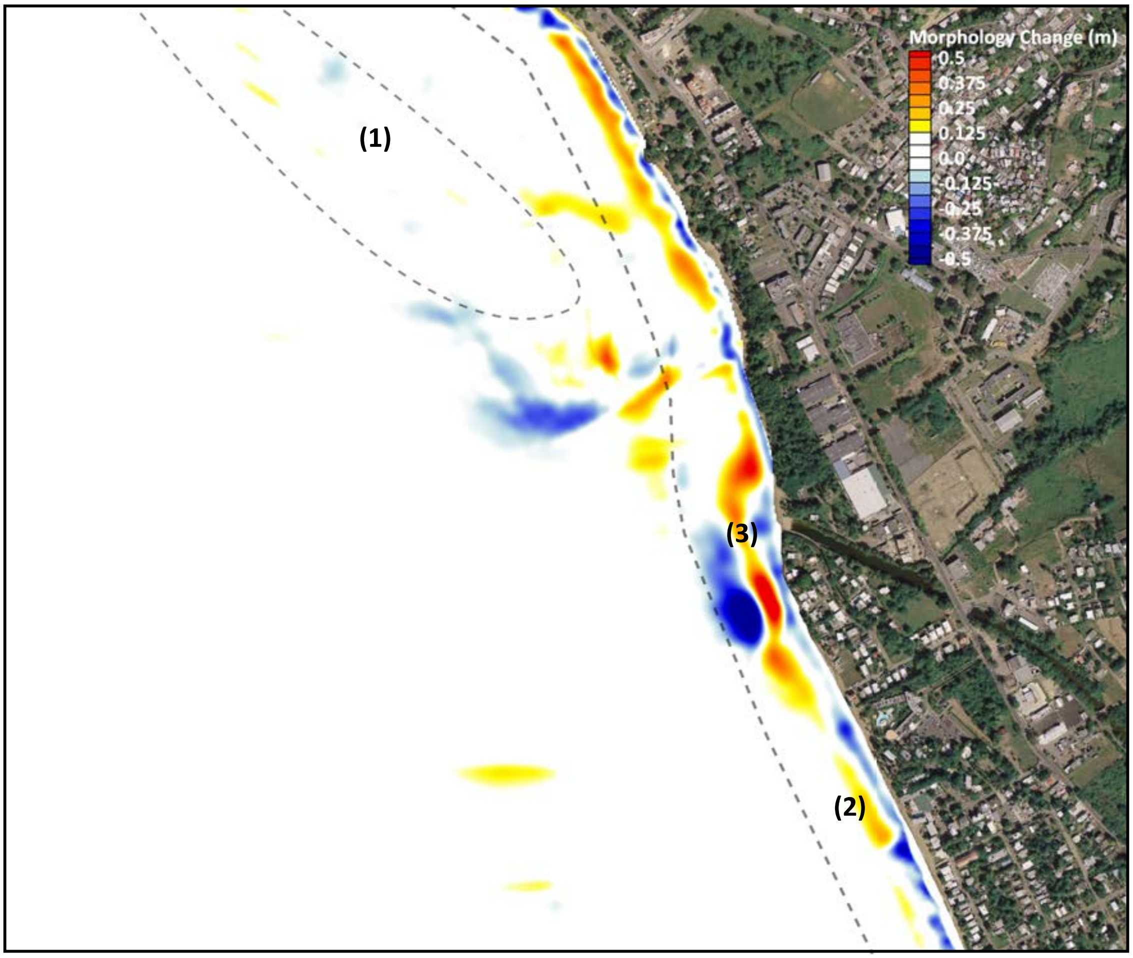

Figure 4.29: Computed morphology change for Hurricane Sandy on October 27, 2012, two days after the southwest wave event. The color scheme shows the morphology change where red $(+)$ indicates accretion and blue $(-)$ indicates erosion. Note the presence of three areas with significant morphology change: (1) the Bajo Blanco area, (2) the nearshore region and (3) Quebrada Los Ramos.

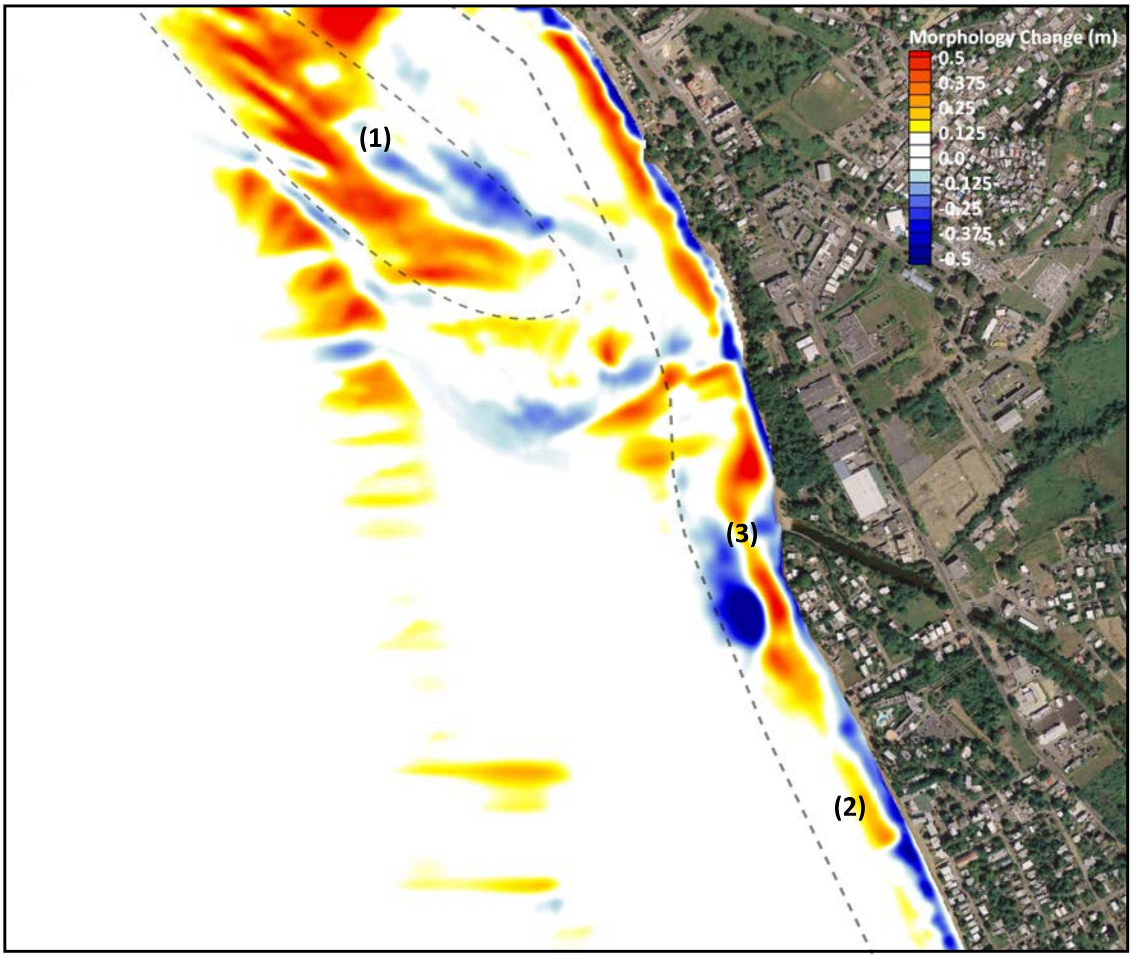

Figure 4.30: Computed morphology change for Hurricane Sandy on November 9, 2012, days after the waves from northwest subside. The color scheme shows the morphology change where red $(+)$ indicates accretion and blue $(-)$ indicates erosion. Note the presence of three areas with significant morphology change: (1) the Bajo Blanco area, (2) the nearshore region and (3) Quebrada Los Ramos.

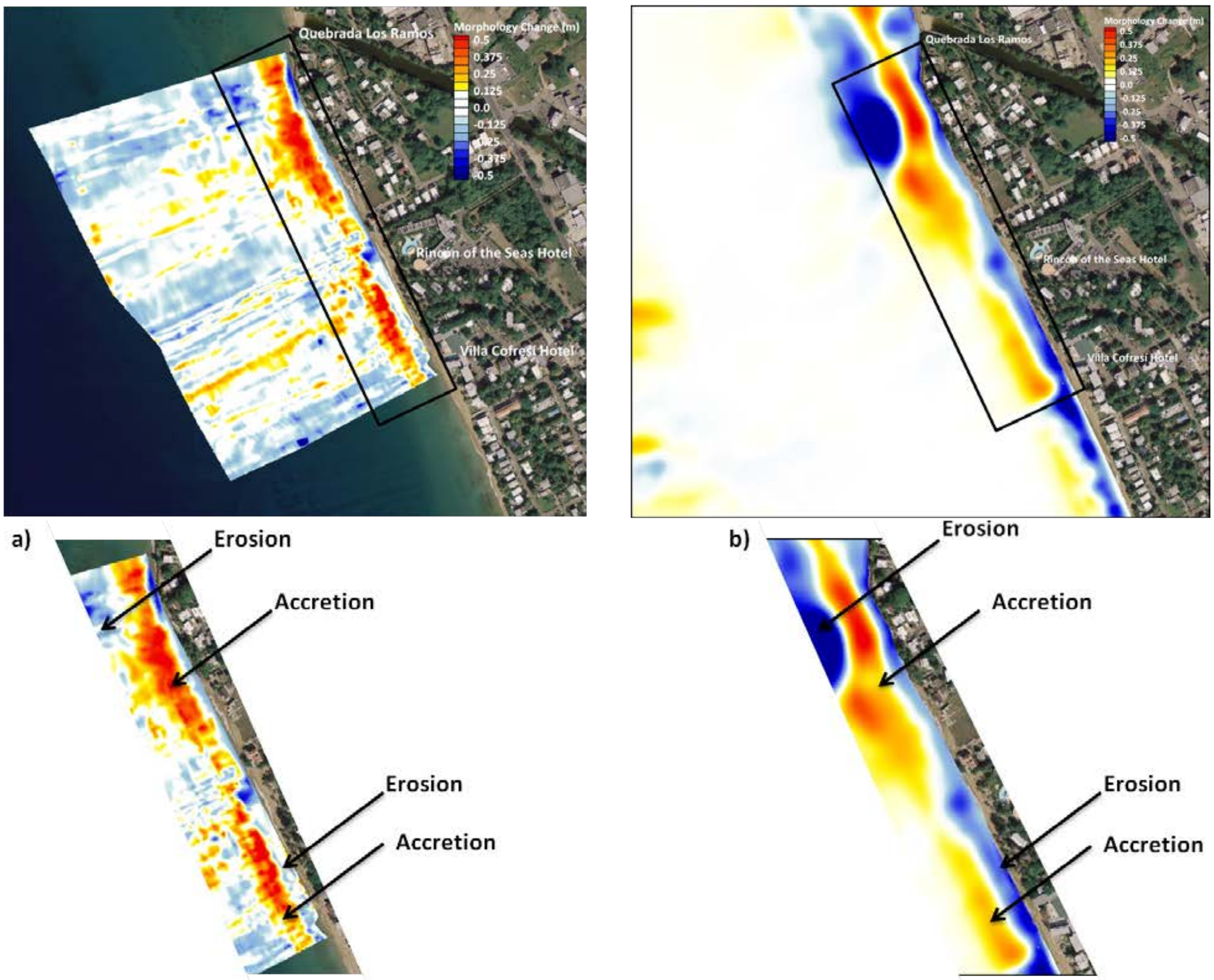

Figure 4.31: Cumulative erosion and accretion induced by Hurricane Sandy: a) measured morphology change and b) simulated morphology change. The color scheme shows the morphology change where red (+) indicates accretion and blue (−) indicates erosion.

4.6 Conclusions

The present study has been successful in improving understanding of the complex sediment transport processes which occur during storms in Rincón, Puerto Rico. A validation study of the Coastal Modeling System (CMS) for the coast of Rincón was conducted. The hydrodynamic module was validated by comparing predicted and observed depth-averaged currents, and a good agreement was found, especially during periods with large wave events. After proving that the model can be applied successfully to model the hydrodynamics of the study area, sediment transport simulations were executed. The model simulations were conducted using the NET sediment transport model with the Lund-CIRP equilibrium transport formulation. The main conclusions of this modeling study are as follows:

- The CMS model can correctly predict nearshore hydrodynamics in Rincón, provided that accurate boundary conditions be provided to the model.
- According to CMS, the southwesterly wave events caused by Isaac and Sandy generate significant sediment transport and morphology change in the nearshore region.
- According to CMS, the northwesterly swell generated by Sandy seemed to cause significant sediment transport and deposition mostly in the Bajo Blanco area, but did not greatly affect morphology change in the nearshore region as opposed to the southwest wave events.
- When compared with the jetski-based surveys, the CMS model appears to predict, at least qualitatively, the large scale features of the observed morphology change for both Isaac and Sandy.
- There are three main areas in which morphology change appears to be most significant: the Bajo Blanco area, the nearshore region and Quebrada Los Ramos.

Despite these encouraging measurements, it should be mentioned that the methodology presented has several limitations:

- The model does not account for erosion in the beach face.
- The sediment size was taken as spatially constant. Ideally, a spatially variable grain size distribution could be given to CMS if such data was available for the study site.

Nevertheless, the present study is the first time that such a comparison between observations and computations of morphology change have been conducted in Puerto Rico. The methodology applied in the present study could be readily implemented in other areas of Puerto Rico in which sediment transport information is needed.

Chapter 5

CONCLUDING REMARKS AND RECOMMENDATIONS

The main objective of the present study was to quantify and simulate storm-induced morphology change in the coast of Rincón, Puerto Rico. As a result, a surveying system was developed which could be deployed days before and after storm wave events in order to collect accurate high-resolution bathymetric data and characterize storm-induced morphology change.

Using the jetski-based bathymetric surveying system developed in the present study, hydrographic surveys during the Fall 2012 active storm season were performed, and observations of the coastal morphological response to Tropical Storm Isaac and Hurricane Sandy were obtained. As explained in Chapter 3, storm-induced nearshore morphology changes generated by both storm events were quantified, and the formation of a large shore-parallel sandbar was observed in both events. The analysis of cross-shore transects indicates that southwesterly wave events will generate offshore sediment transport leading to a possible loss of nearshore sand, and northerly long-period waves may help replenish the beach. In order to improve upon the present study, it is recommended that the following actions be performed:

- Additional hydrographic surveys of a larger area should be conducted to observe and understand alongshore sediment transport processes.

- Topographic surveys of the coastline should be performed in order to observe shoreline regression and to develop a seamless bathymetry-topography dataset across the mean water line.

- Multibeam sonar surveys should be conducted, and a real-time kinematic (RTK) GPS system should be added to the surveying system.

To relate the morphological response to the action of storm waves during the study period, a coupled wave-current-sediment transport numerical model, the Coastal Modeling System (CMS), was implemented. This numerical model allowed the evaluation of the complex storm-induced circulation generated by Tropical Storm Isaac and Hurricane Sandy. According to the CMS simulations, the southwesterly wave events generated by Isaac and Sandy induced seaward sediment transport whereas the northwesterly waves event generated by Sandy may have served as a constructive force which helped restore the coast. Alternating bands of erosion and accretion, as a response to storm wave events, were distinctly observed and qualitatively predicted by the model in the nearshore region. In order to improve upon the results obtained from the simulations, the following recommendations are provided:

- A detailed granulometry study should be conducted in order to provide spatially variable sediment properties to the CMS model.
- To compare the model simulations with a smoother observation field, multi-beam bathymetric surveys should be conducted before and after storm events in order to obtain better data of morphology change.
- A detailed sensitivity study regarding the impact of the different sediment transport formulae and parameter values (e.g., adaptation length) should be conducted.

This is the first time that such a study has been carried out to understand morphology changes in Puerto Rico, and the results have shown that the methodology applied here could be readily implemented in other areas of Puerto Rico. Further development of the surveying system and an improvement of the methodology presented could help to further improve the understanding of the complex sediment transport processes that affect the coasts of Puerto Rico.

REFERENCES

Actisense (2011). The NMEA 0183 Information Sheet.

Beach, R. A., Holman, R. A., and Stanley, J. (1994). Measuring nearshore bathymetry on high energy beaches. In *American Geophysical Union Fall Meeting*, San Francisco,CA.

Booji, N., Ris, R., and Holthuijsen, L. (1999). A third-generation wave model for coastal regions 1. Model description and validation. *Journal of Geophysical Research*, 104:7649–7666.

Cañizares, R. and Irish, J. (2008). Simulation of storm-induced barrier island morphodynamics and flooding. *Coastal Engineering*, 55:1089–1101.

Calvete, D., Ribas, F., de Swart, H., and Falqués, A. (2012). Effect of surface rollers on the formation of crescentic bars: Large angles of incidence. In *Proceedings of 33rd Conference on Coastal Engineering*, pages 1–5, Santander, Spain.

Camenen, B. and Larson, M. (2005). A general formula for non-cohesive bed load sediment transport. *Estuarine, Coastal and Shelf Science*, 63:249–260.

CariCOOS (2008). Caribbean Coastal Ocean Observing System. Website. http://caricoos.org/.

Chardón, P. (20). Field observations and numerical simulations of storm-induced nearshore morphology change in rincón, puerto rico. Master's thesis, University of Puerto Rico at Mayagüez.

Deltares (2011). *Delft3D-Flow User Manual*.

Deltares (2012). *Delft3D-Wave User Manual*.

Eversole, D. and Fletcher, C. (2003). Longshore sediment transport rates in a reef-fronted beach: Field data and empirical model Kaanapali beach, Hawaii. *Journal of Coastal Research*, 19 (3):649–663.

Fredsoe, J. and Deigaard, R. (1992). *Mechanics of Coastal Sediment Transport*. World Scientific.

Garmin (2012). GPSMAP 400/500 series Owner's Manual.

Judge, E., Overton, M., and Fisher, J. (2003). Vulnerability indicators for coastal dunes. *Journal of Waterway, Port, Coastal, and Ocean Engineering*, 129(6):270–278.

Larson, M., Kraus, N., and Hanson, H. (2002). Simulation of regional longshore sediment transport and coastal evolution: The Cascade model. In *Proceedings of* 28^{th} *Coastal Engineering Conference*. ASCE Press.

Lin, L. and Demirbilek, Z. (2012). Modeling combined diffraction-refraction in a coastal spectral wave model. In *Proceedings of the Twenty-second International Offshore and Polar Engineering Conference*, Rhodes, Greece.

MacMahan, J. (2001). Hydrographic surveying from a personal watercraft. *Journal of Surveying Engineering*, 127(1):12–24.

Masselink, G., Auger, N., Russel, P., and O'Hare, T. (2007). Short-term morphological change and sediment dynamics in the intertidal zone of a macrotidal beach. *Sedimentology*, 54(1):883–915.

Mesoscale and Microscale Meteorology Division (2007). *Weather Research and Forecasting Model*.

Miche, M. (1951). Le pouvoir reflechissant des Ouvrages Maritimes Exposes a l' Action de la Houle. *Annals des Ponts et Chaussess*, 121:285–319.

Morelock, J. (1978). Shoreline of Puerto Rico. Department of Natural Resources: Coastal Zone Management Program. Retrieved from: http://geology.uprm.edu/.

Morris, W., Vierra, K., Mastroianni, M., and Wilson, J. (2000). Surf and coastal area measurement platform (SCAMP). Technical Report, Areté Associates, VA.

Nam, P., Larson, M., Hanson, H., and Hoan, L. (2011). A numerical model of beach morphological evolution due to waves and currents in the vicinity of coastal structures. *Coastal Engineering*, 58:863–876.

Nam, P. T. and Larson, M. (2010). Model of nearshore waves and wave-induced currents around a detached breakwater. *Journal of Waterway, Port, Coastal, and Ocean Engineering*, 136:156–176.

National Weather Service (2012). NOAA National Hurricane Center. Website. http://nhc.noaa.gov/.

NOAA (2013). National Oceanic and Atmospheric Administration. Vertical Datum Transformation (VDatum). Website. http://vdatum.noaa.gov/.

Ojeda, E., Guillén, J., and Ribas, F. (2010). Dynamics of single-barred embayed beaches. *Marine Geology*, 280:76–90.

Padman, L. (2005). *Tide Model Driver (TMD) Manual*. Earth and Space Research.

Paolo, C. (2012). Sediment transport models for shallow water equation. Master's thesis, Universita Degli Studi DiPisa.

Ris, R., Holthuijsen, L., and Booji, N. (1999). A third-generation wave model for coastal regions 2. Verification. *Journal of Geophysical Research*, 104:7667–7681.

Ruggiero, P., Walstra, D., Gelfenbaum, G., and van Ormondt, M. (2009). Seasonal-scale nearshore morphological evolution: Field observations and numerical modeling. *Coastal Engineering*, 56:1153–1172.

Sánchez, A., Beck, T., Lin, L., Demirbilek, Z., Brown, M., and Li, H. (2012). *Coastal Modeling System Draft User Manual*. U.S. Army Engineer Research and Development Center, Coastal and Hydraulics Laboratory.

Science Delivery Division (2013). Queensland coastal risk and bathymetric LiDAR: A pilot study for collecting near-shore bathymetry. Technical Report, Department of Science, Information Technology, Innovation and the Arts Science Delivery, Brisbane, QLD.

Scott, K. R., Canals, M., and Vélez, F. J. (2012). *Coastal Erosion and Beach Morphology Changes in Rincón, Puerto Rico*. Poster session presented at the 2012 Ocean Sciences Meeting, Salt Lake City, UT.

Simiu, E. and Scanlan, R. H. (1996). *Wind Effects on Structures: Fundamentals and Applications to Design*. John Wiley & Sons Inc., Reading, Massachusetts.

StarFish (2010). 990F Towed Sidescan System. Specifications Sheet.

Taylor, L., Eakins, B., Carignan, K., Warnken, R., Sazonova, T., and Schoolcraft, D. (2008). Digital elevation models of Puerto Rico: Procedures, data sources and analysis. Technical Memorandum, National Oceanic and Atmospheric Administration, Boulder, CO.

Thieler, E. R., Rodríguez, R. W., and Himmelstoss, E. A. (2007). Historical shoreline changes at Rincón, Puerto Rico, 1936-2006. Technical Report, U.S. Geological Survey and U.S. Department of the Interior, VA.

Trifonova, E., Valchev, N., Andreeva, N., Eftimova, P., and Kotsev, I. (2011). Measurements and analysis of storm induced short-term morphological changes in the Western Black Sea. *Journal of Coastal Research*, 64:149–154.

U.S. Department of Commerce (1978). Ocean and coastal management in Puerto Rico. Website. http://coastalmanagement.noaa.gov/.

USACE (2010). U.S. Army Corps of Engineers: Wave Information Studies Project Documentation (WIS). Website. http://wis.usace.army.mil/.

van Rijn, L., Walstra, D., Grasmeijer, B., Sutherland, J., Pan, S., and Sierra, J. (2003). The predictability of cross-shore bed evolution of sandy beaches at the time scale of storms and seasons using process-based profile models. *Coastal Engineering*, 47(3):295–327.

van Son, S., Lindenbergh, R., de Schipper, M., de Vries, S., and Duijnmayer, K. (2009). Using a personal watercraft for monitoring bathymetric changes at storm scale. In *Proceedings of Hydro9 Conference*, Cape Town, South Africa.

Vélez, F. (2013). Nearshore hydrodynamics of Rincón, PR: Implications for sediment transport and coastal erosion. Master's thesis, University of Puerto Rico at Mayagüez.

Zarillo, G. and Brehinh, F. (2007). Hydrodynamic and morphological modeling at Sebastian Inlet, FL. In *Proceedings of Coastal Sediments '07 Conference*, pages 1297–1310, Reston, VA. ASCE Press.

Zhang, D., Liu, H., and Lin, P. (2003). The application of SWAN to the simulation of a storm surge. In *International Conference on Estuaries and Coasts*, Hangzhou, China.